Title
Hyperpolarized 13C Magnetic Resonance Spectroscopy: Probing Enzymatic Activity, Cellular Transport, and Oncogene Activation

Author
Leon, Christine

Publication Date
2014

Peer reviewed|Thesis/dissertation

Hyperpolarized ^{13}C Magnetic Resonance Spectroscopy: Probing Enzymatic Activity, Cellular Transport, and Oncogene Activation

by

Christine Leon Swisher

DISSERTATION

Submitted in partial satisfaction of the requirements for the degree of

DOCTOR OF PHILOSOPHY

in

Bioengineering

in the

GRADUATE DIVISION

of the

UNIVERSITY OF CALIFORNIA, SAN FRANCISCO

AND

UNIVERSITY OF CALIFORNIA, BERKELEY

[redacted]

Acknowledgements

I would never have been able to finish my dissertation without the guidance of my committee members, my co-workers, help from friends, and support from my family and my husband. There are almost too many to list. But I'll give it a shot.

I would like to express my deepest gratitude to my advisor, Dr. Dan Vigneron, for teaching me everything thing I know about conducting scientific research, for providing an excellent atmosphere for doing research, and for constantly challenging me to be a better scientist. I owe him the greatest debt for my success in my graduate work.

I would also like to thank Dr. Peder Larson for his guidance, caring demeanor, saintly patience and for sharing his brilliant insights with me, Dr. Sarah Nelson, who has mentored me as if I was her own student and is a great role model for all women in science, and Dr. John Kurhanewicz, for his infectious enthusiasm for science as well as for all of his guidance over the years. Indeed, I am truly blessed to have been a part of the talented people in the Surbeck Lab and incredibly grateful for their support.

In the surbeck lab, I want to give a special thanks to Dr. Robert Bok for teaching me about cancer biology, his help with my numerous animal experiments, and his saintly patience, Dr. Subramaniam Sukumar for his help with pulse sequence programming, Dr. Jason Crane for all of his help with the development of kinetic

modeling algorithms and his patience as I struggled to learn C, Dr. Emma Essock-Burns for her mentorship, Romelyn Delos Santos for her help with experiments and her unfailing kindness, Mark Van Criekinge for keeping the polarizers running and his patience, Jenny Che and Cathy Devine for being the most helpful administrators of all time, Drs. Adam Kerr and John Pauly for all their input on MAD-STEAM, Lucas Carvajal for help with the coils, Peter Shin, Dr. Ilwoo Park, Justin Delos Santos, Hong Shang, Hsin-Yu Chen, Zihan Zhu, and Eugene Milshteyn for their help with experiments, Dr. Jermey Gordon for many helpful discussions, Drs. Galen Reed and Cornelius Von Morze for their friendship and support over the years, and Drs. Bertram Koelsch and Renuka Sriram for valuable insights, help with experiments, and for being great collaborators.

Many thanks also go to Dr. Klaus Kruttwig for the many hours he has dedicated to our liver cancer project, Dr. Andrei Goga for serving on my quals and dissertation committee, and Dr. Michael Lustig for serving on my quals and dissertation committee and for mentoring me in the art of teaching.

I would like to take this opportunity to thank the Dr. Christian Frezza and the members of his group at the MRC Cancer Unit, whose lab I worked at for a short duration but with whom I forged a special bond. I am very thankful for his encouragement and for teaching me about cancer metabolism and molecular biology and sharing his inspiration love of science with us.

I also want to thank my undergraduate advisor Dr. Brent Vernon and the members of his group for believing in me and motivating me to pursue a career in academia. Drs. Brent Vernon, Ryan McLemore, Bee Hoon Lee, Michael Caplan, Vincent Pizziconi, and Alex McLaren gave me a much-needed early push as an undergraduate that continues to propel me forward - for that I owe them a special debt.

I am also deeply grateful for all the faculty, staff, and students of the UC Berkeley - UCSF Graduate Program in Bioengineering who have provided me with a tremendous graduate education. They have taught me how to think about science; provided me with numerous opportunities and economic support; shown me how to approach my work as a scientist; and how to think about the big picture.

But most of all, I want to thank my family, whose unconditional love and support has helped me the most: to my grandparents, who have inspired me to pursue this career path, the whole Menking Clan, who are always my biggest cheerleaders, my father who always believes in and encourages me, instilled a love of science, and showed me the value of hard work, my mother and step-father who have supported me in every way imaginable, and finally my husband, Matt, for his love and sacrifice, for patiently proofreading every paper and listening to every talk, and his unfailing support.

Thanks to you all!

Christine Leon Swisher

June 2014

Hyperpolarized ^{13}C Magnetic Resonance Spectroscopy: Probing Enzymatic Activity, Cellular Transport, and Oncogene Activation

Abstract

Magnetic resonance spectroscopy (MRS) of hyperpolarized (HP) substrates is a powerful tool to investigate tissue metabolism in vivo. Recently, a first-in-man clinical trial of this technology showed feasibility, safety, and great promise for noninvasive diagnosis of cancer via the detection of previously unobservable phenomena such as the Warburg Effect. However, the acquired signal is a combination of flow, perfusion, diffusion, and relaxation in addition to metabolism. To isolate these effects and provide improved measurement of metabolic alterations in cancer, I designed tailored acquisition and reconstruction techniques. These techniques rely on the phase accumulation from stimulated echoes to "tag" metabolites and compressed sensing data undersampling to optimize acquisition time and resolution, thus allowing for the accurate, non-invasive measurement and localization of enzymatic activity, cellular transport, and oncogene activation. Specifically, we detected high enzymatic activity of lactate dehydrogenase (LDH) in high-grade regions within primary tumors and metastatic lesions in a transgenic

prostate cancer tumor model. We also observe increased efflux of lactate via monocarboxylate transporter 4 (MCT4), which is upregulated in aggressive subsets of a number of cancers and may correlate with metastatic potential. We also detected the presence of the h-Ras oncogene in a switchable oncogene-driven model of liver cancer, which expresses altered oncogene-induced signaling pathways between c-Myc and h-Ras driven cancer models. Notably for oncology in particular, these new techniques have great biomedical and clinical significance, as they could be used to better identify particularly aggressive regions within tumors, monitor cancer progression, follow response to therapy, and improve treatment planning.

Hyperpolarized ^{13}C Magnetic Resonance Spectroscopic Acquisition and Reconstruction

Probing Enzymatic Activity, Cellular Transport, and Oncogene Activation

By

Christine Leon Swisher

Committee

Chair: Dan Vigneron, PhD

Second Reader: Sarah Nelson, PhD

Third Reader: Andrei Goga, MD, PhD

Fourth Reader: Michael Lustig, PhD

Table of Contents

List of Figures

List of Tables

Chapter 1: Introduction

Nuclear Magnetic Resonance (NMR) is one of the most prolific fields of the past century - resulting in six Nobel prizes in the past 50 years from the discovery of the magnetic moment and the first recordings of atomic nuclei to the imaging of human diseases. NMR continues to evolve, changing the face of many different scientific disciplines.

Since its introduction only three decades ago, magnetic resonance imaging (MRI) has become a very powerful and widely used imaging modality due to its safety, flexibility, and high soft tissue contrast. Clinically, MRI acquisitions provide a breadth of information including anatomical imaging, angiography, diffusion mapping, functional brain imaging, guided intervention, and spectroscopic imaging, to name a few. The disease application areas are just as wide-ranging including cancers, orthopedics, neurologic disorders, cardiovascular disease, hepatobiliary disease, vascular disorders, and many more.

Typically, MRI images are acquired with proton (^{1}H) signals from water molecules in the body. This provides high SNR as the ^{1}H isotope has a high abundance of ~100% and as well as high concentration as the body is primarily made up of water. Proton Magnetic Resonance Spectroscopic Imaging (MRSI) not does not have this advantage as it reports on non-water low concentration metabolites. However, the information on biochemical profiles allows for differentiation of disease and normal tissues that are often not be possible with conventional MRI techniques. Carbon-13 MRSI would provide for an even wider range of metabolites but the SNR further suffers due to a low natural abundance of 1.1%, reduced gyromagnetic ratio, and low concentrations of important metabolites *in vivo*.

Recently the technological breakthrough of dissolution dynamic nuclear polarization has

allowed for unprecedented increases in SNR of greater than 10,000 fold. This allows for the detection of carbon-13 signals, which were previously unobservable. This new technology has gathered great excitement as it enables the ability to monitor uptake and conversion of key metabolites in disease.

This new technique has the potential to become a major new metabolic imaging technique providing valuable information on previously-inaccessible aspects of biological processes and has even been translated into the clinic with the first-in-man clinical trial of this new imaging modality at UCSF. Not only does this new technology provide unprecedented clinical information, it also gives us a new means to investigate the real-time processes of cells for the first time.

The scientific work presented in this dissertation adds to the current literature on hyperpolarized ^{13}C imaging specifically to both the understanding the underlying causes and effects of alterations in metabolism and their connection with cancer as well as the development of tools that utilize aberrant cancer metabolism as a biomarker of disease. My dissertation includes four main Bioengineering contributions in Chapters 3-5,7 each of which is a minor adaptation of either an already published, peer-reviewed manuscript or one in the process of being published. Chapters 6 and 8 are from peer-reviewed work submitted to the Proceedings of the International Society of Magnetic Resonance in Medicine.

Chapter 3 details the application of kinetic modeling to the acquisition and reconstruction method MAD-STEAM (metabolic activity decomposition with stimulated echo acquisition mode). This technique doubles the information via the direct detection of exchanging spins. This greatly enhances the sensitivity to flux and exchange mediated by the Lactate

Dehydrogenase enzyme (LDH), which is often upregulated in cancer.

In Chapter 4, the topic of Metabolic Activity Decomposition is revisited with the addition of a spectroscopic imaging readout and the necessary post-processing reconstruction algorithm. With the addition of localization and the imaging of the distribution of exchange, the specificity of the technique to detect elevated enzymatic activity indicative of cancer was validated.

In Chapter 5, the topic of Metabolic Activity Decomposition is revisited with the addition of a variable diffusion weighting. With the addition of varied diffusion weighting, it is possible to acquire exchange, relaxation and diffusion parameters within a single acquisition.

In Chapter 6, the principles of Metabolic Activity Decomposition were adapted to rapidly acquire 2D EXchange SpectroscopY (EXSY) spectra of hyperpolarized substrates. The results highlight the importance of investigating bidirectional exchange in the study of metabolism as well as show its potential to be used as a diagnostic tool.

In Chapter 7, cancer metabolism is further investigated with hyperpolarized carbon-13, whereby the effect cancer on pyruvate metabolism is investigated with the activation of both the Myc and Ras oncogenes. Here we show that h-Ras and c-Myc activation can be differentiated via the presence pyruvate-to-alanine conversion in a switchable model of liver cancer. We show for the first time that a hyperpolarized carbon-13 labeled substrate can be used as metabolic imaging agent for non-invasive, *in vivo* monitoring of the presence of h-Ras and more generally for the differentiation of oncogenes via metabolic reprogramming.

In Chapter 8, kinetic modeling algorithms were developed to aid in the interpretation and

visualization of hyperpolarized signals, which are key to the translation of the technology into the clinic.

Finally, in Chapter 9, I conclude by giving a summary of the technique development and preclinical cancer applications presented in this dissertation and discuss clinical prospects and future directions for hyperpolarized ^{13}C technology.

Chapter 2: Background

This chapter will focus on Magnetic Resonance Imaging (MRI) and Magnetic Resonance Spectroscopy (MRS) fundamentals that are necessary for accomplishing and understanding the developments undertaken in this dissertation project. In particular, the background on STEAM and EXSY pulse sequences are necessary for the understanding of the advancements made in chapters 3-6. Following the introduction of MRI/MRS, a brief introduction will be given on hyperpolarization and its application in the field of hyperpolarized carbon-13 MR. Then a broad introduction is included on the metabolic adaptations in cancer. Briefly oncogenes will be introduced as background for Chapter 7. Finally, enzyme kinetics and monocarboxylate transporters will be introduced, as they are key to understanding the significance of the findings in Chapter 3-5.

2.1 Fundamentals of Magnetic Resonance Imaging

2.1.1 Spin, Magnetic Moment, Magnetization Vector, and Polarization

Atoms with an odd number of protons and neutrons possess a nuclear spin angular momentum and thus exhibit nuclear magnetic resonance (MR) phenomenon[1,2]. Qualitatively, these nuclei can be described as spinning charged spheres, which results in a small magnetic moment or "spin"[1,2]. In living things, protons (^{1}H) are the most abundant MR visible nuclei due to a high natural abundance and a large percentage of living tissue is made up of H_20. Thus, ^{1}H is the most widely studied for MRI scanning. Other biologically meaningful nuclei have non-zero "spin", such as ^{13}P (with 15 protons + 16 neutrons) and ^{13}C (with 6 protons + 7 neutrons). The spin angular momentum can be expressed as a vector quantity

$$\boldsymbol{S} = \frac{h}{2\pi}\boldsymbol{I} \tag{2.1}$$

where h is Planck's constant (h = 6.62606957 × 10^{-34} m^2 kg / s) and $\boldsymbol{I}$ is the spin operator in quantum mechanics. This gives rise to a magnetic dipole moment $\boldsymbol{\mu} = \gamma \boldsymbol{S}$ that is dependent on the gyromagnetic ratio γ that is an inherent property of each atomic nuclei species[3]. In the presence of a magnetic field, a magnetization moment $\boldsymbol{M} = \sum \boldsymbol{\mu}$ will be produced in the direction of the applied field (Figure 2.1b).

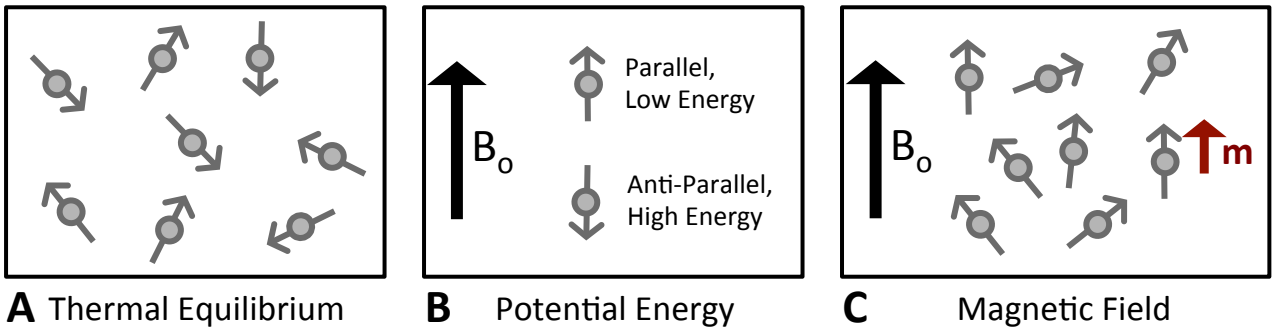

Figure 2.1: (a) Random orientation of spin at thermal equilibrium. **(b)** There are two states a nuclei can be in either parallel (low energy) or anti-paralle l(high energy). **(c)** In the precense of a static magnetic field a net magnetization vector **m** will arise. The lowest energy configuration is for the dipole magnetic moment to be parallel with the static magnetic field, B_0 *(Adapted from Hu, S 2010).*

The total equilibrium magnetization is equal to the net difference between the nuclei aligned and anti-aligned with the applied field, B_o.

$$M_o = \frac{N\mu(I_z+1)B_o}{3kT} \tag{2.2}$$

Therefore, the magnetization is proportional to the applied B_o. Where μ is the magnetic moment of a single nucleus and N is the number of nuclear spins per unit volume. Polarization can be understood with a quantum mechanical description. The potential energy, E, of a magnetic moment, μ, in the presence of a $\boldsymbol{B}$ field is $E = -\mu \cdot \boldsymbol{B} = -\mu_z B_o = -\gamma S_z B_o$. The difference between the two energy states can be written as[3]

$$\Delta E = h\frac{\gamma}{2\pi}B_o \tag{2.3}$$

for spin ½ particles. The signal comes from the difference between the two populations (red spin shown in the Figure 2.2), one parallel (n_+) and the other anti-parallel (n_-). The tendency is to occupy the minimum energy state. Therefore, the n_+ population is favored as it is of lower energy (shown in Figure 2.1). When thermal energy exceeds the energy separation spins can occupy both energy states. The ratio the two populations is dependent on the Boltzmann distribution[3]:

$$\frac{n_-}{n_+} = e^{-\Delta E/kT} \tag{2.4}$$

k denotes the Boltzmann constant ($1.3806488 \times 10^{-23}$ m^2 kg s^{-2} K^{-1}), and T is the temperature in Kelvin. Typically, this ratio is approximately 0.999993 per Telsa for conventional proton MR. Only 7 out of 10^6 will be in excess in the parallel state[3]. Macroscopically, this minute excess accounts for all of the polarization that observed with NMR and MRI. The polarization, P,

$$P = \frac{n_+ - n_-}{n_+ + n_-} = \frac{e^{-\Delta E/kT} - 1}{e^{-\Delta E/kT} + 1} \tag{2.5}$$

describes the fraction of the spins aligned with the B_o vector. Using Eq 2.5 with a magnetic field of 3T and at body temperature (310K), the polarization of ^{13}C is 2.49×10^{-6}, meaning that out of a million spins, only a few more are parallel to the magnetic field than antiparallel.

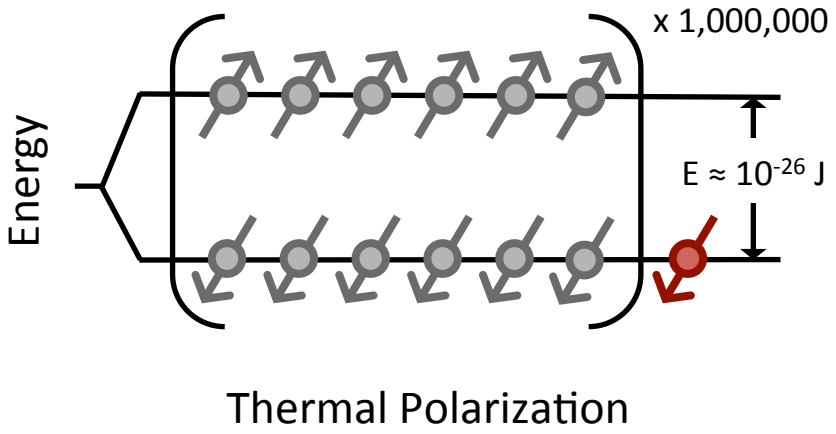

Figure 2.2 Thermal polarization from population difference of nuclear spin energy states.

This small magnetization is the basis of detected signal in MRI. For ^{1}H, the polarization is moderately improved at 9.88 x 10^{-6} albeit still very small. However, high signal-to-noise ratio (SNR) is achieved due to the high concentration of water molecules *in vivo* and high natural abundance of the ^{1}H isotope (>99.9%)[3]. ^{13}C has neither of these advantages. However, SNR can be dramatically improved with a technique called dissolution dynamic nuclear polarization (DNP)[4] (described in Section 2.3).

2.1.2 RF Excitation

The NMR signal arises from precession of the net magnetization, **M**, which is originally aligned with a main magnetic field, **B**. When **M** is tipped away from **B, M** will precess about **B** similar to a spinning top. This precession is described by the following equation[5]:

$$\frac{d\boldsymbol{M}}{dt} = \boldsymbol{M}\times\gamma\boldsymbol{B} \tag{2.6}$$

Solving equation 2.1, the precession of **M** about **B** occurs at the angular frequency $\omega_o = \gamma B_o \ rad/s$, namely the Larmor frequency. Each nuclei will have a specific gyromagnetic ratio that is inherent to that specific isotope (shown in Table 2.1)[3].

Table 2.1: Natural Abundance and gyromagnetic ratio for several isotopes commonly observed with NMR and MRI. (Adapted from Levitt 2001.)

Isotope	Spin	Natural Abundance	Gyromagnetic Ratio
^{1}H	1/2	~100%	267.5 x 10^{6} rad $s^{-1}T^{-1}$
^{2}H	1	0.015%	41.1 x 10^{6} rad $s^{-1}T^{-1}$
^{13}C	1/2	1.1%	67.3 x 10^{6} rad $s^{-1}T^{-1}$
^{31}P	1/21	~100%	251.8 x 10^{6} rad $s^{-1}T^{-1}$
^{23}Na	3/2	~100%	70.8 x 10^{6} rad $s^{-1}T^{-1}$
^{19}F	1/2	~100%	108.4 x 10^{6} rad $s^{-1}T^{-1}$
^{129}Xe	1/2	26.44 %	74.0 x 10^{6} rad $s^{-1}T^{-1}$

To detect the magnetization, an oscillating magnetic field, $B_1(t)$ at the Larmor resonant frequency is applied to the aligned nuclei by transmitting with Radio Frequency (RF) coils. Because the frequency of the oscillating applied magnetic field matches the nuclei's resonant frequency, the nuclei absorb the energy, their magnetic moment changes orientation, and they are excited[3]. This results in a change in their net magnetization after which the nuclei begin precession.

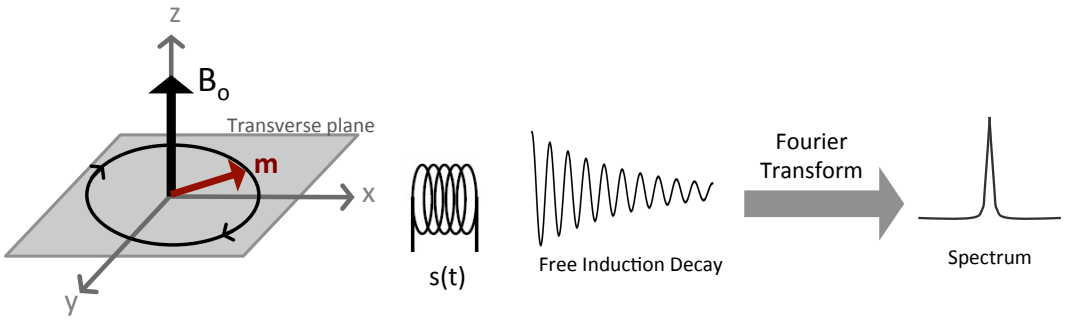

Figure 2.3 Schematic of signal detection at coil. Magnetization is tipped away from the static main magnetic field, B_o, into the transverse plane where it can be detected by an induced voltage in a nearby radiofrequency coil.

Excitation occurs when the magnetic moment of the nuclei is tipped away from the static field, into the transverse plane. Followed by precession about the axis of the static magnetic field[1,3]. The duration of the RF pulse applied determines the angle between net magnetization of the spins and the static magnetic field and at this angle the spins will

precess around the longitudinal axis.

The excited nuclei are now in the higher energy state from the absorption of energy from the applied magnetic field. Because the tendency is to occupy the lower energy state they will eventually return to the equilibrium state aligned parallel with the main magnetic field. As the spins precess, energy is emitted at the Larmour frequency producing a detectable signal called free induction decay (FID). The FID is a result of the voltage induced in nearby receiving RF coils[1].

The amplitude of $s(t)$ is a function of the net magnetization and flip angle:

$$s(t) \propto M_o e^{-i2\pi f_{ot}} \sin(\theta) \tag{2.7}$$

where θ is the RF pulse flip angle determined by the intergal of the applied oscillating magnetic field[3].

$$\theta = \gamma \int_0^T B_1(t)dt \tag{2.7}$$

For a B_1 field with a constant amplitude, namely a non-selective excitation, the angle of excitation is given by:

$$\theta = \gamma B_1 \sqcap \tau \tag{2.7}$$

Once magnetization is tipped from the longitudinal axis (z), aligned with B_o, it can be observed in the transverse plane (x, y). Thus, the signal strength from the transverse component of the magnetization, m_{xy}, is given by the sine of the flip angle, θ. The unexciting magnetization can be stored in the longitudinal axis, m_z. It is given by the cosine of the flip angle. Such that for a $\pi/2$ flip angle, $m_{xy} = M_o sin(\theta) = M_o$ and

$m_z = M_o cos(\theta) = 0$. For hyperpolarized applications, where the magnetization does not recover, the flip angle should be much less than $\pi/2$ to preserve magnetization for dynamics and imaging.

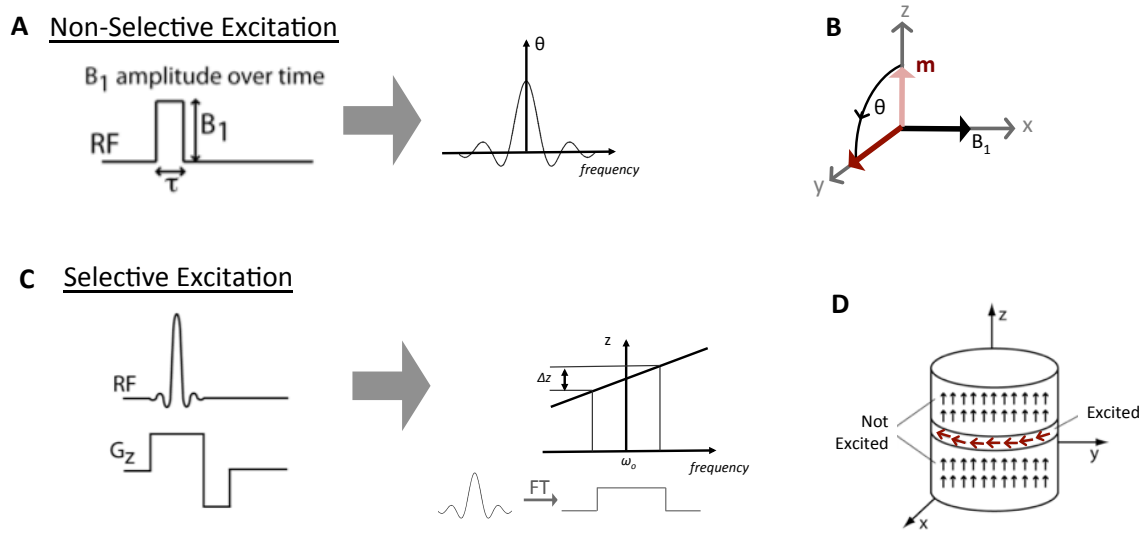

Figure 2.4: (a) Non-selective excitation can be achieved with a hard pulse. Its Fourier transform give a sinc shaped frequency response. **(b)** The flip angle is determined by Eqn. 2.7. **(c)** To excite only a slice from a volume, a sinc pulse and a gradient in the slice select direction are applied. The Fourier transform of the sinc pulse will excitate a bandwidth of frequencies encoded by the gradient. **(d)** Only spins in the excitation bandwidth, Δω, which are located in Δz are excited. *(Adapted from Hu, S 2009 and Nishimura, D 1996).*

The non-selective, "hard" pulse shown in Figure 2.4a will excite the entire volume[3]. Slice selection can be achieved with the application of a sinc shaped $B_1(t)$ pulse and a gradient applied on the axis of the desired slice. The gradient imparts a linear variation in the frequencies, $f(z) = \frac{\gamma}{2\pi}(B_o + Gz)$, in space such that the slice can be chosen by with a frequency selective RF excitation pulse. Only the slice which contains Larmor frequencies that match the frequencies of the oscillating magnetic field will be excited[3]. The slice thickness can be altered by varying the and the amplitude of the slice selection gradient or by changing the the bandwidth of the selective pulse, $thickness = 2\pi\, BW/\gamma G$[3].

The excitation profile of a $B_1(f)$ is the Fourier transform of $B_1(t)$ for small flip angles (<90°). The Fourier transform of the applied sinc, $B_1(t) = BW\ sinc(BW \cdot t)$, is a rect $B_1(f) = \sqcap\ (\frac{f}{BW})$ with an excitation bandwidth BW. Of course an infinitely long *sinc* pulse is theoretically impossible and thus a windowed *sinc* is applied resulting in an imperfect slice selection profile. Optimizing the shape of the RF pulse in time can be used to improve spatial selectivity.

2.1.3 Relaxation

The signal acquired after excitation is easily described by a Larmor frequency oscillation term and a decay term. The decay is a result of a inherent decay constant, T_2 or spin-spin relaxation, and another term that is dependent on the homogeneity of the sample[2]. This term is called T_2^*, and is defined as

$$\frac{1}{T_2^*} = \frac{1}{T_2} + \frac{1}{T_2'} = \frac{1}{T_2} + \gamma \Delta B_o \tag{2.8}$$

where $T_2' \propto \Delta B_o$ is proportional to the inhomogeneity of the field strength ΔB_o.

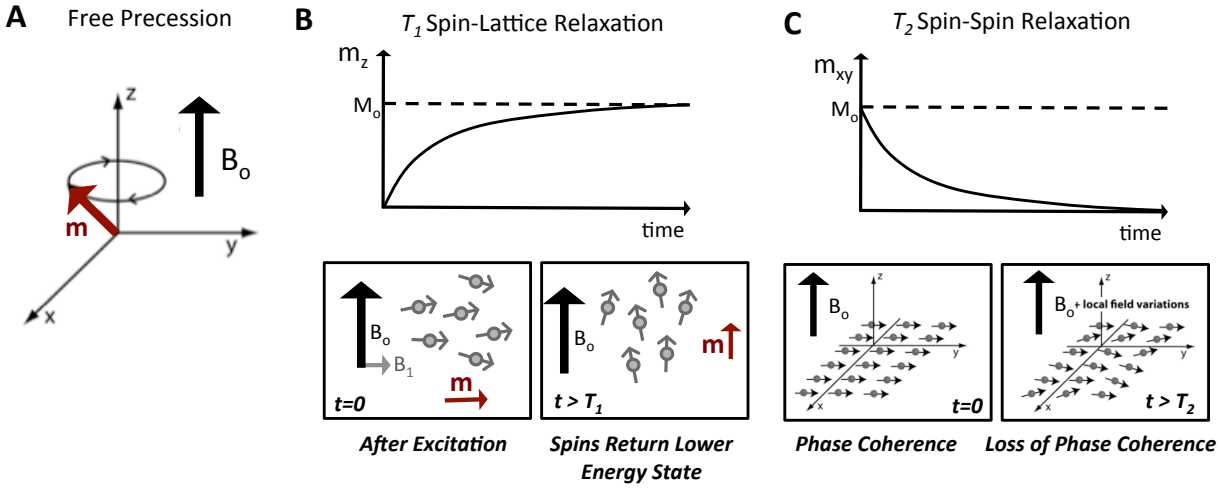

Figure 2.5: Precession and relaxation. **(a)** When tipped from the z-axis, the magnetization vector precesses about the static magnetic field direction (z-axis). **(b)** After being tipped away from the z-axis, the magnetization along z gradually returns (T_1 relaxation). **(c)** Without local variations in magnetic field, all spins in a volume precess at the same rate and have phase coherence. Dephasing occurs when there are local variations in magnetic field, called T_2 relaxation. *(Adapted from Hu, S, 2009).*

This spin-spin relaxation mechanism occurs in the transverse plane[2]. Following an excitation, T_2 relaxation can be observed. Initially, all of the spinning dipoles within the excited sample are precisely in phase. Quickly, they will begin to lose coherence as some spin slightly faster than the others[1,2] due to heterogeneity within their micro-enviroments[6]. T_2 relaxation occurs in a inhomogeneous magnetic field whereby energy can be transfered from dipoles aligned with and opposed to the main magnetic field. This transfer results in a change in the energy state of the dipoles[2]. This rate at which energy is transferred is proportion to the variations of the local magnetic field.

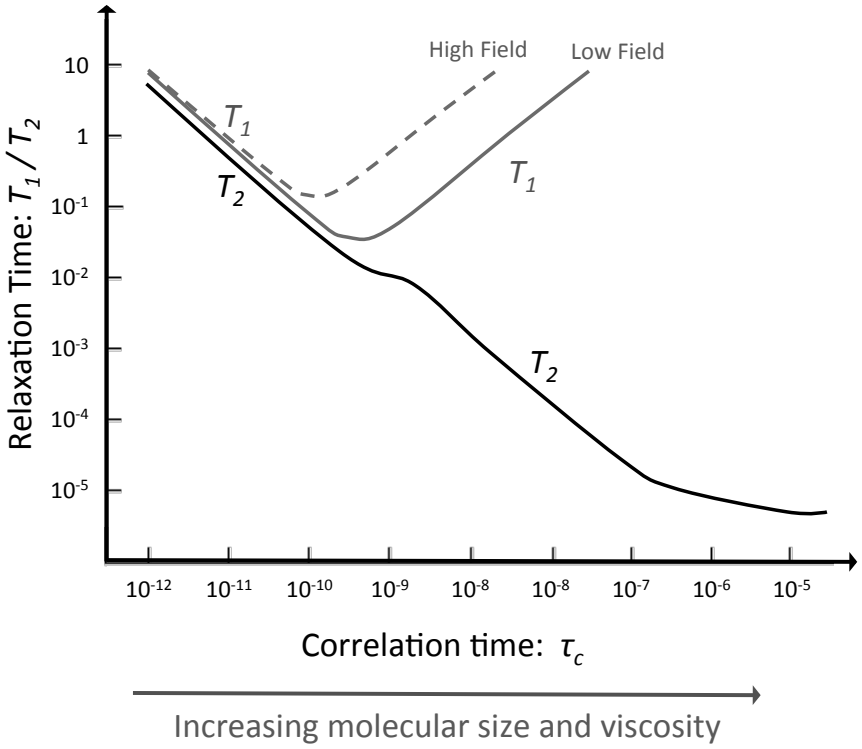

Figure 2.6: Relaxation versus correlation time. *(Adapted from Levitt, MH 2001).*

T_2 spin-spin relaxation is related to the rate of rotation and translation (correlation time, τ_c) of the adjacent dipoles. The dipole-dipole interaction is also increased as the strength of the local field increases and is also dependent on the proximity of the adjacent dipoles[1,2]. Therefore in pure water T_2 is long, about 3-4 seconds. Protons in pure move much faster than the Larmor frequency[1,2]. However, in solutions of macromolecules and tissues the spin-spin relaxation rate is much faster, i.e., the T_2 time is shorter[1,2].

In the presence of a "perfectly" uniform magnetic field and with an object without susceptibility effects, T_2 and T_2^* would be equal. In reality, T_2^* relaxation occurs because of the static field non-uniformity, ΔB_o , within each voxel which results from both imperfections in the static magnetic field as well as from magnetic susceptibility effects in sample inside the field or even in the patient.

The acquired signal is $s(t) = M_o e^{-i2\pi f_o t} e^{-t/T_2^*}$ because m_{xy} decreases in amplitude over time according to[3]:

$$\frac{dm_{xy}}{dt} = -\frac{m_{xy}}{T_2^*} \quad (2.9).$$

The solution to Eqn. (2.9) is:

$$m_{xy}(t) = M_o e^{-t/T_2^*} \quad (2.10).$$

A long T_2 and minimization of ΔB_o is optimal for hyperpolarized experiments providing increased SNR and the ability to acquire increased spatial resolution.

The other relaxation mechanism is T_1 relaxation, also called longitudinal relaxation and spin-lattice relaxation. After $\boldsymbol{M}$ is tipped away from the +z axis, the remaining m_z component is less than the original magnetization along +z, which is denoted M_o. m_z will recover back to M_o over time according to[3]:

$$\frac{dm_z}{dt} = -\frac{m_z - M_o}{T_1} \quad (2.11).$$

The solution to Eqn. (2.11) is:

$$m_z(t) = M_o + (m_z(0) - M_o)e^{-t/T_1} \quad (2.12).$$

T_1 relaxation is a result of induced field fluctuation due to molecular motion, whereby the local fielded experienced by a nuclei changes when the molecular reorients[1,2]. Spin-lattice relaxation is governed by a number of mechanisms including dipolar coupling, quadrupolar coupling, paramagnetics, scalar coupling, chemical shift anisotropy (CSA), and spin rotation. Similarly to T_2, T_1 relaxation depends on the correlation time, τ_c. Using the Bloembergen-Purcell-Pound theory (BPP theory), which takes into account the effect of

tumbling motion of molecules on the local magnetic field disturbance, T_1 relaxation can be derived from the following relationship[7]:

$$\frac{1}{T_1} = K\left[\frac{\tau_c}{1+\omega_o^2\tau_c^2} + \frac{4\tau_c}{1+4\omega_o^2\tau_c^2}\right] \quad (2.13)$$

where $K = \frac{3\mu_o^2}{160\pi^2}\frac{h^2\gamma^4}{2\pi r^6}$ for a spin-1/2 nuclei. The theory is in good agreement with experiments on pure substances, but can not handle more complicated systems such as the human body.

T_1 of a hyperpolarized substrate is very important as it determinates the acquisition time of the experiment. Unlike thermally polarized systems where signally averaging is possible, a long T_1 is desirable for hyperpolarized experiments as it allows for increased acquisition time. Increased acquisition time can be used to acquire higher resolution images as well as investigate the dynamics of chemical exchange over time.

2.1.4 Magnetization Dynamics and Exchange

Combining the effects of precession (Eqn. (2.6)), transverse relaxation (Eqn. (2.9)), and longitudinal relaxation (Eqn. (2.12)) gives the Bloch equation[5]:

$$\frac{d\boldsymbol{M}}{dt} = \boldsymbol{M}\times\gamma\boldsymbol{B} - \frac{m_x\hat{\imath}+m_y\hat{\jmath}}{T_2^*} - \frac{(m_z-M_o)\hat{k}}{T_1} \quad (2.14).$$

The Bloch equation is a phenomenological description of magnetization vector dynamics and is extremely valuable for understanding MRI.

To describe chemical exchange, a phenomenon often observed in hyperpolarized carbon-13 spectroscopy, the Bloch equations must be adapted to include terms that take into account relaxation as a result of chemical exchange. Chemical exchange describes any

process in which a nuclei exchange between at least two environments resulting in a change of NMR parameters such as chemical shift, coupling, or relaxation rate. These can be intramolecular such as protein folding or conformational isomerism or intermolecular such as enzyme catalyzed reactions, binding, and protonation.

The Bloch equations for a spin that can be in state A_1 or A_2 in the absence of exchange can be described by the following[8,9]:

$$\frac{d\boldsymbol{M_1}}{dt} = \boldsymbol{M_1}\times\gamma\boldsymbol{B_1} - R_1(\boldsymbol{M_1} - \boldsymbol{M_{10}}) \tag{2.15}$$

$$\frac{d\boldsymbol{M_2}}{dt} = \boldsymbol{M_2}\times\gamma\boldsymbol{B_2} - R_2(\boldsymbol{M_2} - \boldsymbol{M_{20}}) \tag{2.16}$$

where R_1 and R_2 are the full relaxation matrixes for the spin in state A_1 or A_2, respectively. Assuming that exchange from A_1 to A_2 and vise versa is instantaneous, the equations can be modified to include exchange with the addition of a first order kinetics term[9].

$$\frac{d\boldsymbol{M_1}}{dt} = \boldsymbol{M_1}\times\gamma\boldsymbol{B_1} - R_1(\boldsymbol{M_1} - \boldsymbol{M_{10}}) + \boldsymbol{k}(\boldsymbol{M_2} - \boldsymbol{M_1}) \tag{2.17}$$

$$\frac{d\boldsymbol{M_2}}{dt} = \boldsymbol{M_2}\times\gamma\boldsymbol{B_2} - R_2(\boldsymbol{M_2} - \boldsymbol{M_{20}}) + \boldsymbol{k}(\boldsymbol{M_1} - \boldsymbol{M_2}) \tag{2.18}$$

These equations a very helpful in the analysis of slow, intermediate and fast chemical exchange. Fast exchange, $k \ll |\delta_1 - \delta_2|$, is characterized will result in a single resonance shifted by the weighted average of two chemical shifts, $\delta_{obs} = f_1\delta_1 + f_2\delta_2$. For intermediate exchange, $k \approx |\delta_1 - \delta_2|$ coalescence resulting in line broadening will be observed. In the case of slow exchange $k \gg |\delta_1 - \delta_2|$, separate lines are observable for each state. Each line will be broadened by $\Delta LW = k/\pi$. However, many other factors can affect line shape. Additionally, the difference between the coupling constants, J, and $T_2 s$ determines the exchange regime.

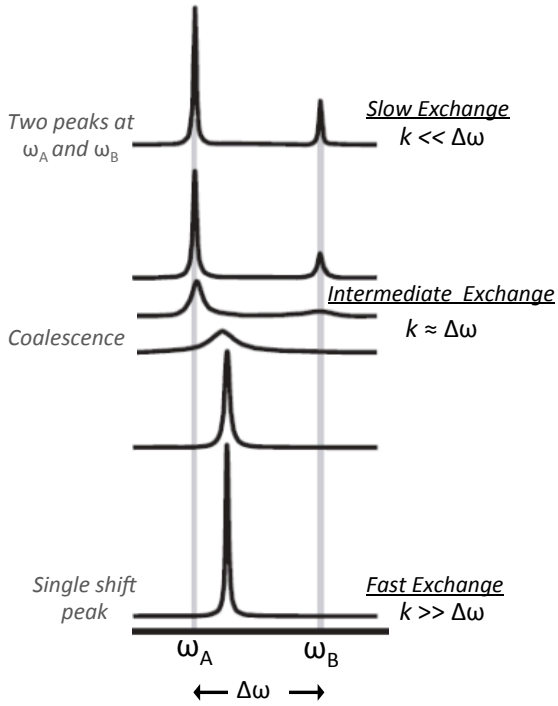

Figure 2.7: Appearance of spectra for two resonances exchanging in fast, intermediate, and slow exchange regimes.

2.1.5 K-space and Imaging Principles

The received signal observed from the transverse component, m_{xy}, of $\boldsymbol{M}$ is

$$s_r(t) = \int_x \int_y \int_z m_{xy}(x,y,z,t)\, e^{-i\omega_o t} dx\, dy\, dz \tag{2.19}$$

where the baseband, demodulated received signal is

$$s(t) = \int_x \int_y \int_z m_{xy}(x,y,z,t)\, dx\, dy\, dz \tag{2.19}$$

ignoring relaxation[3]. Without gradients all spins will resonance at $\omega_o = \gamma B_o$ however with the addition of spatially varying gradients spatial localization can be achieved by encoding the spatial locations by varying their frequencies, $\omega(x) = \omega_o + \Delta\omega = \gamma(B_o + G_x x)$. Including the precession due to the application of a constant, linear gradient for a single dimension Eqn. (2.19) becomes

$$s(t) = \int_x m_{xy}(x,t) e^{-i\gamma G_x x t}\, dx \tag{2.20}$$[3].

Thus the acquired signal is the combination of the magnetization multiplied by phase, which maps the spatial locations. By supplementing $k_x(t) = \frac{\gamma}{2\pi} G_x t$, Eqn. (2.20) becomes

$$s(t) = \int_x m_{xy}(x) e^{-i2\pi k_x(t)x}\, dx \tag{2.21}$$

such that the received signal is just the Fourier transform of $m_{xy}(x,t)$[3].

$$s(t) = \Im\{m_{xy}(x)\} = M_{xy}(k_x(t)) \tag{2.22}$$

More generally, $k(t) = \frac{\gamma}{2\pi}\int_0^t G(\tau)d\tau$ for cases when G is not constant[3]. In two dimensions

$$s(t) = \int_x \int_y m_{xy}(x,y) e^{-i2\pi(k_x(t)x+(k_y(t)y)}\, dy\, dx \tag{2.23}$$

and

$$s(t) = \Im\{m_{xy}(x,y)\} = M_{xy}(k_x, k_y) \tag{2.24}.$$

The most basic sequence acquire an MRI image is the 2DFT shown in Figure 2.8. Whereby k-space is transversed via the running integral of the gradients. For this pulse sequence, an entire k_x line is acquired and this repeated with varying phase encode amplitudes G_y to cover a grid in k-space. The image is the 2D Fourier transform. Fourier theory[10], states that the object Field-of-View (FOV) is determined by the sampling rate Δk

$$FOV = \frac{1}{\Delta k} \tag{2.25}.$$

Thus to achieve a higher FOV more lines of k-space must be acquired, requiring a longer scan time. In k_y, reducing Δk_y is costly. Increasing the FOV_y by n requires n times number of phase encodes resulting in n fold increase in scan time for the same spatial resolution. In k_x, small Δk_x is easily achieved as this is limited by the hardware, which is very fast. Nyguist sampling requires $FOV > 2\Delta k$ however an anti aliasing filter can be applied in the readout direction due to the high sampling[10]. The spatial resolution is determined by

$$\delta = \frac{1}{K_{max}} = \frac{1}{n\Delta k} \quad (2.26).$$

K_{max} is the extend in k-space is determined by the number of samples n and the Δk[10]. Decreased resolution, δ, will result in improved image quality at the cost of SNR loss or increased scan time. SNR is determined by

$$SNR \sim \delta_x\, \delta_y\, \delta_z \sqrt{t_{AD,total}}\, f(\rho, T_1, T_2, \ldots) \quad (2.27)[3].$$

The parameter $t_{AD,total}$ is the total time the receiver is acquiring data. This parameter can be broken down as

$$t_{AD,total} = t_{AD} \times N_{PE} \times N_{avg} \quad (2.28).$$

where t_{AD} is the data acquisition time in a single TR, N_{PE} is the total number of phase encodes, and N_{avg} is the number of signal averages. For simplicity, the transverse decay effects are ignored, as increasing the acquisition time in a single TR will not provide any SNR benefit once the signal has decayed. This relationship demonstrates that improving SNR is costly in scan time. For instance a 2-fold improvement in resolution in two dimensions will result in an 4-fold decrease in resolution. To gain back this SNR, a 16-fold (4^2) increase in scan time is required.

The acquistion time in a single TR (t_{AD}) is can be described in terms of the receiver bandwidth (BW), which is inversely proportional the single-sample time t_s as

$$BW = \frac{1}{t_s} \quad (2.29)$$

such that

$$t_{AD} = N \times t_s = \frac{N}{BW} = \frac{1}{BWPP} \quad (2.30)$$

where $BWPP$ is the bandwidth-per-pixel[3]. The SNR can also be improved by increasing the $BWPP$.

2.2 Fundamentals of Magnetic Resonance Spectroscopy

2.2.1 Chemical Shift

Chemical shift is a result of the electron density, electronegativity of nearby groups, and anisotropic induced magnetic field effects[2]. Electron density can cause a chemical shift a it shields a nucleus from the external field. Nuclei in the vicinity of an electronegative atoms experience a reduction in electron density resulting in deshielding of the nuclei[2]. Anisotropic induced magnetization field effects are the result of an induced magnetic field as a result of the electron cloud revolving about the nucleus. This can result in either a paramagnetic effect when it is parallel to the applied field or diamagnetic when it is opposed[2].

These phenomena result in a change in the local magnetic field resulting in a change in frequency.

$$\omega = \gamma B_o(1 - \sigma) \quad (2.30)[3].$$

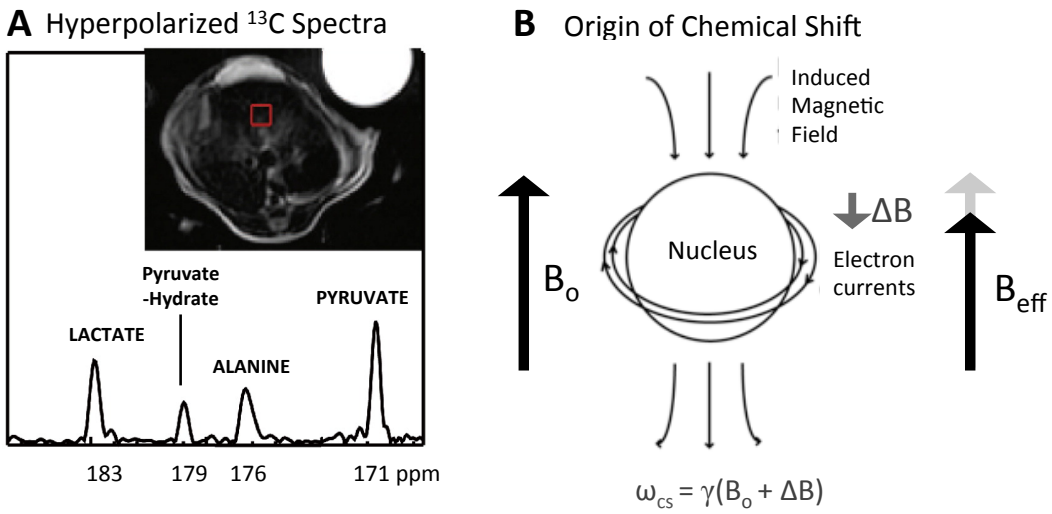

Figure 2.8: (a) A typical hyperpolarized ^{13}C spectrum is shown with the chemical shifts. **(b)** Chemical shift results from an induced magnetic field that changes the magnetic field experienced by the nuclei, $B_{eff} = B_o + \Delta B$. This results in a molecule dependent shift of the Larmor frequency. *(Adapted from Hu, S 2009).*

2.2.2 Exchange Spectroscopy

EXchange SpectroscopY (EXSY) is used to quantify dynamic processes of time scales from milliseconds to minutes. Physical processes include slow conformational changes including domain movement, ligand binding and release, topological interconversion or secondary structure and cis-trans isomerization[11,12]. Additionally, EXSY is used to quantify and detect chemical reactions and enzymatic conversions. EXSY requires that the $k \ll |\Delta\omega|$.

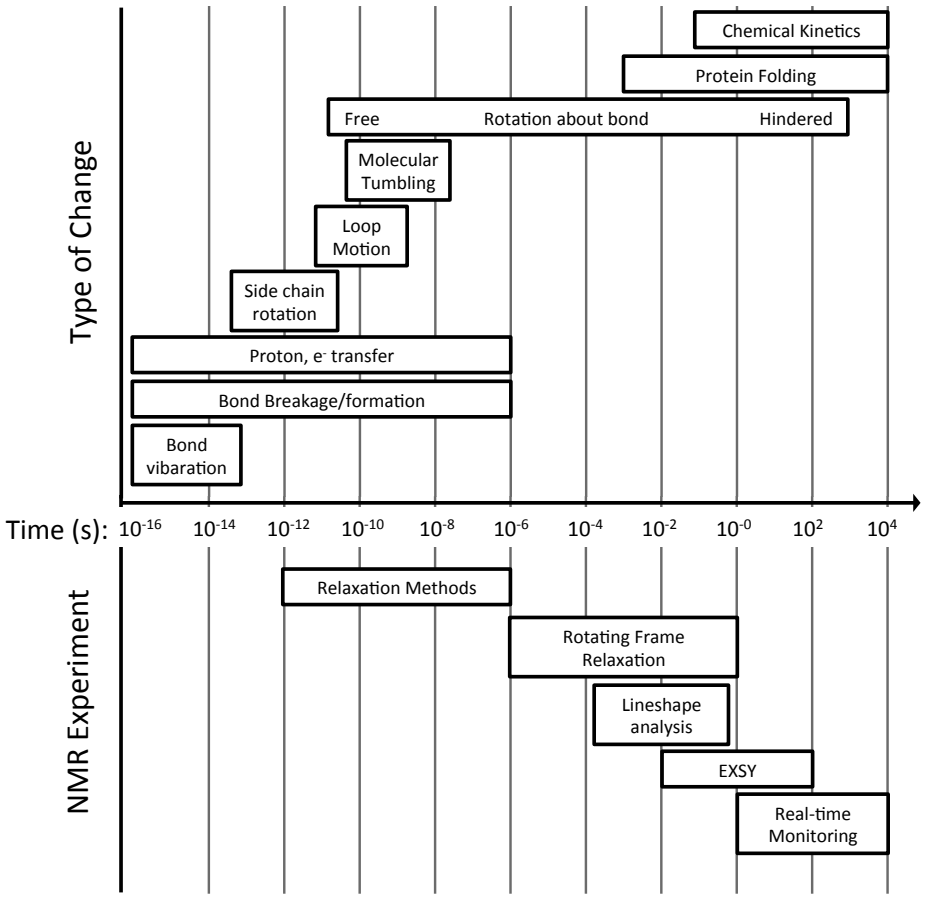

Figure 2.9: Timescales for molecular motions and NMR experiments that can be used to study them.

In one-dimensional NMR, the signal is recorded as a function of one time variable and then it's Fourier transformed is taken to obtain the spectrum. In two-dimensional NMR, the signal is recorded as a function of two time variables, t_1 and t_2. The two-dimensional spectra is acquired by two-dimensional Fourier transformed of two frequency variables[13].

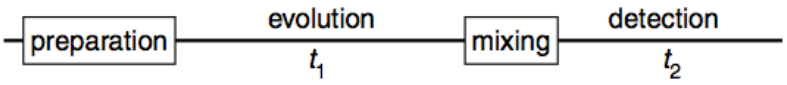

Figure 2.10: General scheme for two-dimensional spectroscopy.

To acquire two-dimensional spectra the pulse sequence shown in Figure 2.10 can be used. First, the magnetization is prepared with preparation pulses. The resulting magnetization

is then allowed to evolve for the first time period, t_1, storing the desired information in the longitudinal plane. This is followed by a mixing time as shown in Figure 2.10. After the mixing time the signal is recorded as a function of the indirect time variable, t_2. The exact design of the preparation and time periods determines the type information acquired[13].

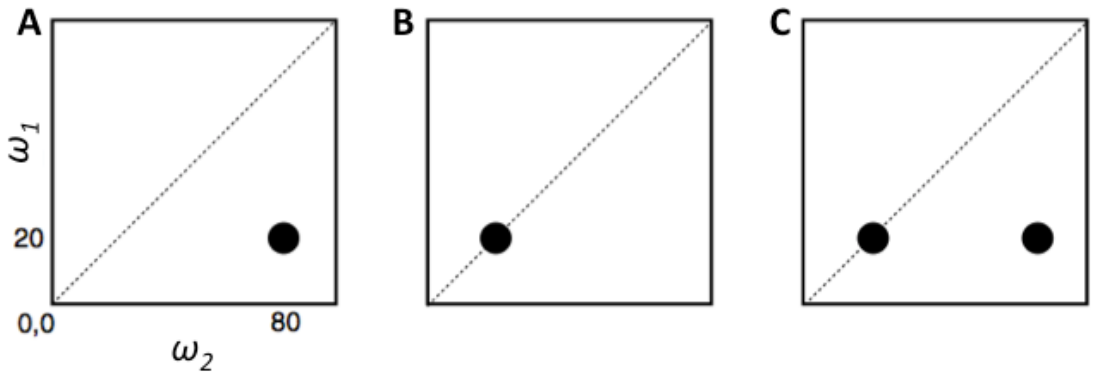

Figure 2.11: Schematic for interpretation of 2D NMR spectra.

To interpret two-dimensional spectrum consider a case where a peak appears at ω_1 = 20 Hz, ω_2 = 80 Hz (Figure 2.11a). This peak corresponds to spins resonate frequency was 20 Hz during the evolution time, t_1 (Figure 2.10). Then during the mixing time these *same* spins changed their resonance frequency evolving at 80 Hz during t_2 (Figure 2.11) is called a cross-peak.

Similarly, if there is a peak at ω_1 = 20 Hz, ω_2 = 20 Hz (Figure 2.11b) This spin was unaffected by the mixing period and thus continued to evolve at 20 Hz during t_2. In Figure 2.9c, a third case is considered where there are two peaks, one at ω_1 =20Hz, ω_2 =80Hz and another at ω_1 = 20Hz, ω_2 =20Hz. The means that a percentage of the spins were unaffected by the mixing period, continuing to evolve at 20 Hz during t_2 and the other percentage when changed their resonance frequency to 80 Hz during the mixing time

Figure 2.12: Basic pulse sequence for EXSY. To acquire the 2D spectra t_1 is varied. In the EXSY acquisition all pulse have 90° flip angles.

In the Exchange Spectroscopy (EXSY) experiment, a cross-peak arises from chemical exchange. The basic pulse sequence is shown in Figure 2.12. To acquire the full spectra the sequence is repeated with varying values of t_1 to sample the indirect dimension. The number of repetitions determines the spectral resolution in the indirect dimension based on Fourier theory and thus more time consuming similar to phase encoding.

$$\delta_{direct} = \frac{spectral\ width}{number\ of\ spectral\ points} \rightarrow time = t_2 \tag{2.31}$$

$$\delta_{indirect} = \frac{spectral\ width}{number\ of\ repetitions} \rightarrow time = reps \times t_2 \tag{2.32}$$

Often 2D spectra are acquired with varying mixing times, *TM*s, to generate build-up curves from the measured intensities. This data can then be fit to an exchange model to extract kinetic rates of conversion. For two-site exchange, the following three equations describe the three unique build-up curves.

$$I_{AA}(t) = P_A(P_A + P_B e^{-k_{ex}t})e^{-t/T_1} \tag{2.31}$$

$$I_{BB}(t) = P_B(P_B + P_A e^{-k_{ex}t})e^{-t/T_1} \tag{2.32}$$

$$I_{AB}(t) = P_A P_B(1 - P_A e^{-k_{ex}t})e^{-t/T_1} \tag{2.33}$$

These equations assume that the relaxation is the same in each state and solves for the effective rate of exchange rather than solving for each direction independently.

2.2.3 STimulated Echo Acquisition Mode (STEAM)

STimulated Echo Acquisition Mode (STEAM) is a sequence often used in spectroscopy. It consists of a train of same three 90° pulses described in the (EXSY) acquisition shown in Figure 2.13. The sequence is very useful for single voxel spectroscopy, as it conveniently has three 90° pulses whereby slice selective pulses can be played on each axis for 3D localization.

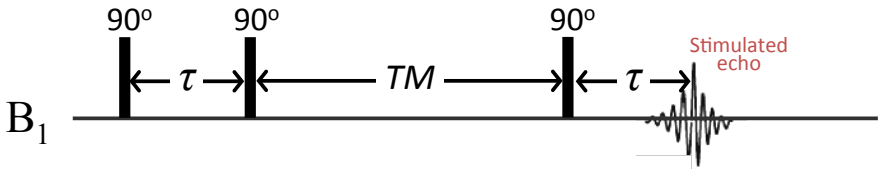

Figure 2.13: Schematic of a simplified STEAM sequence.

The sequence timings are chosen such that $T_2 \gg \tau$ for $SNR, TM \gg T_2$ or with a large crusher gradient during the mixing time such that the transverse magnetization fully decays during that time. This prevents parasitic magnetization in the stimulated echo. Here we will assume that $T_1 \gg TM$ and $T_1 \gg \tau$, which is the case for hyperpolarized substrates.

The magnetization, $\vec{M}(T)$, after the third pulse ($T = TM + 2\tau$) can be solved with rotation, $R_y(\pi/2)$, followed by free precession, another rotation from the second 90° pulse, another period of free precession, and finally a 90° followed by free precession. The derivation is shown below. Magnetization following first 90° pulse is given by

$$\vec{M}(0^+) = R_y(\pi/2)\vec{M}(0^-) = \begin{bmatrix} 0 & 0 & -1 \\ 0 & 1 & 0 \\ 1 & 0 & 0 \end{bmatrix} \begin{bmatrix} 0 \\ 0 \\ M_o \end{bmatrix} = \begin{bmatrix} -M_o \\ 0 \\ 0 \end{bmatrix} \quad (2.34).$$

This is followed by a period of free precession

$$\vec{M}(\tau^-) = R_z(\omega\tau)\vec{M}(0^+) = \begin{bmatrix} cos(\omega\tau) & sin(\omega\tau) & 0 \\ -sin(\omega\tau) & cos(\omega\tau) & 0 \\ 0 & 0 & 1 \end{bmatrix} \begin{bmatrix} -M_o \\ 0 \\ 0 \end{bmatrix} = \begin{bmatrix} -M_o cos(\omega\tau) \\ M_o sin(\omega\tau) \\ 0 \end{bmatrix} (2.35).$$

The second 90° pulse results in the following magnetization

$$\vec{M}(\tau^+) = R_y(\pi/2)\vec{M}(\tau^-) = \begin{bmatrix} 0 & 0 & -1 \\ 0 & 1 & 0 \\ 1 & 0 & 0 \end{bmatrix}\begin{bmatrix} -M_o cos(\omega\tau) \\ M_o sin(\omega\tau) \\ 0 \end{bmatrix} = \begin{bmatrix} 0 \\ M_o sin(\omega\tau) \\ -M_o cos(\omega\tau) \end{bmatrix} \quad (2.36).$$

During the mixing time, *TM*, all of the magnetization in the transverse plane decays; intuitively this will result in a 50% signal loss.

$$\vec{M}(TM^-) = \begin{bmatrix} 0 \\ 0 \\ -M_o cos(\omega\tau) \end{bmatrix} \quad (2.37).$$

The third 90° pulse followed by a period of free precession gives $\vec{M}(T)$

$$\vec{M}(TM^+) = R_y(\pi/2)\vec{M}(TM^-) = \begin{bmatrix} 0 & 0 & -1 \\ 0 & 1 & 0 \\ 1 & 0 & 0 \end{bmatrix}\begin{bmatrix} 0 \\ 0 \\ -M_o cos(\omega\tau) \end{bmatrix} = \begin{bmatrix} M_o cos(\omega\tau) \\ 0 \\ 0 \end{bmatrix} \quad (2.38)$$

$$\vec{M}(T) = R_z(\omega\tau)\vec{M}(TM^+) = \begin{bmatrix} cos(\omega\tau) & sin(\omega\tau) & 0 \\ -sin(\omega\tau) & cos(\omega\tau) & 0 \\ 0 & 0 & 1 \end{bmatrix}\begin{bmatrix} M_o cos(\omega\tau) \\ 0 \\ 0 \end{bmatrix} = \begin{bmatrix} M_o cos^2(\omega\tau) \\ -M_o cos(\omega\tau) sin(\omega\tau) \\ 0 \end{bmatrix}$$

(2.39).

Signal is just the integral of the spins over the volume.

$$s(T) = \int_V \begin{bmatrix} M_o cos^2(\omega\tau) \\ -M_o \cos(\omega\tau)\sin(\omega\tau) \\ 0 \end{bmatrix} \quad (2.40)$$

Assuming the variation in $\Delta\omega$ is sufficiently high across the voxel volume, *V*, in other words $\varphi(\vec{x})$ ranges from $-\pi$ to π. $\Delta\omega$ in the absence of gradient would be due to inhomogeneity (T_2^* line broadening, imperfect shimming) the imagery term integrates to zero.

$$s(T) = \int_{-\pi}^{\pi} M_o \cos(\varphi(\vec{x}))\sin(\varphi(\vec{x}))d\vec{x} - i\int_{-\pi}^{\pi} M_o cos^2(\varphi(\vec{x}))d\vec{x} = \frac{1}{2}M_o \quad (2.41)$$

The real and imaginary components of the signal are the following

$$Re\{s(T)\} = \frac{1}{2}M_o \qquad \text{and} \qquad Im\{s(T)\} = 0 \quad (2.42)$$

with $\varphi = 0$. However if a spin, went through exchange during the mixing time, ω_{cs}, TM. The magnetization time T would be following:

$$\vec{M}(T_{cs}) = R_z(\omega_{cs}\tau)\vec{M}(TM^+) = \begin{bmatrix} M_o cos(\omega_o\tau)\cos(\omega_{cs}\tau) \\ -M_o cos(\omega_o\tau) sin(\omega_{cs}\tau) \\ 0 \end{bmatrix} \quad (2.43).$$

Integrating over the volume

$$s(T) = \int_{-\pi}^{\pi} M_o \cos(\varphi(\vec{x}))\sin(\varphi_{cs}(\vec{x}))d\vec{x} - i\int_{-\pi}^{\pi} M_o \cos(\varphi(\vec{x}))\cos(\varphi_{cs}(\vec{x}))d\vec{x} = \frac{1}{2}M_o e^{i\Delta\varphi(\omega_o,\omega_{cs})} \quad (2.44)$$

yields the following real and imaginary components of the signal

$$Re\{s(T)\} = \frac{1}{2}M_o sin(\Delta\varphi(\omega_o,\omega_{cs})) \quad \text{and} \quad Im\{s(T)\} = \frac{1}{2}M_o sin(\Delta\varphi(\omega_o,\omega_{cs})) \quad (2.45).$$

By choosing τ such that the cumulative phase shift is $\pm\,\pi/2$,

$$\Delta\varphi(\omega_o,\omega_{cs}) = (\omega_{cs} - \omega_o)\tau = 2\pi(f_{cs} - f_o)TE/2 = \pi/2 \pm k\pi \quad (2.46)$$

all spins undergoing exchange will be observed solely in the imaginary signal channel[14,15]:

$$Re\{s_{cs}(T)\} = 0 \quad \text{and} \quad Im\{s_{cs}(T)\} = \frac{1}{2}M_o \quad (2.47).$$

If the acquired signal consists of both exchanging and non-exchange spins the acquired signal would be

$$s_{tot}(T) = M_o(1-a) + iaM_o \quad (2.48).$$

where a is the percentage of spins that have gone through exchange. This is the basis for the metabolic activity decomposition (MAD) method. As mention previously sufficient spatial variation is key to the execution of this technique. To ensure adequate modulation dephasing/rephrasing gradients can be added as shown in Figure 2.14. This is very important in its application to hyperpolarized substrates where measured T_2s are long.

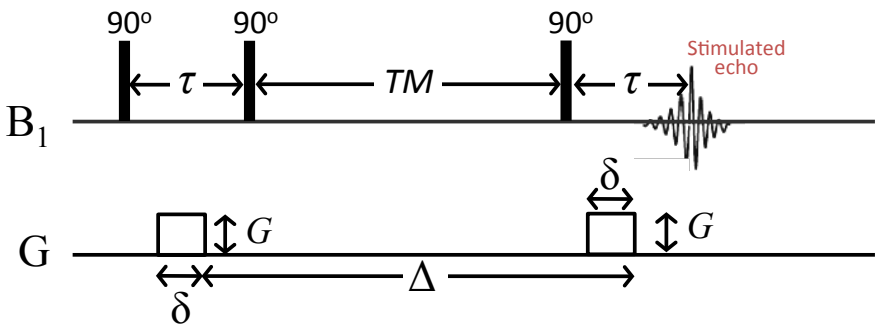

Figure 2.14: Diffusion-weighted stimulated echo sequence (STEAM) which can also be used for in "phase tagging" for Metabolic Activity Decomposition (MAD) reconstruction. Different *b-values* can be achieved by varying the amplitude of *G*.

The gradients are added to ensure "phase tagging" via frequency modulation in space as shown in Figure 2.15.

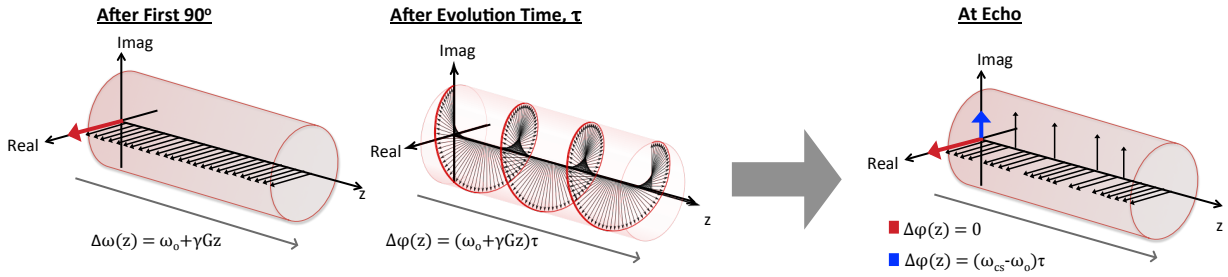

Figure 2.15: Phase "Tagging": The application of a G imparts a linear modulation $\Delta\omega(z) = \omega_o+\gamma Gz$. After the evolution time, τ, $\Delta\varphi(z)$ will be accrued. The second and third 90° pulses flip the direction of the rotation. Similar to a spin echo the spins angular frequency will reverse direction and will thus rephrase $TE/2$. If a spin goes through chemical exchange it will rotate at a new angular frequency, ω_{cs} resulting in phase accrual, $\Delta\varphi\,(z) = (\omega_o+\gamma Gz)\tau - (\omega_{cs}+\gamma Gz)\tau = (\omega_o-\omega_{cs})\tau$.

The STEAM sequence is also used in diffusion MRI. The spatial variation, $\omega(z) = \omega_o + \gamma Gz$, imparted by the gradients shown that results in a stimulated echo (Figure 2.14) can also be used for diffusion imaging.

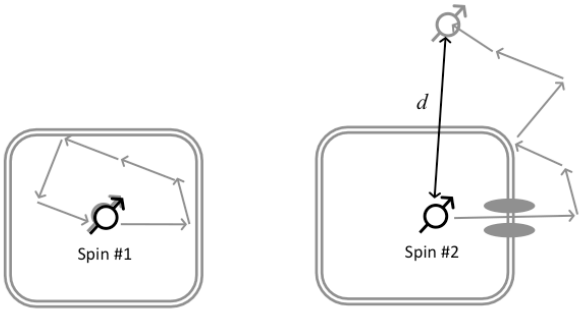

Figure 2.16: Schematic of a stationary and a diffusing spin.

Consider a spin #1 shown in Figure 2.16. After the first 90°, spin #1 will have an angular frequency of $\omega = \omega_o + \gamma G z_o$ and following the first period of phase accrual, τ, the phase of spin #1 will be $\varphi_1(\tau) = (\omega_o + \gamma G z_o)\tau$. After the third 90° and a period of phase accrual, τ, spin #1 will have and angular frequency $-\omega$ giving

$$\varphi_1(T) = (\omega_o + \gamma G z_o)\tau - (\omega_o + \gamma G z_o)\tau = 0 \tag{2.49}$$

where $T = TM + 2\tau$.

Spin #2 however will have an angular frequency of $\omega = \omega_o + \gamma G(z_o + d)$ after the third 90° pulse. This will result in the following phase

$$\varphi_2(T) = (\omega_o + \gamma G(z_o + d))\tau - (\omega_o + \gamma G z_o)\tau = \gamma G d \tau \tag{2.50}.$$

Comparing an ensemble of spins #1 to an ensemble of spin #2 with randomly varying diffusion distances, *d.* The spins in group #1 will have no signal loss due to dephasing. However the spins in group #2 will signal loss, attenuation, due to incoherent dispersion of phasing from this motion.

The Bloch equation accounts for decay via precession, T_2 relaxation, and T_1 relaxation but must be modified for signal attenuation due to diffusion with the application of a spatially varying gradient. The modified Bloch equation, has a diffusion term based on Fick's First Law and mass conservation. The Bloch-Torrey Equation[16], is:

$$\frac{d\boldsymbol{M}}{dt} = \boldsymbol{M}\times\gamma\boldsymbol{B} - \frac{m_x\hat{\imath}+m_y\hat{\jmath}}{T_2^*} - \frac{(m_z-M_o)\hat{k}}{T_1} + \nabla\cdot\boldsymbol{D}\nabla\mathbf{M} \tag{2.51}$$

where $\boldsymbol{D}$ is the diffusion tensor. In the most simple case, which is the only case addressed in this dissertation is isotropic diffusion where the diffusion tensor is a multiple of the identity matrix[16]:

$$\boldsymbol{D} = \boldsymbol{D}\cdot\boldsymbol{I} = D\begin{bmatrix}1 & 0 & 0\\ 0 & 1 & 0\\ 0 & 0 & 1\end{bmatrix} \tag{2.52}.$$

In this case, the solution to the Bloch-Torrey Equation is:

$$M = M_{bloch}e^{-\frac{1}{3}\gamma^2G^2t^3} \sim M_{bloch}e^{-bD} \tag{2.53}.$$

This D is theoretical and the measured value, which is a result of the addition of diffusion sensitizing gradients, is called to as the *apparent diffusion coefficient* (ADC). M_{bloch} is the magnetization without diffusion weighting from the bloch equation and $b-value$ refers to the pulse sequence parameters that provide sensitivity to diffusion[17]. With increased sensitivity to diffusion there is a loss in *SNR* described by the following equation[17]:

$$S(TE) = S_o e^{-\gamma^2G^2\delta^2(\Delta-\frac{\delta}{3})ADC} \tag{2.54}$$

where Δ is the diffusion time, δ is the duration of the gradient, G is the gradient strength, and S_o is the signal intensity without diffusion weighting.

2.2.4 Chemical Shift Imaging

Chemical shift imaging (CSI) also called magnetic resonance spectroscopic imaging (MRSI) is an extension of MR spectroscopy. CSI allows for the detection of the distribution of multiple metabolites in an excited region. With the addition of a spectroscopy dimension, the following baseband, demodulated signal is received[6]:

$$s(t) = \int_x \int_y \int_z \; m_{xy,0}e^{-i2\pi f_o t} + m_{xy,1}e^{-i2\pi f_1 t} \ldots m_{xy,n}e^{-i2\pi f_n t})\; dx\, dy\, dz \tag{2.55}$$

Thus, a k-space interpretation can be applied in the spectral domain where

$$k_f = t \tag{2.56}.$$

Unlike k_x and k_y, k_f is not traversed with the application of gradients but rather in the absence of the gradients as with traditional NMR. The addition can be costly in scan time where the total scan time for simple 2DFT imaging acquisition, pulse sequence and k-space trajectory show in Figure 2.15, is

$$total\ scan\ time \approx\ t_{ro} N_{PE} N_{avg} t_{prep} TR \tag{2.57}$$

Where t_{ro} is the readout time, N_{PE} is the number of phase encodes, N_{avg} is the number of averages and t_{prep} is a preparation time that varies between pulse sequences. With the addition spectroscopy the total scan time becomes

$$total\ scan\ time\ \approx\ t_{AD} N_{FE} N_{PE} N_{avg} t_{prep} TR \tag{2.58}$$

Where t_{AD} is the data acquisition time for spectroscopy. The addition results in a factor of N_{FE}, the number of frequency encodes (readout dimension), increase. In Figure 2.17d shows the additional lines of K_x line that must be sampled. Thus the addition of spectroscopy is time intensive. Echoplanar spectroscopic imaging (EPSI) is a fast alternative, although there are many others where both K_x and K_f are sampled during t_{AD} as shown in figure 2.17e and 2.17f.

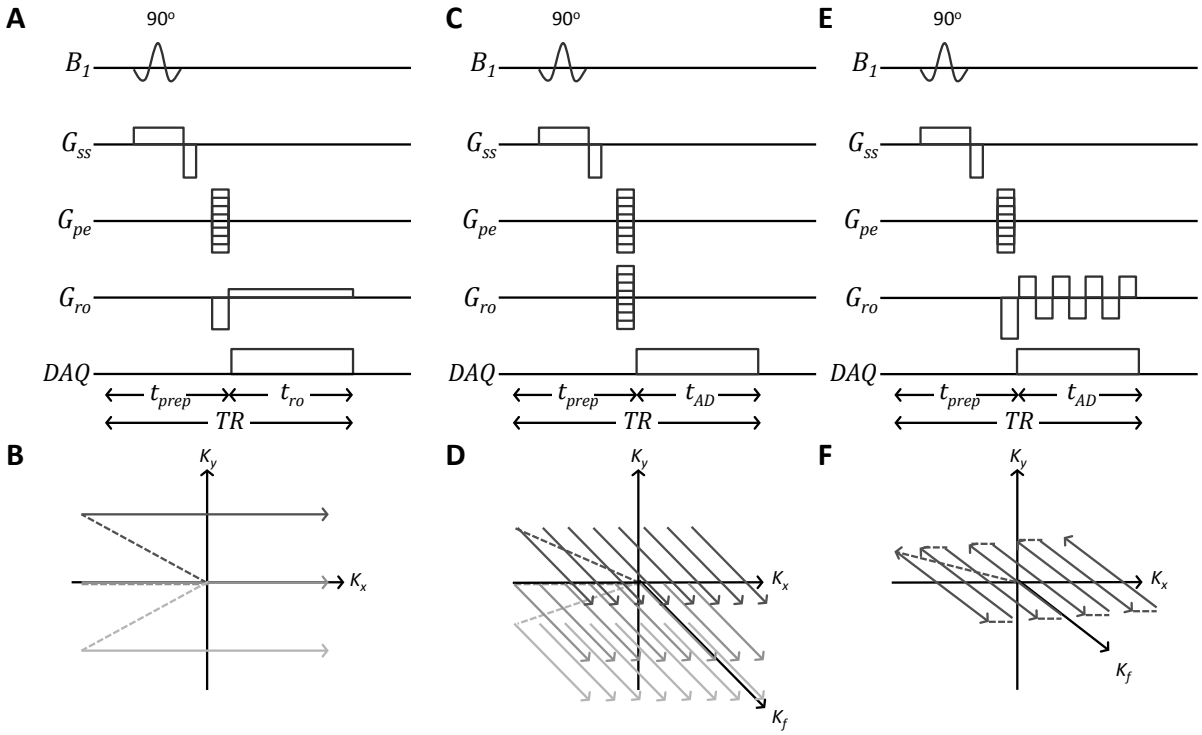

Figure 2.17: (a) Pulse sequence and **(b)** k-space trajectory for a simple 2DFT (Only three phase encodes are shown). **(c)** Pulse sequence and **(d)** k-space trajectory with the addition of spectroscopy (Only three phase encodes are shown). **(e)** Pulse sequence and **(f)** k-space trajectory for echoplanar spectroscopic imaging (EPSI) (Only one phase encode is shown) .

By Fourier theory[10], the spectral resolution is governed by

$$spectral\ resolution\ (Hz) = \frac{1}{t_{AD}} \tag{2.59}$$

where t_{AD} is the acquisition duration and the spectral width as called the spectral *FOV*

$$spectral\ width\ (Hz) = \frac{1}{\Delta t_s} = \frac{n}{t_{AD}} \tag{2.60}$$

where Δt_s is the time between samples and n is the number of samples. Similar to k-space principles discussed previously, improved spectral resolution requires increased scan times and a larger spectral width requires finer sampling, Δt_s which reduces k_f.

2.3 Hyperpolarization

2.3.1 Dynamic Nuclear Polarization

NMR/MRI is a very powerful across a wide range of disciplines and in the clinic. However,

its inherent low sensitivity is a major challenge. This is due to the small magnetic moment of the nuclei resulting in a very small polarization as shown in section 2.1.1. Therefore to detect low concentration metabolites and nuclei with low natural abundance or low gyromagnetic rations, time intensive signal averaging is required to obtain an acceptable *SNR*.

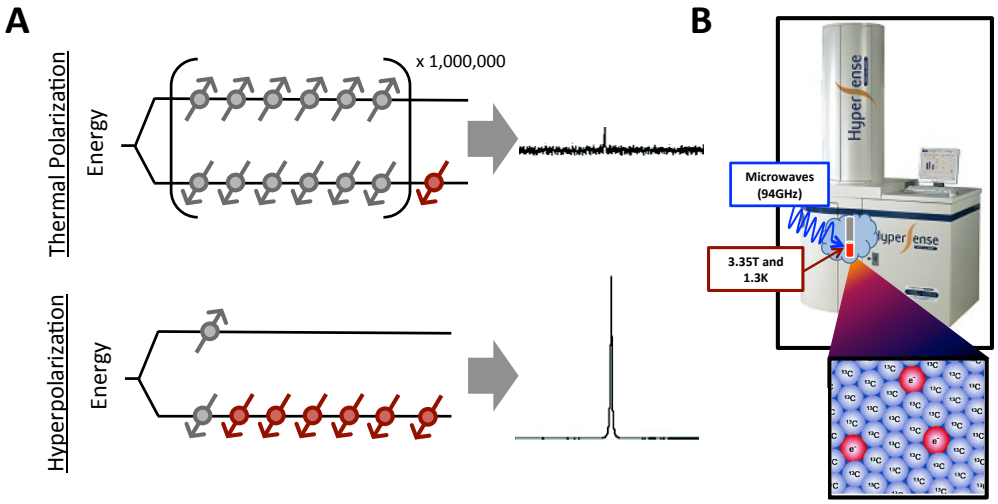

Figure 2.18: (a) Hyperpolarization provides dramatic increases in the difference between aligned and anti-aligned nuclei resulting in >10,000 fold increases in SNR. **(b)** Dynamic nuclear polarization (DNP) transfers polarization to nuclei of interest. This is accomplished by placing nuclei in the proximity of electrons and transferring energy via microwave irradiation at low temperature in a high magnetic field. $^{13}C_1$ –Pyruvate molecules near a molecule containing a free radical, which provides the electron. *(Adapted from Schroder, M 2011).*

Dynamic nuclear polarization (DNP) can overcome these challenges in polarization resulting in dramatic increases in SNR (>10,00 fold)[4]. DNP is the transfer of spin polarization from electrons to nearby nuclei. The nuclei to by hyperpolarized are placed in the proximity of electrons provided with the addition of a free radical. Energy is transferred via microwave irradiation at low temperature in a magnetic field.

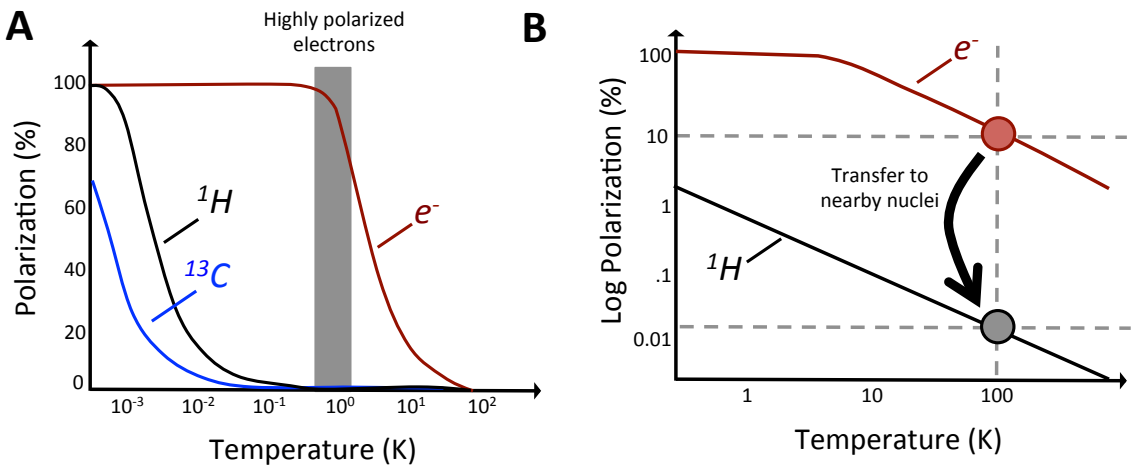

Figure 2.19: Temperature dependence of the electron, carbon and proton nuclear spin reservoir polarization at high magnetic field. At low temperature and high magnetic field the polarization of an electron is near 100% making ideal for high efficiency transfer

The alignment of electron spins is described by the Boltzmann distribution (Section 2.1.1) under the thermal equilibrium[2]. Electrons have an inherently much higher polarization shown in Figure 2.17. For instance, the polarization of protons at 90 K is 0.016% meanwhile the polarization of electrons is 10.541% - 660 fold increase Furthermore, the polarization of the electrons in also increased by placing the sample in a high magnetic field and at low temperature[2].

2.3.2 Past and Recent Work on Carbon-13 Hyperpolarized MR

Magnetic resonance spectroscopy (MRS) of hyperpolarized substrates shows great promise in the development of new clinically relevant diagnostic indicators of disease[18–22]. ^{13}C MRS, in conjunction with DNP, is a highly promising method to detect alterations in tissue metabolism. Hyperpolarization allows the detection of phenomena, such as *in vivo* pyruvate-to-lactate conversion[23,24], by increasing signal-to-noise ratio by a factor of >10,000 (described in Section 2.3.1), allowing for the detection of carbon-13 probes of endogenous, nontoxic, nonradioactive substances *in vivo*. Thus, this method provides a powerful tool to investigate tissue metabolism *in vivo*. The value of this powerful new technology for cancer diagnostics

was first shown by Golman et al.[24] and it has been applied in a large number of studies for detecting cancer presence, progression, and response to therapy providing unprecedented new information[18–22].

[1-^{13}C] Pyruvate is the most widely studied of the hyperpolarized ^{13}C probes because of its key role in metabolism at an important juncture between glycolysis and the citric acid cycle[25,26] and its ability to report on the Warburg effect observed in many cancer cells. Moreover, [1-^{13}C] pyruvate has superb properties for DNP as it has a long longitudinal relaxation time T_1, a high level of polarization providing adequate SNR, and is readily taken up by cells. In preclinical studies, [1-^{13}C] pyruvate has been used to monitor tumor progression, formation, and response to therapy[18–22,27–29]. Following these promising preclinical studies, the technology has been translated into a clinical trial using HP [1-^{13}C] pyruvate in prostate cancer patients, which showed feasibility, safety and great promise for hyperpolarized carbon-13 technology[20].

2.3.3 Past and Recent Work on Hyperpolarized [1-^{13}C]-Pyruvate

Hyperpolarized [1-^{13}C]-pyruvate, in particular, has shown great promise as a potential probe for the presence of disease and its response to treatment[18–22,27–31]. Pyruvate is an important product of the glycolytic pathway, playing a central role in cellular metabolism[32]. In most normal tissues under aerobic conditions, pyruvate dehydrogenase catalyzes the decarboxylation of a significant fraction of pyruvate to produce acetyl-coenzyme A, which is then used in the tricarboxylic acid cycle (TCA). Alternatively, pyruvate can be reduced to lactate in the reaction catalyzed by lactate dehydrogenase (LDH). In the presence of disease, however, the relative fluxes through these enzymes can be significantly altered. For instance, even under aerobic conditions, the glycolytic flux in

tumors is often upregulated[26], which leads to higher concentrations of lactate and an acidic tumor microenvironment[32].

2.4 Adaptations in Cancer

2.4.1 Cancer Metabolism

Metabolism has been associated with cancer since the early days of cancer research where Otto Warburg observed aerobic glycolysis in cancer cell[26]. At this time it was believed that metabolic signatures seen in cancer were solely response to damage of the mitochondria. However, recent work has shown that in fact cancer cells reprogram their metabolic network to support proliferation, survival, and migration[32]. Recently, it has been shown that oncogenes initiate a cascade that lead to dramatic rewiring of metabolic signaling pathways. Moreover, certain metabolites, such as 2-hydroxyglutarate (2-HG)[33,34] and fumarate[35–37], have been shown to be oncogenic themselves. Thus, it is no longer believed that aberrant metabolism is a passive result but that it is a key hallmark feature that drives cancer formation, progression, and invasion[32].

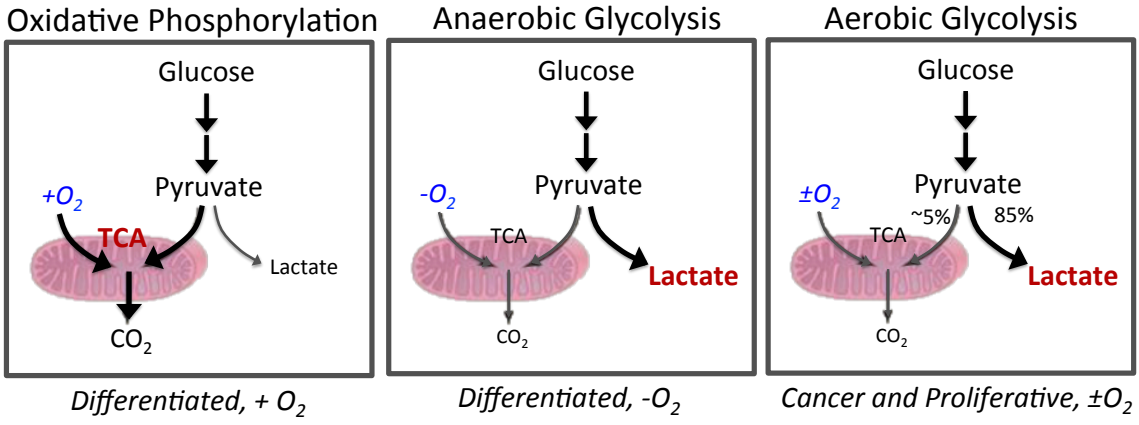

Figure 2.20: (left) In normal, differentiated tissue pyruvate is primarily metabolized in the mitcondria via oxidative phosphorylation and only in hypoxia (lack of oxygen) is pyruvate converted to lactate, namely anaerobic glycolysis. However, in proliferative tissue and tumors pyruvate is readily and preferentially converter to lactate even in the presence of oxygen by aerobic glycolysis *(Adapted from Vander Heiden 2009).*

There are a number of key characteristic attributes of the tumor metabolome. The most notable is the Warburg effect whereby high amounts of lactate are produced from aerobic glycolysis (Figure 2.20). In normal, differentiated tissue pyruvate is primarily metabolized in the mitocondria via oxidative phosphorylation and only in hypoxia (lack of oxygen) is pyruvate converted to lactate, namely anaerobic glycolysis[26]. However, in proliferative tissue and tumors, pyruvate is readily and preferentially converter to lactate even in the presence of oxygen by aerobic glycolysis. This is called the Warburg effect, which a key marker that distinguishes cancer cells from normal cells. The majority of the work in the hyperpolarized carbon-13 MR field has focused on trying to both understanding this phenomenon and utilize it as a diagnostic tool.

The Warburg effect can often inhibit glycolysis, which is also known as Pasteur effect[38]. The Pasteur effect is a result of a dysfunctional mitochondria and the reduced efficiency in ATP production per unit of glucose consumed. Additionally, because cancer cells often utilize glucose for anabolic processes[39] (Figure 2.21) to produce nucleic acids and proteins necessary for proliferation, cancer cells tend to have an abnormally high rate of glucose and glutamine uptake to meet their increased metabolic needs[40].

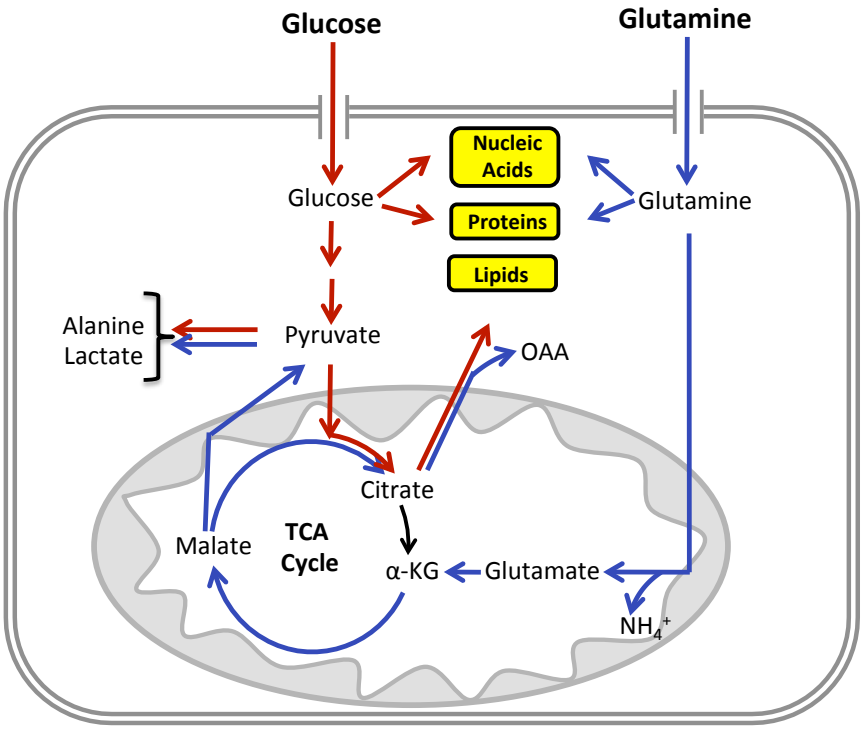

Figure 2.21: Cancer Metabolism: Glucose and Glutamine are the primary fuel sources for cancer cells. Glucose and Glutamine pathways shown in red and blue, respectively. Pyruvate, the end product of glycolysis is converted to lactate via the Warburg effect. Glucose and glutamine are used for anabolic processes producing nuclei acid and proteins necessary for proliferation. Glutamine can also supplement the TCA cycle *(Adapted from Debardinis, RJ et al. 2010).*

2.4.2 Oncogenes

An oncogene is a gene that has the potential to cause cancer. In cancer cells, an oncogene is often mutated or upregulated. Most oncogenes require an additional step to drive cancer such as the upregulation of another gene or environmental factors for cancer to occur[41]. The first oncogene, src, was discovered in 1970 and it was then demonstrated that oncogenes are activated proto-oncogenes discovered by Varmus and Bishop in 1976 leading to a Nobel Prize[42].

A proto-oncogene can become an oncogene by a small modification of its original function. There are three mechanisms of oncogene activation shown in Figure 2.22. The first is

mutation of the proto-oncogene or within a regulatory region[43]. A mutation can cause a change in the protein structure, which could result in oncogenic change in protein activity or loss of regulation (no change in protein expression levels)[43]. Another mechanism for oncogene activation is gene amplification. Misregulation or gene duplication can cause increased protein expression. Increases mRNA stability can also prolongs the proteins presence in a cell. The third mechanism is chromosomal rearrangement. Translocation events that move a proto-oncogene to a new site can lead to activation. Translocation events can also lead to the fusion of a proto-oncogene to another protein that together has oncogenic activity[43,44].

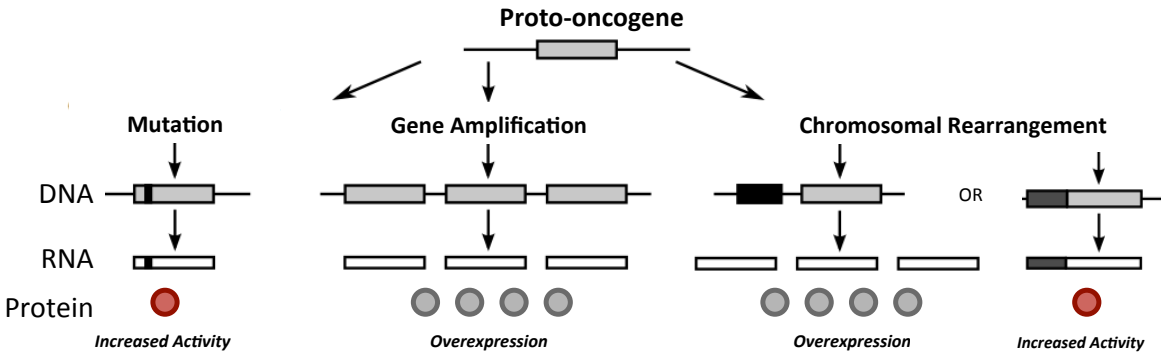

Figure 2.22: There are three mechanisms for the activation of a proto-oncogene. A *mutation* via deletion of point mutation in a coding sequence can produce a hyperactive protein expressed in normal levels. *Gene Amplification* can cause overexpression of the normal protein. Chromosomal rearrangement can cause nearby regulatory sequences to overexpression normal protein or fusion to an actively transcribed gene overexpressed the fusion protein or the fusion protein can be hyperactive *(Adapted from Barillot, E et al 2012)*.

In this dissertation, the Myc and Ras oncogenes are studied. Both Ras and Myc are two of the most frequently found alterations in cancer. Ras is a regulatory GTPase found on the cellular membrane[45]. It is involved in signaling that leads to cell proliferation. Specifically, Ras is a key regulator of the MAPK/ERK Pathway, which can be treated with targeted therapies such as Sorafenib[46–48]. Myc is a transcription factor found in the nucleus. Myc

regulates the transcription of genes that induce cell proliferation[49,50]. One of the hallmarks of Myc is its ability to promote cell-cycle progression. CDK inhibitors have been able to which has been effectively treat Myc induced cancers[51]. Thus the diagnosis of oncogene activation in cancer is highly significant as it could used in treatment planning, ultimately leading to improved patient outcomes.

2.4.3 Enzyme Kinetics and Lactate Dehydrogenase

Enzymes are typically proteins that manipulate other target molecules, called substrates. Substrates bind to an enzyme's active site are transformed into new molecules termed products[52]. The enzymatic mechanism describes the steps that the enzyme takes to produce its products[53]. Enzyme kinetics is the study of the reaction rate of these mechanisms and how various conditions can affect this rate. Enzyme kinetics provides information on the enzymes role in metabolism and how it will behave in a living organism.

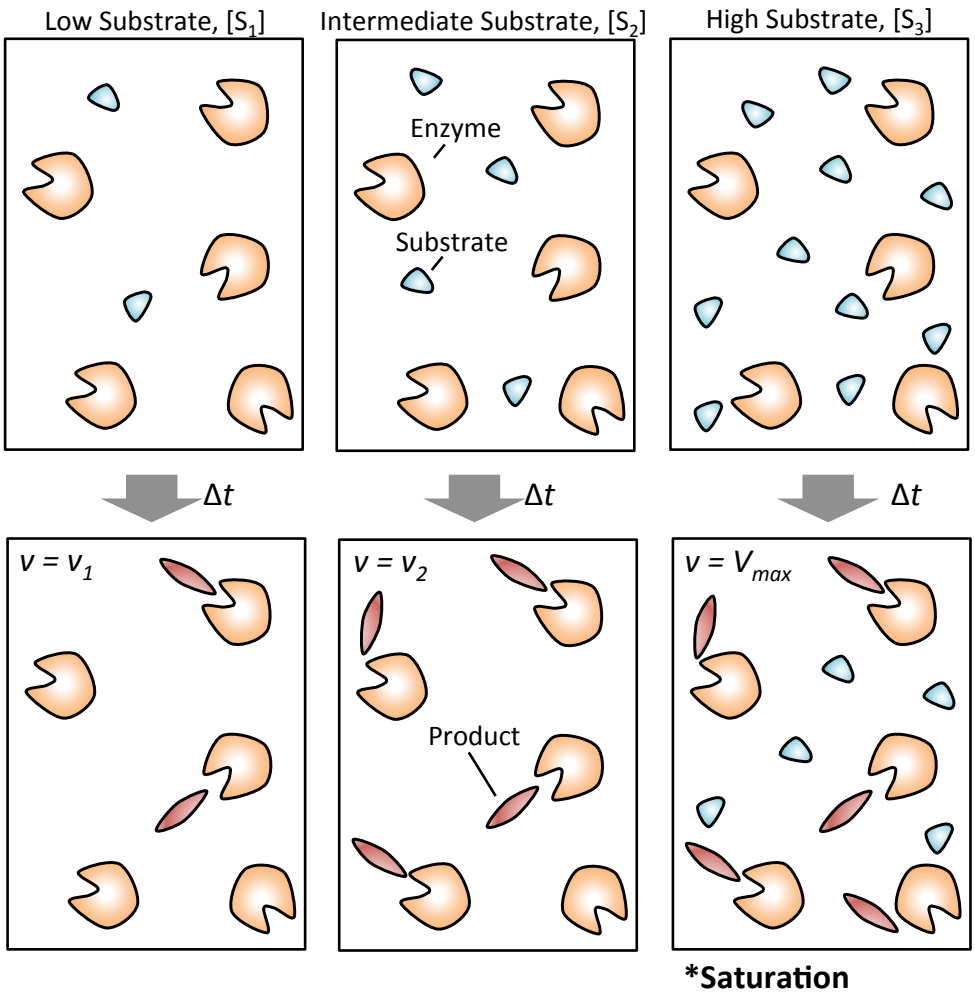

Figure 2.23: Schematic of enzyme saturation: At low concentrations there are plenty of active sites on the enzymes for the substrate molecules (pink circles) to interact. If more of the substrate is added and there are still plenty of active sites the rate of reaction will increase. However, when the substrate concentration outweighs the number of available active sites. The reaction rate will have reached its maximum, V_{max}.

As the concentration of substrate increases, the enzyme, E , will become saturated. Thus the rate of reaction, v, is not a linear response to the substrate concentration, [S], upon saturation. Eventually, the rate will reach a maximum, V_{max} (shown in Figure 2.23)[53]. Graphically, saturation is depicted in Figure 2.24.

Michaelis-Menten kinetics is the most widely used model to describe enzyme kinetics due to its simplicity and robustness. In this model the enzyme, E, binds with the substrate, S, to

form the *ES* complex. The *ES* complex is then converted to the product, *P*, and the enzyme, *E*[54].

$$E + S \underset{k_-}{\overset{k_+}{\leftrightharpoons}} ES \xrightarrow{k_{cat}} E + P \tag{2.61}$$

Where k_+ and k_- are rate constants that describe the enzyme-substrate binding which is reversible and k_{cat} describes the catalytic step. The actual enzymatic mechanism for $ES \xrightarrow{k_{cat}} E + P$ can be quite complex. However, this is usually one rate-determining enzymatic step allowing for the reaction to be modeled with a single rate constant. The model also assumes no inhibition or cooperatively[54].

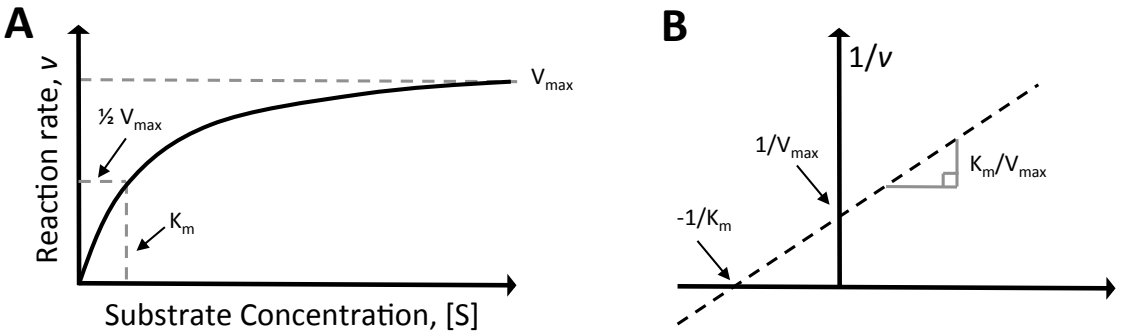

Figure 2.24: (a) Relationship between substrate concentration and reaction rate. **(b)** For ease of interpretation kinetic data can be shown on a Lineweaver–Burk (double-reciprocal) plot *(Adapted from Mathews et al. 1999).*

The Michaelis-Menten equation is

$$v_o = \frac{V_{max}[S]}{K_M + [S]} \tag{2.62}.$$

It describes how the reaction rate, v_o, depends on model shown in Eqn. 2.61. The constant V_{max} describes the maximum velocity and relates to Eqn. 2.61 by

$$V_{max} \overset{\text{def}}{=} k_{cat}[E]_{tot} \tag{2.63}.$$

K_M describes the how quickly the enzyme is saturated, time to reach half the maximum and is given by

$$K_M \stackrel{\text{def}}{=} \frac{k_{cat}+k_-}{k_+} \quad (2.64)[54].$$

The lactate dehydrogenase enzyme (LDH) is clinically significant because it is activity is augmented in a number of diseases[55,56]. Noncancerous conditions that can raise LDH levels such as heart failure, anemia, or muscle fatigue[57]. In cancer, LDH is involved in tumor initiation and metabolism due to cancer cells' increased reliance on aerobic glycolysis to meet high energetic demands[32].

The LDH enzyme is a tetramer (four subunits) composed of M and H protein subunits encoded by the *LDHA* and *LDHB* genes, respectively[58]. There are five isoenzymes. In cancer, fermentative glycolysis is catalyzed by the A form of LDH, whereby cells convert the majority of their glucose into lactate regardless of oxygen availability. LDH catalyzes the interconversion of pyruvate and lactate with concomitant interconversion of NADH and NAD^+. Thus, the availability of co-factors, NADH and NAD^+, can affect the enzyme-catalyzed conversion of pyruvate to lactate. For instance, NAD^+ is involved in pathways that regulated transcription, DNA repair, cell cycle progression, apoptosis, proliferation, and survival and is altered in cancer metabolism[54].

2.4.4 Monocarboxylate Transporters and Their Clinical Significance

As discussed previously, cancer cells produce high levels of the metabolite lactate due to a dysfunctional mitochondria and aerobic glycolysis. Lactate can then be transferred to other

cells as fuel sources. In normal physiology this occurs between in skeletal muscle and the brain, called “lactate shuttle” and within the brain between energy producing astrocytes and high energy consuming neurons, called “neuron-glia metabolic coupling”[59–61]. Cells possess mono-carboxylate transporters (MCTs), that transfer lactate between cells. MCTs have varying affinities for different metabolites. For instance, MCT1 and MCT2 (found in mice) primarily transport lactate into the cell, but actually have a higher affinity for pyruvate[62–65]. MCT4 on the other hand preferentially exports lactate out of the cell. MCT4 expression can be induced by hypoxia. This is regulated by the HIF1-α (hypoxia inducible factor)[66,67], a direct target of Myc.

While it was known that in cancer cells MCT4 regulates the excretion of lactate produced by glycolysis, it has recently been shown that MCT4 is involved in tumor growth and infiltration[68]. Moreover, it has been shown that MCT4 expression is indicative of an aggressive phenotype in a number of cancers[68–70]. High MCT4 export has a major role in creating the high lactate levels that correlate with corresponding increased metastasis, tumor recurrence, and poor outcomes. Recently, lactate has emerged a crucial regulator of cancer development, regulation, and metastasis[71,72].

Chapter 3: Quantitative Measurement of Cancer Metabolism Using Stimulated Echo Hyperpolarized Carbon-13 MRS

The following chapter is adapted from: Swisher CL et al. "Quantitative measurement of cancer metabolism using stimulated echo hyperpolarized carbon-13 MRS" in Magnetic Resonance in Medicine, 2013.

Magnetic resonance spectroscopy of hyperpolarized substrates allows for the observation of label exchange catalyzed by enzymes; thereby providing a powerful tool to investigate tissue metabolism and potentially kinetics *in vivo*. However, the accuracy of current methods to calculate kinetic parameters has been limited by T_1 relaxation effects, extracellular signal contributions, and reduced precision at lower signal-to-noise ratio.

To address these challenges, we investigated a new modeling technique using metabolic activity decomposition-stimulated echo acquisition mode. The metabolic activity decomposition-stimulated echo acquisition mode technique separates exchanging from nonexchanging metabolites providing twice the information as conventional techniques. This allowed for accurate measurements of rates of conversion and of multiple T_1 values simultaneously using a single acquisition. The additional measurement of T_1 values for the reaction metabolites provides further biological information about the cellular environment of the metabolites. This new technique was investigated through simulations and in vivo studies of transgenic mouse models of cancer demonstrating improved assessments of kinetic rate constants and new T_1 relaxation value measurements for hyperpolarized ^{13}C-pyruvate, ^{13}C-lactate, and ^{13}C-alanine.

3.1 Background

3.1.1 Motivation

Hyperpolarized (HP) MRS is advantageous over conventional radionuclide imaging in that it detects not only the injected substrate, but also the products of its biochemical reactions providing additional biologically important information[21]. Prior to the introduction of HP MRS, noninvasive measures of flux through specific enzyme-catalyzed reactions have been limited by low SNR[73]. Measurement of these fluxes could profoundly aid in the understanding of physiology and clinical medicine. The 10,000 fold sensitivity enhancement gained by hyperpolarization of ^{13}C nuclei offers the possibility to non-invasively measure fluxes through individual enzyme-catalyzed reactions *in vivo* and in real-time[4,28,74].

3.1.2 Challenges in Kinetic Modeling with HP [1-^{13}C]-Pyruvate

Recently, time-resolved methods have been used to observe kinetics providing improved sensitivity to altered metabolism[74–82]. In *ex vivo* experiments, hyperpolarized ^{13}C substrates have been used to measure flux through single enzyme-catalyzed steps[73]. *In vivo*, however, the acquired signal is affected by flow, perfusion, diffusion, and membrane transport, in addition to metabolism[24,75,77]. To address these confounding factors, the stimulated echo acquisition mode (STEAM) approach included a diffusion preparation scheme, which can suppress signals from the vasculature and improve contrast for tissue metabolism[82,83].

Even with isolation of the signal to stationary tissue, robustly quantifying metabolism with kinetic parameters using HP MRS *in vivo* is difficult due to the lack of complexity of the dynamic curves and the number of free parameters that need to be estimated. This problem arises from spin-relaxation occurring concurrently with exchange, making it difficult to differentiate metabolic conversion from relaxation[78]. This allows for linear dependency between parameters, which can contribute to poor conditioning for least squares minimization (LSM), and ultimately leading to reduced accuracy in estimation of rates of conversion and spin-relaxation.

Furthermore, the precision and accuracy of the quantitative analysis deteriorate as the signal-to-noise ratio (SNR) decreases[84]. This is important even in the field of hyperpolarized MRS, in which spatial resolution and time constraints *in vivo* may lead to lower SNR. Recently, saturation or inversion magnetization transfer (MT)[78,79], has been applied to hyperpolarized carbon-13 MR to improve accuracy in the measurement of rates of conversion and observe real-time conversion. MT adds more linearly independent equations, requiring at least one extra excitation.

3.1.3 MAD-STEAM and Kinetic Modeling

Here, we applied a new modeling technique using Metabolic Activity Decomposition for reconstruction and a STEAM sequence for acquisition (MAD-STEAM). MAD-STEAM can be used to directly detect real-time conversion and separate exchanging from non-exchanging metabolites within a single acquisition[14]. The additional information from the MAD-STEAM experiment has the potential to improve the accuracy and precision of kinetic

measurements even with low SNR by adding more linearly independent equations. The goal of this study was to investigate this new approach in both simulations and *in vivo* animal studies with quantitative comparisons to prior methods.

The increased flux through the LDH enzyme resulting from the Warburg Effect is presumably responsible for the increased labeling of lactate observed in tumors, as compared to the normal surrounding tissue, following injection of hyperpolarized [1-^{13}C]-pyruvate[21,24,85]. Recently, it has been shown that there is a reduction in HP lactate detection in tumors responding to therapy[18,23,86]. It is widely accepted that these changes observed in lactate labeling are due to flux and exchange through the LDH enzyme[21]. To accurately quantify these changes in metabolism, a new modeling method was developed utilizing the extra information available with MAD-STEAM.

In addition to the high conversion to [1-^{13}C]-lactate observed in many tumors, increased [1-^{13}C]-alanine has been observed during tumor formation in a Myc-driven liver cancer model[22]. While it is well known that most cancers depend on a high rate of aerobic glycolysis for survival and proliferation. Additionally, some cancers display glutamine addiction, having high glutamine uptake into the cell despite the fact that glutamine can be produced from glucose[87]. The conversion of [1-^{13}C]-pyruvate to [1-^{13}C]-alanine via alanine transaminase (ALT) is affected by the availability of the glutamate cofactor, produced from conversion of glutamine via glutaminase inside the cell. Using the new information available with MAD-STEAM, we sought to investigate the rate of conversion of pyruvate-to-alanine for the first time during disease progression in a Myc-driven model, in which both the Warburg effect and glutamine addition have been reported[22,50].

This project was designed to increase specificity and accuracy in the measurement of spin-relaxation and multiple conversion pathways by applying MAD-STEAM to kinetic modeling and then evaluate the new information gained in transgenic models of cancer. A key benefit of measuring kinetics with the additional information from MAD-STEAM is that spin-relaxation and multiple rates of conversion can be measured simultaneously within a single acquisition. The additional parameters provided, such as the T_1 spin-relaxation for the reaction metabolites, may yield further information about the cellular environment experienced by the metabolites. This new technique is also desirable since it improves accuracy by reducing sensitivity to background noise and moving spins within the vasculature. In this study, we applied our new modeling technique to measure real-time metabolic conversion and T_1 spin-relaxation as kinetic markers of malignancy *in vivo* in transgenic mouse cancer models.

3.2 Theory

3.2.1 The MAD-STEAM Experiment

Recently Larson et al. showed that STEAM in the presence of metabolic conversion creates a phase shift that depends on the resonance frequency shift and echo time (TE), $\Delta\varphi = 2\pi\Delta f(TE/2)$ [19]. By choosing $\Delta\varphi = \pm\pi/2$, the metabolic conversion and exchange during a mixing time (TM) can be directly detected within a single acquisition[14]. The pulse sequence is shown in Figure 3.1. MAD-STEAM, which only uses a single acquisition, is advantageous for detecting hyperpolarized signals *in vivo* because magnetization cannot be renewed making it difficult to acquire multiple encoding steps. Ultrafast 2D NMR[88–90] could also be used to acquire similar information, however spatial inhomogeneity *in vivo* may

cause distortion of the data[14].

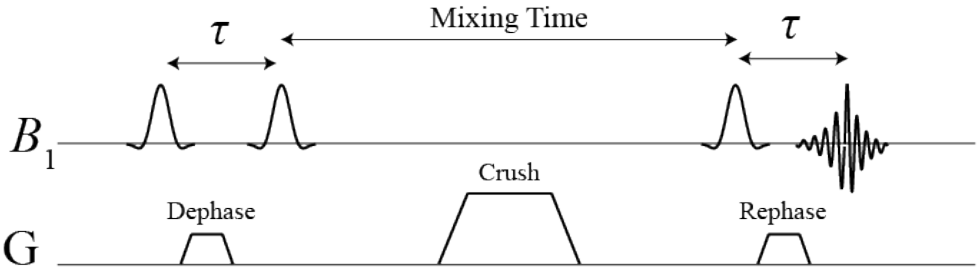

Figure 3.1: Metabolic activity decomposition with stimulated echo acquisition mode (MAD-STEAM) pulse sequence (τ =TE/2).

The MAD-STEAM experiment can be viewed as an extension of a 2D Exchange Spectroscopy (EXSY) NMR experiment[14,91]. The EXSY experiment also uses a stimulated-echo from three 90° pulses, in which the time between the first two 90° pulses, t_1, is incremented to sample a entire 2D spectrum[14]. Instead of acquiring multiple acquisitions of incremented t_1 durations, the MAD-STEAM experiment only samples $t_1 = TE/2$ such that the phase shift between the resonances of interest is $\pm\pi/2$ [14]. In other words, MAD-STEAM acquires the projection of a 2D EXSY spectrum, storing cross peak information in phase. The MAD-STEAM approach is similar to 1D EXSY experiment except that it stores cross peak information in phase rather than interpreting spectra after an inversion. A spin is "phase tagged" when there is an exchange reaction available and the acquired phase after exchange is $\Delta\varphi = \pm\pi/2$.

Here we used the "phase tagging" information encoded through the MAD-STEAM experiment to separate the total signal of a metabolite, $M_x(t)$, into the signal contributions from spins that have not gone through exchange, $Orig\{M_x(t)\}$, and spins that have gone through exchange, $New\{M_x(t)\}$, to improve kinetic measurements for the first time.

Recently Chen et al. and Larson et al. showed that a stimulated echo based MRS approaches could also be used to isolate signal in stationary tissue from spins within the vasculature, providing improved observation of active cellular metabolic conversion for hyperpolarized carbon-13 MR *in vivo*.

3.2.2 Kinetic Models

Previously, it has been shown that the lactate and pyruvate peak intensities can be fit to a simple two-site exchange model to give apparent rates of conversion[23,74,76,79],

$$\frac{d}{dt}\begin{bmatrix} |M_{Pyr}(t)| \\ |M_{Lac}(t)| \end{bmatrix} = \begin{bmatrix} -\rho_{Pyr} - K_{Pyr\to Lac} & +K_{Lac\to Pyr} \\ +K_{Pyr\to Lac} & -\rho_{Lac} - K_{Lac\to Pyr} \end{bmatrix} \begin{bmatrix} |M_{Pyr}(t)| \\ |M_{Lac}(t)| \end{bmatrix} \tag{3.1}$$

where M_{Pyr} and M_{Lac} denote the pyruvate and lactate peak integrals, t is time, ρ_{Pyr} and ρ_{Lac} are pyruvate and lactate spin-relaxation rates, $1/T_{1,x}$. $K_{Pyr\to Lac}$ and $K_{Lac\to Pyr}$ are the pyruvate and lactate apparent rates of conversion. Using MAD-STEAM the two-site exchange system can be described by the following equation:

$$\frac{d}{dt}\begin{bmatrix} Orig\{M_{Pyr}(t)\} \\ New\{M_{Pyr}(t)\} \\ Orig\{M_{Lac}(t)\} \\ New\{M_{Lac}(t)\} \end{bmatrix} = \begin{bmatrix} -\rho_{Pyr} - K_{Pyr\to Lac} & 0 & 0 & 0 \\ 0 & -\rho_{Pyr} & +K_{Lac\to Pyr} & 0 \\ 0 & 0 & -\rho_{Lac} - K_{Lac\to Pyr} & 0 \\ +K_{Pyr\to Lac} & 0 & 0 & -\rho_{Lac} \end{bmatrix} \begin{bmatrix} Orig\{M_{Pyr}(t)\} \\ New\{M_{Pyr}(t)\} \\ Orig\{M_{Lac}(t)\} \\ New\{M_{Lac}(t)\} \end{bmatrix}. \tag{3.2}$$

Where $Orig\{M_{Pyr}(t)\}$ and $Orig\{M_{Lac}(t)\}$ denote the pyruvate and lactate peak integrals with no phase shift $\Delta\varphi = 0$. $New\{M_{Pyr}(t)\}$ and $New\{M_{Lac}(t)\}$ denote the pyruvate and lactate peak integrals of z-magnetizations with phase shifts $\Delta\varphi = -\pi/2$ and $\Delta\varphi = +\pi/2$, respectively. The $\pm\pi/2$ phase shift will put the $Orig\{M_{Pyr}(t)\}$ and $Orig\{M_{Lac}(t)\}$ in the real

channel and the $New\{M_{Lac}(t)\}$ in the imaginary channel, such that they can easily be separated during reconstruction. For all models we assume that pyruvate and lactate are at steady state such that there is no significant influx into the slab. This is a valid assumption because the vascular component was suppressed by the STEAM sequence[83,92], and the acquisition was started after the arrival of pyruvate into the tissue.

This technique can be expanded to a three-site exchange system, such as the conversion of pyruvate to either lactate or alanine. Using the total signal from the peak areas for each metabolite, the following equations can be used to describe the system:

$$\frac{d}{dt}\begin{bmatrix} |M_{Pyr}(t)| \\ |M_{Lac}(t)| \\ |M_{Ala}(t)| \end{bmatrix} = \begin{bmatrix} -\rho_{Pyr} - K_{Pyr\to Lac} - K_{Pyr\to Ala} & 0 & 0 \\ +K_{Pyr\to Lac} & -\rho_{Lac} & 0 \\ +K_{Pyr\to Ala} & 0 & -\rho_{Ala} \end{bmatrix} \begin{bmatrix} |M_{Pyr}(t)| \\ |M_{Lac}(t)| \\ |M_{Ala}(t)| \end{bmatrix}. \quad (3.3)$$

Because pyruvate generated from lactate and pyruvate generated from alanine are in small amounts in the liver relative to the forward reactions, they were assumed to be negligible, and thus $New\{M_{Pyr}(t)\}$ is not part of the model. This constrains the number of free parameters to the number of linearly independent equations per time point to a 1:1 ratio. Using MAD-STEAM, the three-site exchange system can be described by the following system of equations:

$$\frac{d}{dt}\begin{bmatrix} Orig\{M_{Pyr}(t)\} \\ Orig\{M_{Lac}(t)\} \\ New\{M_{Lac}(t)\} \\ Orig\{M_{Ala}(t)\} \\ New\{M_{Ala}(t)\} \end{bmatrix} = \begin{bmatrix} -\rho_{Pyr} - K_{Pyr\to Lac} - K_{Pyr\to Ala} & 0 & 0 & 0 & 0 \\ 0 & -\rho_{Lac} & 0 & 0 & 0 \\ +K_{Pyr\to Lac} & 0 & -\rho_{Lac} & 0 & 0 \\ 0 & 0 & 0 & -\rho_{Ala} & 0 \\ +K_{Pyr\to Ala} & 0 & 0 & 0 & -\rho_{Ala} \end{bmatrix} \begin{bmatrix} Orig\{M_{Pyr}(t)\} \\ Orig\{M_{Lac}(t)\} \\ New\{M_{Lac}(t)\} \\ Orig\{M_{Ala}(t)\} \\ New\{M_{Ala}(t)\} \end{bmatrix} \quad (3.4).$$

The $Orig\{M_{Ala}(t)\}$ and $New\{M_{Ala}(t)\}$ were calculated based on the complex alanine peak

integral and separated using the phase shift, $\Delta\varphi_{Pyr\to Ala} = -\pi / 2.21$ at 3T and TE=14ms, using the equations below:

$$Orig\{M_{Ala}\} = \mathrm{Re}\{M_{Ala}\} + \frac{\mathrm{Im}\{M_{Ala}\}}{\tan(\Delta\varphi_{Pyr\to Ala})} \tag{3.5}$$

and

$$New\{M_{Ala}\} = -\frac{\mathrm{Im}\{M_{Ala}\}}{\sin(\Delta\varphi_{Pyr\to Ala})}. \tag{3.6}$$

3.2.3 Parameter Estimation

Common methods, such as Gauss-Newton algorithm (GNA), Levenberg-Marquardt algorithm (LMA), the Newton method and Generalized Gradient Descent, to estimate parameters from non-linear systems use the Jacobian Matrix, J, iteratively to linearize the least squares problem $Jx = b$, where x is the matrix of parameters to be solved and b is the data. When the condition number, $\kappa = \left(\frac{\left\|J^{-1}e\right\|}{\|e\|}\right)\cdot\left(\frac{\|b\|}{\left\|J^{-1}e\right\|}\right) = \|J\|\cdot\left\|J^{-1}\right\|$, is large ($e$ is error), even a small error in b (noise) may cause a large error in the solution, x. Thus, if the Jacobian becomes ill-conditioned, the least squares estimate amplifies the noise by a factor of κ, and results may be grossly inaccurate[93,94].

Linearization has been used to simplify calculations in exchange systems. Linearization could also be used along with MAD-STEAM to simplify calculations. In these comparisons, linearization was not used to avoid error in sum of squares minimization. Because the error on the linearized data is different than the error on the actual data, the linear least squares solution to linearized models minimizes the sum of squares of residuals for the nonlinear form of the dependent variables rather than the actual dependent variable.

The number of parameters a system can estimate reproducibly and accurately is related to the number of unique eigenvalues of the matrix K from the general equation, $\frac{dM(t)}{dt} = KM(t)$. The following matrix was obtained with using only the total peak area of the data (Eqn 3.1),

$$\begin{bmatrix} -\rho_{Pyr} - K_{Pyr\to Lac} & +K_{Lac\to Pyr} \\ +K_{Pyr\to Lac} & -\rho_{Lac} - K_{Lac\to Pyr} \end{bmatrix}. \tag{3.7}$$

This matrix has two distinct real eigenvalues for the following range of parameters: $K_{Pyr\to Lac} = 0.05 - 0.5 s^{-1}$, $K_{Pyr\to Lac} = 0.001 - 0.05 s^{-1}$, $T_{1,Pyr} = 10 - 50 s$, and $T_{1,Lac} = 10 - 50 s$. Meanwhile, the following matrix obtained from using Metabolic Activity Decomposition (Eq. 3.7) has four distinct real eigenvalues:

$$\begin{bmatrix} -\rho_{Pyr} - K_{Pyr\to Lac} & 0 & 0 & 0 \\ 0 & -\rho_{Pyr} & +K_{Lac\to Pyr} & 0 \\ 0 & 0 & -\rho_{Lac} - K_{Lac\to Pyr} & 0 \\ +K_{Pyr\to Lac} & 0 & 0 & -\rho_{Lac} \end{bmatrix}. \tag{3.8}$$

This matrix should be much more reliable for the prediction of more parameters because it has more unique eigenvalues.

3.3 Methods

3.3.1 Data Fitting

To solve the non-linear inverse problem, an iterative LMA was used in Matlab (The MathWorks Inc., Natick, MA), which interpolates between the method of gradient descent and the GNA. This algorithm uses a trust region such that a reasonable approximation is

always produced. Reasonable starting parameters, such as $T_{1,x} = 20s$, $K_{Pyr \to Lac} = 0.05s^{-1}$, and $K_{Lac \to Pyr} = 0.01s^{-1}$, were used to speed up computation and improve convergence. A single simulation and fit are shown in Figure 3.2. All dynamic curves were normalized to the total carbon during the experiment not including ^{13}C-Urea.

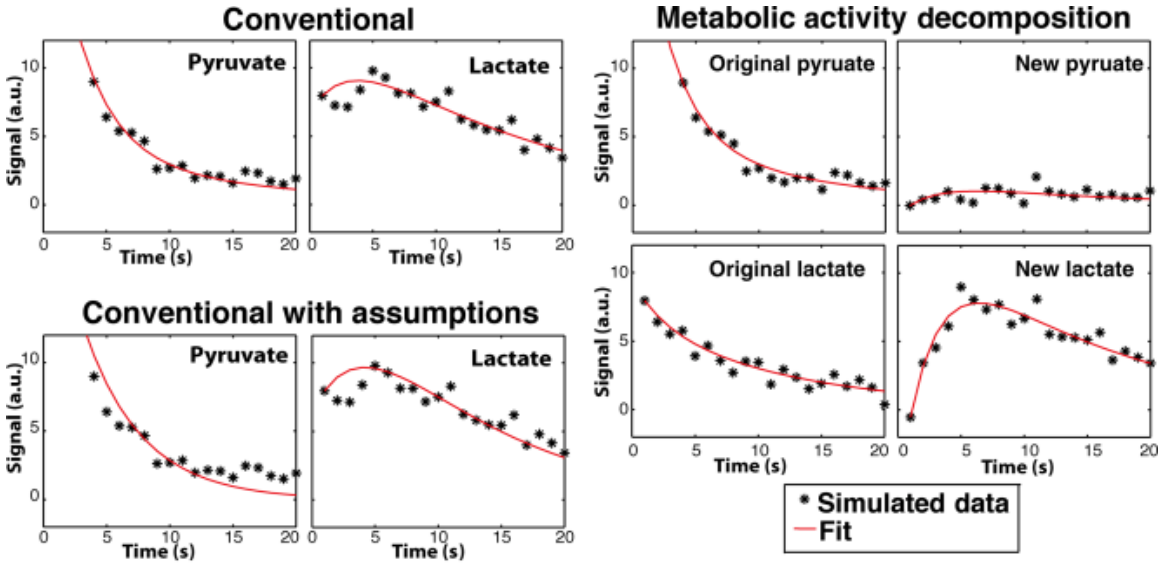

ACTUAL:	$T_{1,Pyr}$=15	$T_{1,Lac}$=11	$K_{Pyr \to Lac}$=0.2	$K_{Lac \to Pyr}$=0.05
Conventional:	$T_{1,Pyr}$=4.45	$T_{1,Lac}$=50.0	$K_{Pyr \to Lac}$=0.081	$K_{Lac \to Pyr}$=0.067
Magnitude with assumptions:		T_1=8.99	$K_{Pyr \to Lac}$=0.107	
Metabolic activity decomposition:	$T_{1,Pyr}$=13.6	$T_{1,Lac}$=12.6	$K_{Pyr \to Lac}$=0.227	$K_{Lac \to Pyr}$=0.073

Figure 3.2: Single simulation data and fitting results with metabolic activity decomposition and simple two-site exchange with and without assumptions. Two-site exchange with assumptions assumes that inline image and inline image.

3.3.2 Simulated Data

Data were simulated for a 20s experiment over a range of parameters: $K_{Pyr \to Lac} = 0.01 - 0.1s^{-1}$, $K_{Lac \to Pyr} = 0.002 - 0.02s^{-1}$, $K_{Pyr \to Ala} = 0.005 - 0.1s^{-1}$, $T_{1,Pyr} = 10 - 40s$, $T_{1,Pyr} = 10 - 40s$, and $T_{1,Ala} = 10 - 40s$. Each combination was simulated over a range of SNRs (25-250 with five iterations each). The SNR was determined using the average signal of pyruvate at the first time point and dividing by the noise root mean square (rms) for both

simulated data and *in vivo* data.

3.3.3 Hyperpolarization of [1-^{13}C]-Pyruvate and ^{13}C -Urea

[1-^{13}C]-Pyruvate mixed with the trityl radical OX063 (Tris[8-carboxyl-2,2,6,6tetra[2-(1hydroxyethyl)]-benzo(1,2-d:4,5-d)bis(1,3)dithiole-4-yl]methyl sodium salt, Oxford Instruments, Abingdon UK) and ^{13}C-urea mixed with the trityl radical OX063 were simultaneously hyperpolarized[95] for phase correction[14] using conventional dynamic nuclear polarization (DNP) methods and a HyperSense DNP polarizer (Oxford Instruments, Abingdon, UK) operating at 3.3T and a temperature of 1.3K. This yields more than 40,000 fold increases in the pyruvate and urea signals[4]. The sample was dissolved to produce solutions with 80mM pyruvate and 80mM urea and a biologically appropriate pH (~7.4) with TRIS/NaOH/EDTA dissolution media.

3.3.4 Acquisition and Reconstruction

All data were acquired with a STEAM sequence slab selection, TE = 14ms, TMs starting at 50ms, 20 acquisitions, 1s temporal resolution, 256 spectral points, 2.5 kHz spectral bandwidth, a progressive flip angle scheme, and an adiabatic double spin echo[96]. A symmetrically sampled full echo was acquired to preserve phase information. Co-polarized ^{13}C-urea was used as a phase reference to correct for phase shifts caused by homogeneous, bulk motion such as respiration, which would affect all metabolites[14].

For animal experiments, a 3T MRI system (GE Healthcare, Waukesha, WI, USA) was used with a dual-tuned mouse birdcage coil based on a design used previously[85,97]. Given the main field of 3T, the echo time TE=14ms was chosen. With TE=14ms, the phase of pyruvate

to lactate conversion will be $\Delta\varphi_{Pyr\rightarrow Lac} = +\pi/2$ such that the new and original lactate are in quadrature. Since new and original alanine are not exactly in quadrature, the magnitude was broken into its components (Eqn. 3.5 and 3.6) based on $\Delta\varphi_{Pyr\rightarrow Ala} = -\pi/2.21$ in order to separate original and new alanine. This information was used for modeling three-site exchange in the liver cancer model, in which there is known high alanine production.

3.3.5 Animal Experiments

All animal studies were performed under a protocol approved by the UCSF Institutional Animal Care and Utilization Committee. Mice were anesthetized with 1-1.5% isoflurane and placed on a pad heated to 37°C during the MR experiment. Transgenic prostate cancer (TRAMP) mouse models[85] (described in further detail in Chapter 4) at different stages of progression (n=5) and normal mice (n=5) were imaged for the two-site exchange study. Data were acquired from a slab containing predominately the tumor or from a 20mm slab of the abdomen for normal mice. In the reproducibility study, data were acquired from a slab containing the liver of a normal mouse. For the three-site exchange study, a switchable transgenic liver cancer model was used (n=5). Following a baseline scan and hyperpolarized ^{13}C study, doxycycline was removed from the diet to allow induction of expression of the human oncogenes Myc [51,98] or Myc and Ras transgenes[99] and initiation of tumorigenesis. Data were acquired from a slab containing the entire liver but excluding the lungs and abdomen. During each study, 350 μL of the hyperpolarized [1-^{13}C]-pyruvate solution was injected into the mouse over a 12s period, followed by a 0.15 mL normal saline flush. To reduce artifacts from the inflow of pyruvate, data acquisition began 25-30s following the start of injection of pyruvate. Axial, coronal, and sagittal T_2-weighted fast

spin-echo (FSE) images were acquired as anatomical references.

3.3.6 Enzyme Assays

LDH activity was measured in the transgenic liver cancer model (n=5) by observing the decrease in absorbance of reduced nicotinamide adenine dinucleotide (NADH) at 340 nm using a spectrophotometrical microplate reader (Saphire, Tecan, Maennesorf, Switzerland). Multiple samples from tumor and adjacent tissue were frozen in liquid nitrogen and homogenized in modified RIPA buffer (50 mM Tris-HCl pH 8.0, 150 mM NaCl, 0.5 % Na-deoxycholate, 1% Triton X 100, 0.1 % SDS, 2mM EDTA). Protein determination was performed using a BCA Protein Assay Kit (Pierce, Rockford, IL, USA). For determination of LDH activity, a standard curve was acquired using L-LDH from bovine heart (1000 units x mL^{-1} , Sigma-Aldrich, St. Louis, MO, USA). Activity was measured in the presence of 0.15 mM NADH (Sigma-Aldrich) and 0.8 mM pyruvate (Sigma-Aldrich) in 50 mM Tris-HCl, pH 7.4 for 5 min.

3.4 Results

3.4.1 Simulations

Conventional two-site exchange yields four unknowns but only two equations at each time point, causing unstable conditioning of the Jacobian matrix (Figure 3.3). When using conventional modeling, the condition number of the Jacobian matrix dramatically worsened when both the forward and backward rates are slow and the relaxation rates are similar, suggesting linear dependency between parameters. Intuitively, in these parameter ranges, conventional modeling is unable to distinguish forward from backward conversion and relaxation. Simulated data, shown in Figure 3.3 and Table 3.1, demonstrated that using

only the total peak areas for a two-site exchange and three-site exchange model results in a miscalculation of the rate of conversion and is less accurate in calculating multiple effective T_1s even when the model fits the data well (coefficients of correlation > 0.8). For these nonlinear systems, goodness of fit does not necessarily correlate with accuracy.

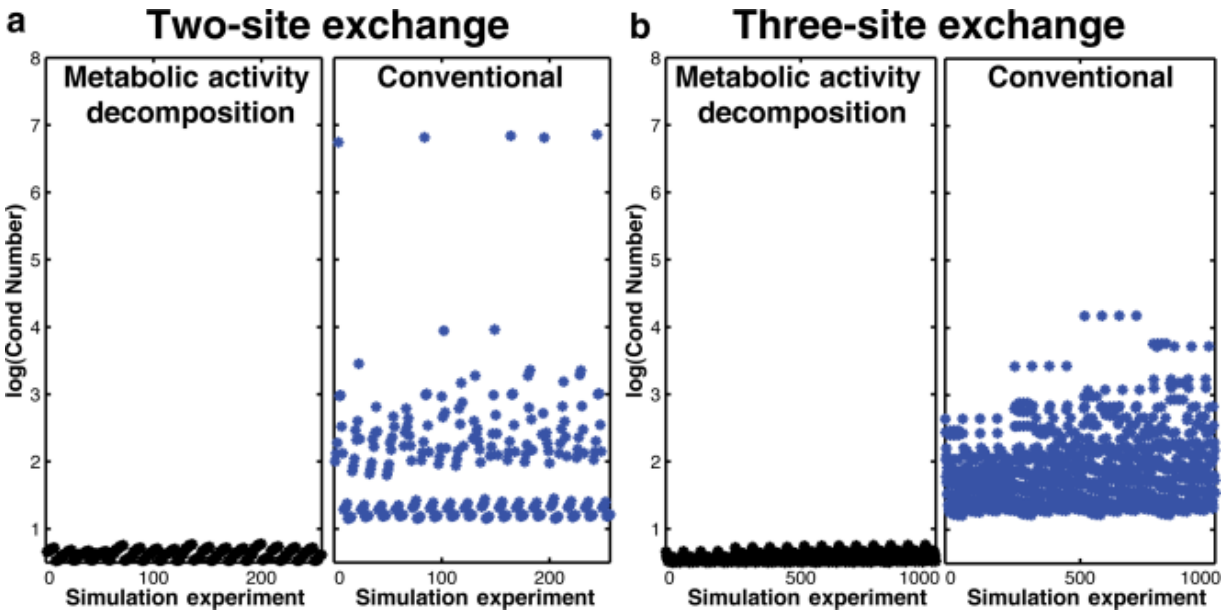

Figure 3.3: Comparison of stability and condition of (a) two-site exchange using the total metabolite signal and two-site exchange using metabolic activity decomposition and (b) three-site exchange using the total metabolite signal versus three-site exchange using metabolic activity decomposition. Comparison is over a wide range of parameters and all combinations in a physiological expected range. The condition number comes from Jacobian matrix at the solution, *x*.

Table 3.1: Accuracy in Estimated Kinetics Parameters obtained using Metabolic Activity Decomposition and other Approaches to Kinetic Modeling.

	Two-Site Exchange			Three-Site Exchange	
SNR = 25	***Metabolic Activity Decomposition***	***Conventional***	***Conventional with Assumptions*** [a]	***Metabolic Activity Decomposition***	***Conventional***
$\%Difference: K_{Pyr \to Lac}$	8.7%	338.6%	43.7%	2.9%	30.8%
$\%Difference: K_{Lac \to Pyr}$	21.9%	570.7%	-	-	-
$\%Difference: K_{Pyr \to Ala}$	-	-	-	8.1%	65.6%
$\%Difference: T_{1,Pyr}$	11.6%	31.7%	-	4.4%	25.7%
$\%Difference: T_{1,Lac}$	15.4%	36.%	-	3.1%	16.6%
$\%Difference: T_{1,Ala}$	-	-	-	4.6%	22.7%
SNR = 50					
$\%Difference: K_{Pyr \to Lac}$	5.0%	258.6%	44.3%	1.4%	19.0%
$\%Difference: K_{Lac \to Pyr}$	11.6%	351.2%	-	-	-
$\%Difference: K_{Pyr \to Ala}$	-	-	-	4.0%	41.1%
$\%Difference: T_{1,Pyr}$	7.3%	26.2%	-	2.4%	15.6%
$\%Difference: T_{1,Lac}$	8.6%	27.4%	-	1.5%	11.4%
$\%Difference: T_{1,Ala}$	-	-	-	2.3%	15.0%
SNR = 100					
$\%Difference: K_{Pyr \to Lac}$	2.7 %	113.2%	44.7 %	1.0%	13.2%
$\%Difference: K_{Lac \to Pyr}$	6.4 %	205.6%[d]	-	-	-
$\%Difference: K_{Pyr \to Ala}$	-	-	-	2.1%	25.9%
$\%Difference: T_{1,Pyr}$	4.5%	19.4%	-	1.1%	9.5%
$\%Difference: T_{1,Lac}$	5.3%	26.8%	-	0.7%	7.2%
$\%Difference: T_{1,Ala}$	-	-	-	1.2%	10.0%

[a]Assumes $T_{1,Pyr} = T_{1,Lac}$ and $K_{Lac \to Pyr} = 0$.

[b]Data is reported as average percent difference error between actual value and estimated value. Two-site exchange with Metabolic Activity Decomposition used Eq. 2 and conventional modeling used Eq. 1. Three-site exchange with Metabolic Activity Decomposition used Eq. 3 and conventional modeling used Eq. 4. The average percent difference, was found for n=5 simulation experiments per parameter combination, and SNR = 25-250 and without noise.

[c]Comparison was over a range of physiologically expected parameters and all combinations in that range: $K_{Pyr \to Lac} = 0.01 - 0.1 s^{-1}$, $K_{Lac \to Pyr} = 0.002 - 0.02 s^{-1}$, $K_{Pyr \to Ala} = 0.005 - 0.1 s^{-1}$, and $T_{1,x} = 10 - 40 s$.

[d] Even small errors in the back reaction may appear large when the denominator is small: *%Difference* = (|*Actual –Estimated*|)/*Actual*)* 100%

To improve the fit, the number of free parameters can be constrained by assuming $T_{1,Pyr} = T_{1,Lac}$ and $K_{Lac \to Pyr} = 0$ [23]. However, in the case of low SNR, this approach can often underestimate the conversion rate $K_{Pyr \to Lac}$ compensating with inaccurate relaxation rates which do not describe the actual kinetics of the system, as shown in Table 3.1. At SNRs values typically seen *in vivo*[14] using Metabolic Activity Decomposition, the precision of quantitative analysis is high as shown in Table 3.1. Even at very low SNRs, the error measured was less than 20%.

3.4.2 Two-Site Exchange In Vivo

Using Metabolic Activity Decomposition, higher production of lactate in the tumor was detected in the time series data, as shown in Figure 3.4. We observed high rates of conversion of pyruvate to lactate in a murine prostate tumor ($0.110 \pm 0.014 s^{-1}$) versus the abdomen of a normal mouse ($0.033 \pm 0.008 s^{-1}$). *In vivo*, calculations with MAD-STEAM yielded apparent $K_{Pyr \to Lac}$ values with a larger effect size compared to conventional modeling (Table 3.2). Decreased apparent $K_{Lac \to Pyr}$ rates of conversion were also observed in tumors suggesting an increased unlabeled lactate pool-size and a high availability of NADH. Not only were the rates of conversion different in tumor tissue, but also, the effective $T_{1,Lac}$ *s* were different in tumors as shown in Table 3.2.

Table 3.2. Comparison of Rates on Conversion in Tumors Versus in Normal with Metabolic Activity Decomposition and Conventional Two-Site Exchange.

$K_{Pyr \to Lac}$	***Tumor***	***Normal***	***P-value***
Metabolic Activity Decomposition:	0.110 ± 0.014	0.033 ± 0.008	0.005*
Conventional with Assumptions[b]:	0.068 ± 0.011	0.054 ± 0.008	0.385
Conventional:	0.150 ± 0.061	0.264 ± 0.069	0.164
$K_{Lac \to Pyr}$			
Metabolic Activity Decomposition:	0.001 ± 6.11x10^{-4}	0.025 ± 0.007	0.028*
Conventional:	0.153 ± 0.073	0.264 ±0.145	0.080
$T_{1,Pyr}$			
Metabolic Activity Decomposition:	0.120 ± 0.020	0.198 ± 0.035	0.123
Conventional:	0.197 ± 0.033	0.169 ± 0.020	0.271
$T_{1,Lac}$			
Metabolic Activity Decomposition:	0.105 ± 0.009	6.13x10^{-2} ± 0.007	0.026*
Conventional:	0.038 ± 0.009	5.26x10^{-2} ±0.027	0.500
$T_{1,Both}$			
Conventional with Assumptions[b]:	0.137 ± 0.011	0.170 ± 0.027	0.274

[a] Data is reported as the mean ± mse with units s^{-1}.

[b] Assumes $K_{Lac \to Pyr} = 0$ and $T_{1,Pyr} = T_{1,Lac}$

[c] Two-sided unpaired students t-test (n=5,α=0.05). *Denotes significant differences (p-value < α).

[d] Comparison of rates on conversion in tumor versus normal with Metabolic Activity Decomposition and conventional Two-site Exchange from slabs in the abdomen of TRAMP mice and normal mice. With this small sample size, significant differences were only detected when using Metabolic Activity Decomposition.

Multiple MAD-STEAM experiments were acquired in a single normal mouse liver using two-site exchange. This data showed reduced intrasubject variance in estimating $K_{Pyr \to Lac}$ using Metabolic Activity Decomposition (Mean = 0.079, σ = 0.012, Percent Error = 16.7%) versus using the magnitude of the spectra (Mean = 0.077, σ = 0.039, Percent Error = 50.2%) or the magnitude of the spectra with assumptions (Mean = 0.051, σ = 0.024, Percent Error = 46.9%). Large percent errors in parameter estimation in the three modeling techniques were attributed to the low SNR of lactate in normal tissue. Even with the lower SNR, Metabolic Activity Decomposition demonstrated improved reproducibility.

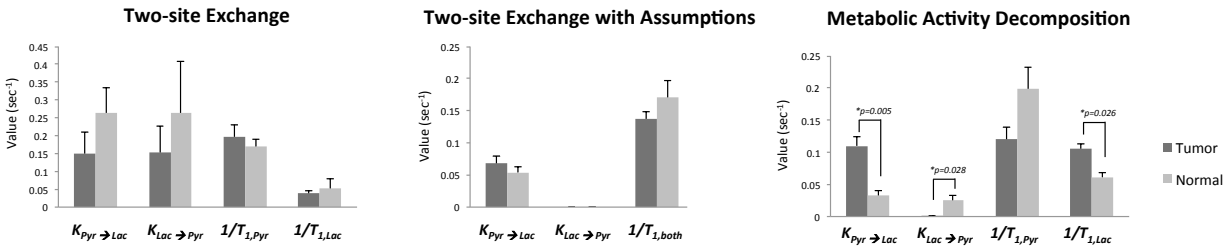

Figure 3.4: Comparison of Rates on Conversion in Tumors Versus in Normal with Metabolic Activity Decomposition and Conventional Two-Site Exchange with and without the assumptions that there is no conversion of lactate-to-pyruvate and the T_1 for lactate and pyruvate are equal.

3.4.3 Three-Site Exchange In Vivo

Representative data from a MAD-STEAM experiment and three-site exchange using Metabolic Activity Decomposition are shown in Table 3.2. Using Metabolic Activity Decomposition, real-time alanine conversion can be detected as seen in Figure 3.6D and 3.6F. Using Metabolic Activity Decomposition, changes in the rate of conversion of [1-^{13}C]-pyruvate to [1-^{13}C]-alanine were observed in addition to conversion to [1-^{13}C]-lactate as shown in Figure 3.7. In this mouse model experiment, a three fold increase in $K_{Pyr\rightarrow Ala}$ was observed following oncogene expression in the pre-tumor state compared to baseline and a further three fold increase was detected when the tumor was at a late stage (baseline = 0.046, pre-tumor = 0.131, late tumor = 0.398). There was a 37.3% decrease in the effective $T_{1,Ala}$ from baseline to the pre-tumor state and a 26.8% increase in the effective $T_{1,Ala}$ from the pre-tumor to late state as shown in Figure 3.7. Additionally, there was a 17.3% decrease in the $T_{1,Lac}$ from baseline to the pre-tumor stage.

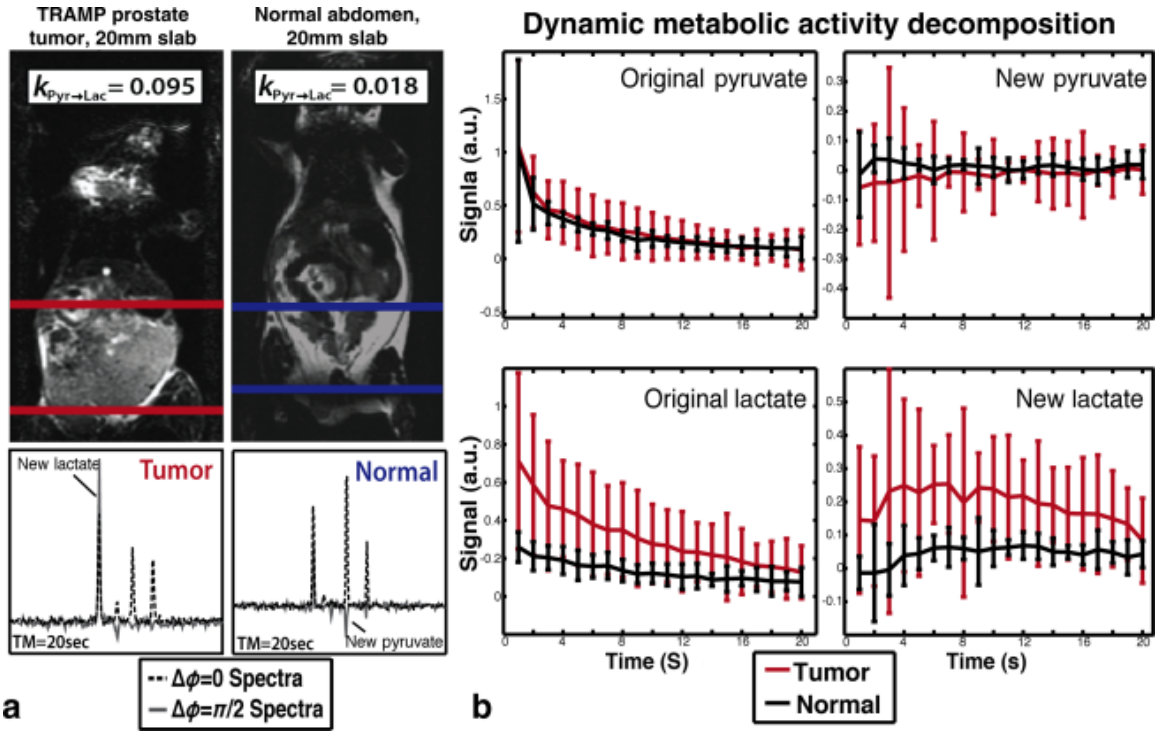

Figure 3.5: (a) Sample spectra from tumor and normal regions and their corresponding slab locations. **(b)** Dynamic curves from metabolic activity decomposition showing increased conversion of lactate to pyruvate and faster decay of the original lactate signal in TRAMP tumors versus normal tissue. Data was normalized to total carbon, excluding ^{13}C-urea (n=5).

As supporting data, $K_{Pyr\rightarrow Lac}$ measurements were compared to enzymatic assays. $K_{Pyr\rightarrow Lac}$ measured with Metabolic Activity Decomposition (R^2 = 0.809) demonstrated a higher correlation with LDH activity than modeling with the total signal of each metabolite (R^2 = 0.343). $K_{Pyr\rightarrow Lac}$ measured with Metabolic Activity Decomposition also had a higher correlation to LDH activity assays than metabolite ratios such as the lactate-to-total carbon ratio (R^2 = 0.530) excluding ^{13}C -urea and the lactate-to-pyruvate ratio (R^2 = 0.662) over the entire dynamic experiment and the lactate-to-pyruvate (R^2 = 0.687) after perfusion of the pyruvate bolus (t=3s after start of acquisition, acquisition started at 30 seconds after start of pyruvate injection).

3.5. Discussion & Conclusions

Metabolic Activity Decomposition kinetic modeling of hyperpolarized MR data demonstrated improved precision in estimation of both rates of conversion and relaxation rates (Table 3.1). This improvement is attributed to additional information from the Metabolic Activity Decomposition method, which provides a well-conditioned system and reduces sensitivity to linear dependency from Metabolic Activity Decomposition method, which provides a well-conditioned system and reduces sensitivity to linear dependency from similar parameters (Figure 3.3). There is some bias in the data for all methods presented due to fitting to the data magnitude. The magnitude was used for fitting *in vivo* data because it is commonly used in the literature[77,79], and a main goal of this work was to compare to previous approaches. This bias could be removed by using complex data instead of using the magnitude.

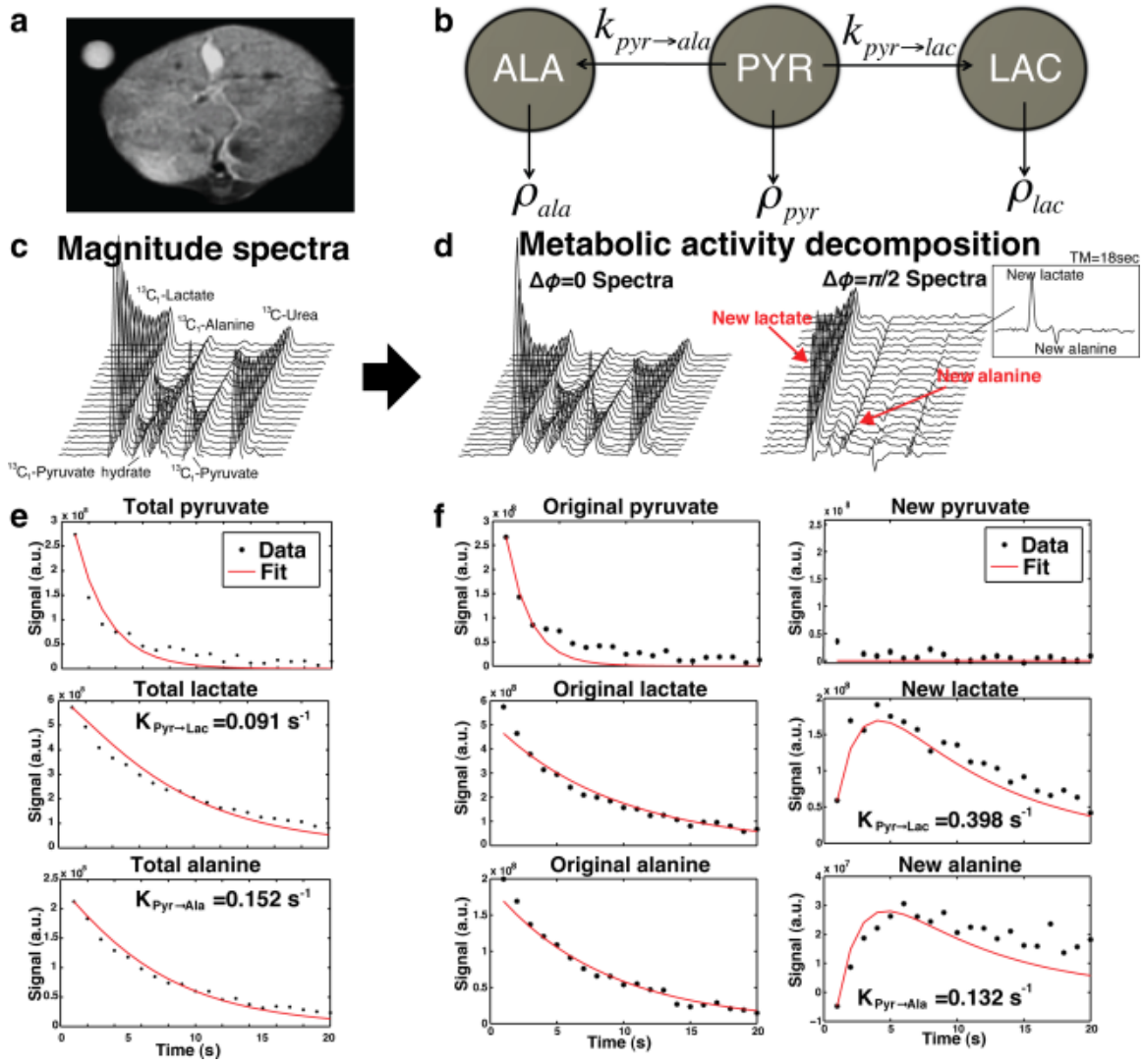

Figure 3.6: (a) T_2-weighted axial anatomical image within the slab where data was acquired. **(b)** Schematic of the three-site exchange system. Stacked plots of the successively acquired **(c)** magnitude spectra, **(d)** real ($\Delta\varphi$=0) and imaginary ($\Delta\varphi$=π/2) spectra from a MAD-STEAM pulse sequence with TE=14 ms. The areas under the curve from **(e)** the magnitude spectra with the corresponding three-site exchange fit Eq. using only the total amount of each metabolite and **(f)** the areas under the curve from the real and imaginary spectra with the corresponding three-site exchange fit to Eq. using original and new metabolite information provided by metabolic activity decomposition.

Simulations over a wide range of relaxation and conversion rates demonstrated that this new modeling technique not only more accurately calculated these parameters, but it also was robust to noise with SNRs down to 10:1. Even though all models showed high goodness of fit, a good fit did not necessarily correlate with accurate estimates, suggesting that caution should be taken when evaluating the accuracy of these nonlinear models

based on goodness of fit alone[100].

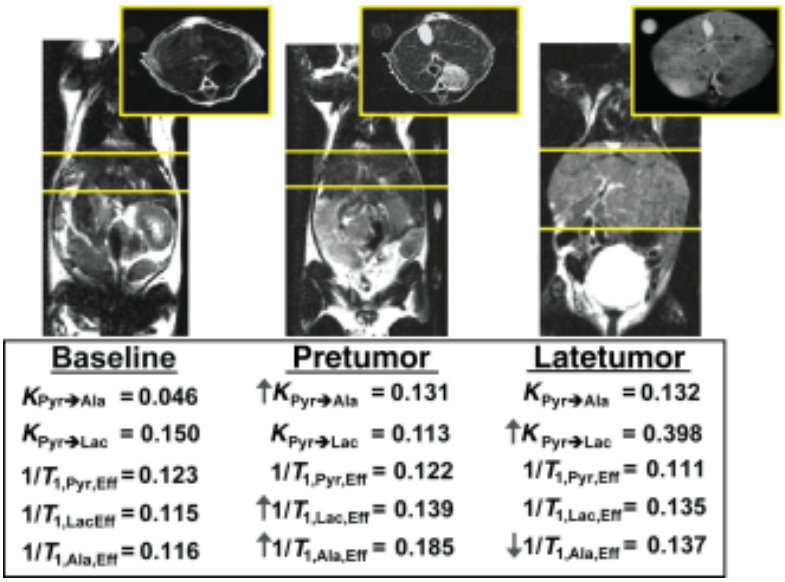

Figure 3.7: T_2-weighted axial and coronal anatomical images showing progression in a switchable oncogene driven model of liver cancer and the corresponding rates of conversion calculated from three-site exchange using MAD-STEAM and Eq. at each time point: baseline, 2 weeks (pretumor), and five weeks (late tumor) off doxycycline. Yellow lines contain the liver where data was acquired.

Even with the inherent 50% loss in SNR using a STEAM sequence compared to some other acquisition strategies[83], the accuracy gained from new "phase tagging" information with Metabolic Activity Decomposition far overcame any loss of accuracy from decreased SNR. For instance, at an SNR=100 the average error in estimation of $K_{Pyr\to Lac}$ for the two-site exchange was 113.0% with conventional modeling, but only 2.7% using Metabolic Activity Decomposition both with simulated data. Using only the conventional modeling, accuracy was improved to 44.7% error by assuming $K_{Lac\to Pyr}=0$ and $T_{1,Pyr}=T_{1,Lac}$. Even at a 50% lower SNR (SNR=50) using Metabolic Activity Decomposition, the average error was far less than all conventional approaches, 5.0%, as shown in Table 3.1. Similarly, the average error in estimation of $K_{Pyr\to Lac}$ for three-site exchange model was 13.21% at an SNR=100 using conventional modeling, but only 1.4% at an SNR=50 using Metabolic Activity

Decomposition. Also, alternate preparation schemes have been shown improve SNR for the stimulated echo acquisition[83] and thus could substantially reduce such losses for MADSTEAM experiments as well.

In a comparison of tumor versus normal, using Metabolic Activity Decomposition to solve for rates of conversion and relaxation times had a larger effect size in both conversion and relaxation rates, allowing the new method to better distinguish changes in metabolism and cellular environment. In tumors, the measured $K_{Pyr\rightarrow Lac}$ values were significantly higher than normal, which agrees with prior findings that cancerous tissues have higher LDH-A expression[101]. Interestingly, effective $T_{1,Lac}$ was shorter in tumors compared to normal tissues suggesting an altered cellular environment for lactate in the tumors. Because the b-value increases during the experiment, the effective T_1s measured in these experiments are a combination of both diffusion weighting as well as the longitudinal relaxation.

Improved reproducibility was also observed. The $K_{Pyr\rightarrow Lac}$ measured using Metabolic Activity Decomposition had an improved correlation with the measured enzyme activity compared to conventional modeling. This suggests that the new technique more accurately reflected enzymatic activity. Even with isolation of the detected signal to stationary tissue and "phase tagging," other factors such as membrane transport were not accounted for in this model. Prior studies have isolated intracellular and extracellular metabolites and have shown that membrane transport can play a role in the measured rate of conversion[69,76]. The combination of this work with these methods would provide even further specificity for enzyme activity. Another future direction is the minimization of the voxel volume, which would allow for improved localization of tissue areas and could enable the study of

smaller tumors and smaller regions of normal tissues.

When the modeling technique was used in a liver cancer model known to have high pyruvate conversion to alanine in the pre-tumor stage[22], the two-site exchange model is no longer valid. Here, the conversion rate of [1-^{13}C]-pyruvate to [1-^{13}C]-alanine was investigated for the first time during tumor formation. Because the phase shift of [1-^{13}C]-pyruvate to [1-^{13}C]-alanine with a 14ms echo time at 3T is approximately $-\pi/2$, Metabolic Activity Decomposition could be used to model the three-site exchange system to obtain improved measurements of $K_{Pyr\rightarrow Ala}$. In a transgenic oncogene-driven liver cancer model, changes in $K_{Pyr\rightarrow Ala}$ were observed between baseline, two weeks (pre-tumor), and two months (late tumor) off doxycycline in addition to changes in $K_{Pyr\rightarrow Lac}$ during progression, as shown in Figure 3.7.

This technique improved accuracy, simultaneously measured conversion rates and effective T_1s, and suppressed vascular effects, thus providing new quantitative measures of relaxation and conversion rates. The ability to quantify rates of conversion with increased accuracy can improve current hyperpolarized kinetic models and could aid in the understanding of metabolic alterations in diseases including cancer. Meanwhile the T_1 relaxation measurements obtained in this approach provide additional parameters for the investigating the effects of the intracellular environment on the metabolites of interest.

In vivo, the increased accuracy resulted in a larger effect size between tumors and normal tissue. $K_{Pyr\rightarrow Lac}$ increased in tumors, the back reaction $K_{Lac\rightarrow Pyr}$ decreased, and $T_{1,Lac}$ was

shorter in tumors suggesting an altered cellular environment in the tumors. Moreover, the ability to detect changes between different stages of progression suggests that $K_{Pyr \rightarrow Ala}$ may also be valuable in addition to $K_{Pyr \rightarrow Lac}$ in investigating metabolism alterations with disease, particularly in case of liver cancer. Since it provided better measures of tumor kinetic parameters, this new acquisition and modeling technique demonstrated biomedical potential for monitoring cancer progression and response to therapy.

Chapter 4. Localized, Non-invasive *In Vivo* Measurement of Enzymatic Activity

The following chapter is adapted from: Swisher CL et al. "Localized, Non-invasive *In Vivo* Measurement of Enzymatic Activity using MAD-STEAM Hyperpolarized Carbon-13 MR Spectroscopic Imaging" which is in revision for Magnetic Resonance in Medicine, 2014.

Traditionally, measurements of enzymatic activity require invasive biopsy, and inaccuracies can occur since the tissue is frozen, lysed, and cannot account for cellular membrane transport. Recently, we showed that using MAD-STEAM single-voxel acquisition and reconstruction with hyperpolarized carbon-13 magnetic resonance spectroscopy, real-time conversion can be directly observed, which suggested increased specificity for monitoring intracellular enzymatic activity. Extending the method to Magnetic Resonance Spectroscopic Imaging (MRSI) provides improved localization of those changes, which can better differentiate tumor versus normal and was necessary to verify that MAD-STEAM is, in fact, measuring intracellular enzymatic activity. In transgenic models of cancer, real-time generation of lactate was observed in a prostate tumor model, which was used to construct parametric maps.

MAD-STEAM MRSI was developed to provide a simple and robust method for parametric mapping with increased specificity to cellular exchange without concomitant signals from arterial input or T_1 longitudinal relaxation. We found that the results using this technique were significantly correlated with enzymatic activity (Spearman: $\rho = 0.943$ and *p-value* = 0.017) and can be used to non-invasively measure enzymatic activity *in vivo* and identify aggressive

regions with high LDH enzymatic activity (*p-value* = 0.003). Kinetics maps revealed variations within the tumor that were not visible with T_2W anatomic imaging and secondary metastatic regions. In the field of oncology in particular, this new technique has great biomedical and clinical significance, as it could be used to better identify particularly aggressive regions within tumors, monitor cancer progression, and follow response to therapy.

4.1 Background

4.1.1 Warburg Effect and Lactate Dehydrogenase

Tumor cells have an altered metabolic phenotype characterized by increased glycolytic flux and high cellular lactate production catalyzed by the lactate dehydrogenase (LDH) enzyme[26,32,102]. LDH catalyzes the interconversion of pyruvate and lactate with concomitant interconversion of NADH and NAD^+. In most normally differentiated cells, the LDH enzyme converts pyruvate, the final product of glycolysis, to lactate only in hypoxia conditions and thereby relies on mitochondrial oxidative phosphorylation to produce ATP. In contrast, many cancer cells rely on aerobic glycolysis called the Warburg effect, whereby they have adapted to derive ATP from metabolism of glucose to lactate in the cytosol, even in the presence of oxygen. At high concentrations of lactate, the LDH enzyme exhibits feedback inhibition, and the rate of conversion of pyruvate to lactate is decreased. However, many cancerous cells secrete lactate rapidly out of the cell via monocarboxylate transporters such as MCT4[68,103], thus limiting feedback inhibition.

LDHA (lactate dehydrogenase A) overexpression is inducible in hypoxic conditions[104], and in many cancers. High LDHA levels have been linked to a poorer prognosis in many cancers[55,56]. Moreover, high concentrations of lactic acid produced from flux through the LDH enzyme is a

hallmark of cancer metabolism[32]. While expression can report that the protein is in fact expressed, it does not report on actual enzyme functionality i.e. correct folding of the enzyme, presence of required cofactors, proper targeting, protein transport, and if there are mutations crucial to catalytic residues; whereas measurements of enzymatic activity account for all of these factors. As such, measurement of enzymatic activity should provide a more accurate description of aberrant cancer metabolism and increased sensitivity to abnormal tissue. Conventional measurements of enzymatic activity require invasive biopsy. Here we developed a non-invasive localized tool to measure enzymatic activity with hyperpolarized ^{13}C magnetic resonance spectroscopic imaging (MRSI).

4.1.2 Motivation

In medical imaging, there is a growing need to better detect and characterize abnormal tissue and disease processes. However, since most imaging techniques rely on physical parameters to generate image contrast, specific molecular information such as protein expression or enzymatic activity cannot often be obtained or is of limited value. Recently, it has been shown that the Metabolic Activity Decomposition technique provided more accurate quantitative measures of conversion rates[15] for hyperpolarized (HP) ^{13}C[15]MR by removing confounding signals from the vasculature[83], allowing for direct observation of real-time exchange and flux[14], and measuring T_1 relaxation times simultaneously[15]. Using Metabolic Activity Decomposition with Stimulated Echo Acquisition Mode (MAD-STEAM) single-voxel acquisition and reconstruction, real-time conversion and exchange were directly observed. In this project, we developed a MAD-STEAM spectroscopic imaging sequence to obtain spatially localized parametric maps of exchange kinetics in preclinical cancer models and to correlate these data with subsequent *ex vivo* biochemical enzymatic activity assays of resected tissue samples.

4.2 Materials and Methods

4.2.1 MAD-STEAM Acquisition and Reconstruction

As shown by Larson et al., Stimulated Echo Acquisition Mode (STEAM) in the presence of metabolic conversion creates a phase shift dependent on the resonance frequency and the echo time ($TE/2$), $\Delta\varphi = 2\pi f \frac{TE}{2}$, which can be used to "phase tag" metabolites ($\Delta\varphi \approx \pm\pi/2$) and directly observe real-time metabolism. Using metabolic activity decomposition (MAD), exchanging versus non-exchanging spins can then separated based on their "phase tag."[14,15] For a main field of 3T, the echo time TE=14ms was chosen such that the phase of pyruvate to lactate conversion will be $\Delta\varphi_{Pyr\rightarrow Lac} = \pi/2$ and the generated and original lactate (Denoted as $Lac_{from\ Pyr}$ and $Lac_{no\ change}$, respectively) are in quadrature, shown in Figure 4.2a.

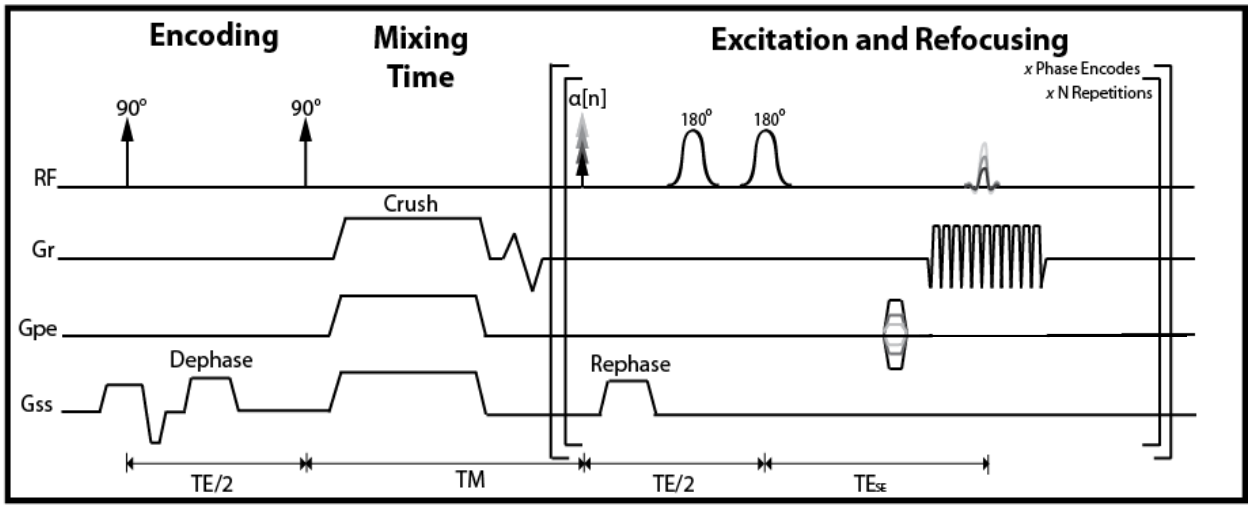

Figure 4.1: Dynamic Metabolic Activity Decomposition with Stimulated Echo Acquisition Mode (MAD-STEAM) pulse sequence with flyback echo planar spectroscopic imaging (EPSI). All data were acquired with 20mm slab selection in z, 59 spectral points, two repetitions, a progressive flip angle scheme, and adiabatic double spin echo[20]. A symmetrically sampled full echo was acquired to preserve phase information [19].

Co-polarization with ^{13}C-urea provided a phase reference to correct for phase shifts caused by homogeneous, bulk motion such as respiration, which would affect all metabolites[14]. Two

adiabatic double spin echoes were used to extend the echo time, reduce sensitivity to phase errors, and improve spectral quality[96]. Flyback Echo Planar Spectroscopic Imaging was added to the MAD-STEAM pulse sequence, shown in Figure 4.1, to localize and image enzymatic conversions of hyperpolarized pyruvate throughout the tumor and normal tissues.

4.2.2 Kinetics Maps of Metabolism

Data from MAD-STEAM can be used to describe the following system,

$$\begin{array}{ccc} Pyr & \xrightarrow{K_{Pyr\rightarrow Lac}} & Lac \\ T_1 \downarrow & & \downarrow T_1 \end{array}$$

where $K_{Pyr\rightarrow Lac}$ is the net flux of pyruvate to lactate during a mixing time and T_1 is the longitudinal relaxation of both metabolites[13]. We also assume that the backwards reactions, to pyruvate and $K_{Pyr\rightarrow Ala}$ outside of the liver are negligible compared to the conversion of pyruvate to lactate, $K_{Pyr\rightarrow Lac}$.

Because of the additional information provided by MAD-STEAM, parametric maps can be prepared from only two images with the following simple, algebraic equations traditionally used in exchange spectroscopy (EXSY)[91]:

$$1/T_1 = \frac{1}{TM}\log\left(\frac{Lac(0)^2 - Pyr(0)^2}{Lac_{no\ change} - Pyr_{no\ change}}\right) \quad (4.1)$$

$$K_{Pyr\rightarrow Lac} = \frac{1}{TM}\log\left(1 - \frac{Lac_{from\ Pyr} * \exp\left(TM/T_1\right)}{Lac_{no\ change} * Pyr_{no\ change}}\right) \quad (4.2)$$

where TM is the mixing time between the first and second acquisition. $Lac(0)$ and $Pyr(0)$ are the initial images of lactate and pyruvate acquired from the first image and $Lac_{from\ Pyr}$,

$Pyr_{from\ Lac}$, $Lac_{no\ change}$, and $Pyr_{no\ change}$ (Figure 4.2b) are acquired from the second image using MAD.

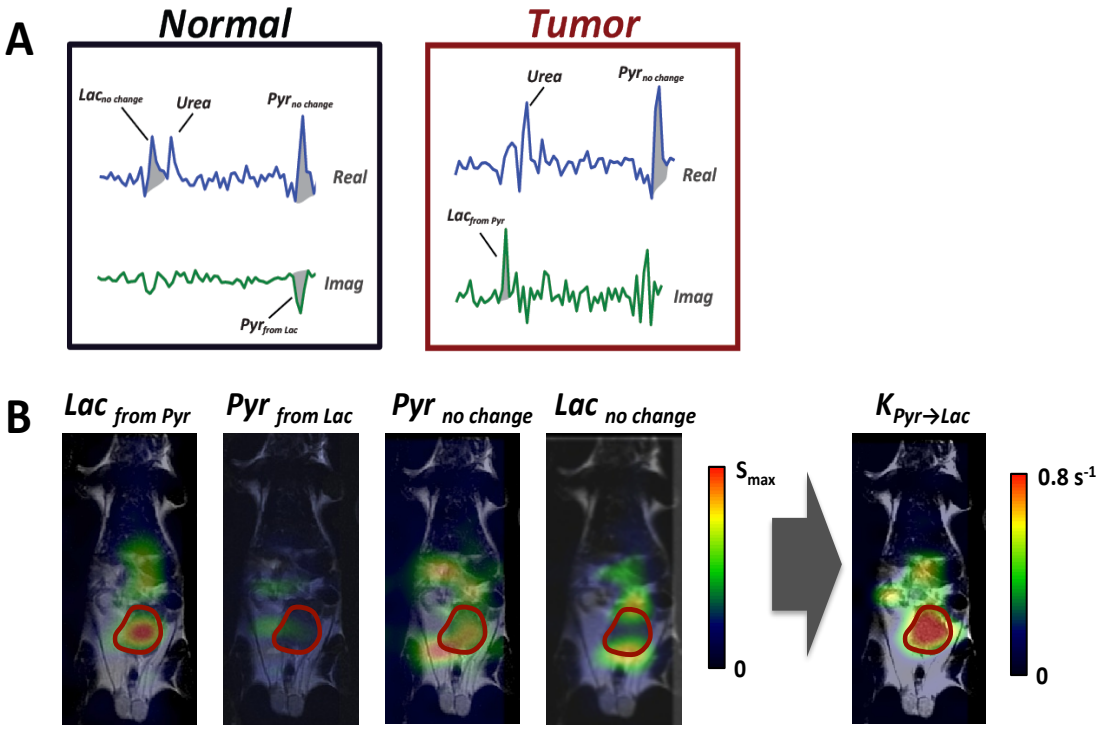

Figure 4.2: **(a)** Reconstruction of real and imaginary spectra into **(b)** metabolite maps, which were used to prepare kinetic parametric maps with Eq 1 and Eq 2 from two coronal MRSI of images using MAD-STEAM in a transgenic model of prostate cancer (reps = 2, Δz = 20mm, TE=14ms).

4.2.3 Animal Experiments

For animal experiments, a 3T clinical MRI system (GE, Waukesha, WI, USA) was used with a dual-tuned mouse birdcage coil based on a design used previously[85,97]. All animal studies were performed under a protocol approved by the UCSF Institutional Animal Care and Utilization Committee. Mice were anesthetized with 1-1.5% isoflurane and placed on a pad heated to 37°C during the MR experiment. During each study, 350μL of the hyperpolarized [1-^{13}C]-pyruvate and ^{13}C-Urea solution was injected into the mouse over a 12s period. To allow perfusion of pyruvate into the tissue, data acquisition began 20 sec following the start of injection of pyruvate. Axial and coronal T_2-weighted fast spin-echo (FSE) images were acquired as anatomical references.

A Transgenic Adenocarcinoma of the Mouse Prostate (TRAMP) was used for this study. TRAMP mice will develop progressive forms of prostate cancer with distant site metastasis and exhibit various forms of disease from mild intraepithelial hyperplasia to large multinodular malignant neoplasia. Activation of probastin at maturation, allows for the expression of the SV40 T antigen initiating tumor formation as shown in Figure 4.3.

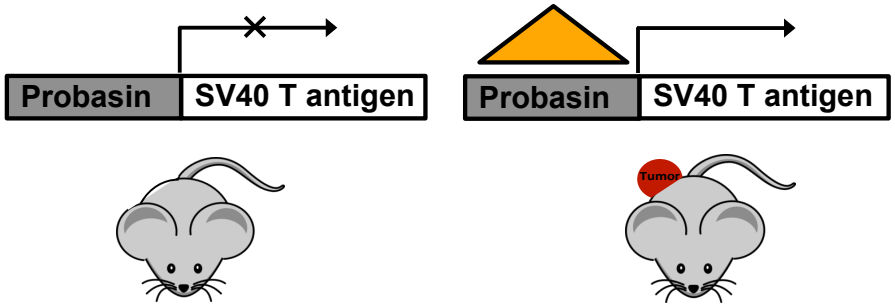

Figure 4.3: Schematic of transgenic adenocarcinoma of the mouse prostate (TRAMP) mechanism for tumor initiation where activation of probastin occurs at maturation, allowing for the expression of the SV40 T antigen initiating tumor formation.

4.2.4 Polarization of [1-^{13}C] Pyruvate and ^{13}C-Urea

[1-^{13}C]-Pyruvate mixed with the trityl radical OX063 (Tris[8-carboxyl-2,2,6,6tetra[2-(1hydroxyethyl)]-benzo(1,2-d:4,5-d)bis(1,3)dithiole-4-yl]methyl sodium salt, Oxford Instruments, Abingdon, UK) and ^{13}C-urea mixed with the trityl radical OX063 were hyperpolarized[95] using conventional DNP methods and a HyperSense DNP polarizer (Oxford Instruments, Abingdon, UK) operating at 3.3T and a temperature of 1.3K. All samples were dissolved to produce solutions with 80mM pyruvate and 80mM urea and a biologically appropriate pH (~7.4) with TRIS/NaOH/EDTA dissolution media.

4.2.5 Enzymatic Assays

LDH activity was measured through an NADH-linked spectrophotometric method by observing the decrease in absorbance of NADH at 339nm after addition of varying

concentrations of pyruvate. Approximately 7.5mg of frozen tissue was thawed in lysis buffer (830μL) containing 50mM Tris (pH 8.2), 2mM DTT, 2mM EDTA, and 1% Triton x-100. The tissue was homogenized for 30 sec and centrifuged for 5 min at 7000rpm at 4°C. The supernatant was removed and diluted appropriately so that the reduction of NADH was linear over the first 10 min of the assay. In microplate wells, 3ml of cell lysate was mixed with 147ml reaction buffer containing varying concentrations of pyruvate, 80mM Tris (pH 7.2), 200mM NaCl, and 200mM NADH, which was heated to 30°C.

The assay was conducted immediately by monitoring the decrease in NADH absorbance, at 339nm, for 10 min with an Infinite M200 spectrophotometer (Tecan) Each pyruvate concentration was assayed in triplicate. The reaction rate was normalized to total protein concentration (Quick Start Bradford Protein Assay, Bio-Rad). Each sample was assayed in triplicates, at 595nm, after incubating at room temperature for at least 5 min. The absorbance of the sample was then recorded, and protein concentration was calculated with a gamma-globulin standard curve. Once the sample's protein concentration had been acquired, it was used to calculate LDH reaction rates for the varying pyruvate concentrations. The LDH reaction rate, measured in mM NADH/min/[protein], was plotted against pyruvate concentrations according to Michaelis-Menten kinetics. The maximum velocity (V_{max}) and substrate concentration at which the reaction rate is half of the maximum (K_m) values were then calculated with the Lineweaver-Burk plot.

4.2.6 Protein Expression

PCR was conducted in triplicate with 20 mL reaction volumes of 1X Taqman buffer (1X Applied Biosystems PCR buffer, 20% glycerol, 2.5% gelatin, 60nM Rox as a passive

reference), 5.5 mM $MgCl_2$, 0.5 mM each primer, 0.2 mM each deoxynucleotide triphosphate (dNTP), 200 nM probe, and 0.025 unit/mL AmpliTaq Gold (Applied Biosystems) with 5 ng cDNA. A large master mix of the above-mentioned components (minus the primers, probe, and cDNA) was made for each experiment and aliquoted into individual tubes, one for each cDNA sample. cDNA was then added to the aliquoted master mix. The master mix with cDNA was aliquoted into a 384-well plate. The primers and probes were mixed together and added to the master mix and cDNA in the 384-well plate. PCR was conducted on the ABI 7900HT (Applied Biosystems) using the following cycle parameters: 1 cycle of 95° for 10 minutes and 40 cycles of 95° for 15 seconds, 60° for 1 minute. Analysis was carried out using the SDS software (version 2.3) supplied with the ABI 7900HT to determine the Ct values of each reaction.

Ct values were determined for three test and three reference reactions in each sample, averaged, and subtracted to obtain the ΔCt [ΔCt = Ct (test locus) – Ct (control locus)]. PCR efficiencies were measured for all custom assays and were greater than or equal to 90%. Therefore, relative fold difference was calculated for each primer/probe combination as $2^{-\Delta Ct}$ x 100. L19 (Applied Biosystems) was used as the control.

4.2.7 Statistical Analysis

The Spearman correlation coefficient was used to assess the linear correlation between LDH activity and $K_{Pyr \rightarrow Lac}$ along with linear regression and goodness of fit. High-grade tumors (>60% poorly differentiated cells) were compared to normal adjacent tissue with a two-sided student's t-test being used to test for statistical significance. The effect size was calculated using Cohen's D.

The *a priori* minimum sample size was calculated to be 9 using Mead's Resource Equation (E = N – B – T), where the blocking component B = -1, the treatment component T = 0, and N is total number of units minus one such that the error component E was between 10 and 20. For six animals studied, N = 12 (n = 6) and E = 13. A post hoc sample size test required a minimum of 5 animals (n = 4.05) for $K_{Pyr \rightarrow Lac}$ using the following test:

$$n = \frac{2\sigma^2(Z_\beta + Z_{\alpha/2})^2}{|\bar{x}_1 - \bar{x}_2|} \tag{4.3}$$

where Z_β is the desired power (0.84 for 80% power), $Z_{\alpha/2}$ is the desired level of statistical significance (1.96, 95% confidence interval, α = 0.05), $\bar{x}_1$ and $\bar{x}_2$ are the means of both groups, and σ is the standard deviation of the outcome variable. Power was calculated using the following critical value:

$$Z_{Power} = \frac{|\bar{x}_1 - \bar{x}_2|}{standard\ error(x_{1i} - x_{1i})} - Z_{\alpha/2} \tag{4}$$

where *Power* is the area to the right of Z_{Power} on a standard normal distribution.

Table 4.1: MAD-STEAM MRSI derived parameters in the liver, adjacent normal, and tumor (*n = 5*, high grade only). Effect size (Cohen's D), power (percent area less than Z_{Power} on standard normal distribution), and significance (two-sided, paired student's t-test) are reported between tumor and adjacent normal tissue. *Denotes *p-value* < 0.05.

	Tumor	Adjacent Normal	Liver	Effect Size	Powe	Significance
$K_{Pyr \rightarrow Lac}$	0.49 ±	0.04 ± 0.03s^{-1}	0.22 ± 0.13s^{-1}	1.316	100%	0.003*
$Lac_{from\ Pyr}/Pyr_{from\ Lac}$	43.8 ± 57.0	1.38 ± 2.40	0.31 ± 0.30	0.373	97.3%	0.157

4.3 Results

4.3.1 Correlation with Activity and Expression

$K_{Pyr \rightarrow Lac}$ was highly correlated with the maximum reaction velocity, V_{max}, of LDH (Spearman: ρ = 0.943 and *p-value* = 0.017, Figure 4.5) with a slope Δ = 5.71 nmol NADH/mg protein (R^2 =

0.962), suggesting that at 80mM hyperpolarized $^{13}C_1$-pyruvate saturates the LDH enzyme and thus measures the maximum velocity of the enzyme (n = 6).

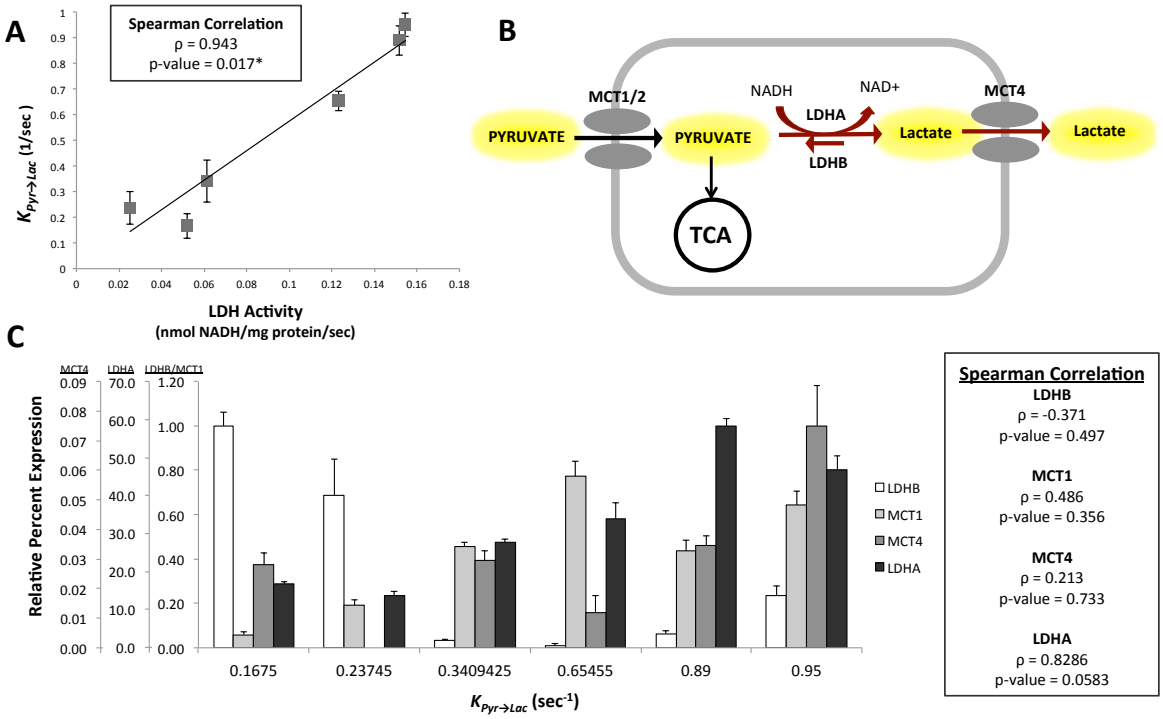

Figure 4.4: **(a)** LDH activity (V_{max}) was highly correlated with $K_{Pyr\rightarrow Lac}$ measured with tumor voxel. *Denotes statistical significance with α = 0.05. **(b)** Schematic of primary factors affecting the rate of conversion of hyperpolarized pyruvate-to-lactate. **(c)** mRNA expression of LDHA, which encodes the M subunit, and LDHB, which encodes the H subunit of the lactate dehydrogenase enzyme, and mRNA expression of monocarboxylate transporters MCT1 and MCT4, which shuttle pyruvate into and lactate out of the cell, respectively. Data are shown as relative fold differences from the house keeping gene, L19, and compared to $K_{Pyr\rightarrow Lac}$ values also measured within primary tumor in transgenic model of liver cancer in the region where tissue was taken for LDH activity assays.

4.3.2 Localization of Regions with High LDH Activity

Statistically significance increases in $K_{Pyr\rightarrow Lac}$ were observed within tumors in a transgenic model of prostate cancer compared to adjacent normal tissue using the MAD-STEAM MRSI sequence (n = 5, Figure 4.5, Table 4.1). MAD-STEAM images showed improved contrast to metabolism by suppressing signal from flowing spins. Additionally, the improved localization of $K_{Pyr\rightarrow Lac}$ demonstrated higher rate constants for prostate cancer than adjacent normal tissue (*p-value* = 0.003, Table 4.1, high-grade tumors with >60% poorly differentiated cells), demonstrating high contrast-to-noise between the tumor and normal adjacent tissue (Table

4.1). Moreover, parametric maps of $K_{Pyr\rightarrow Lac}$ revealed heterogeneity within tumors as shown in Figure 4.5 and Table 4.2.

TABLE 4.2. Tumor grade (PD – poorly differentiated, WMD – well or moderately differentiated, and N – normal) and MAD-STEAM $K_{Pyr\rightarrow Lac}$ derived parameter within ROI (region of interest).

Animal	$K_{Pyr\rightarrow Lac}$	LDHA	LDHB	LDHA-to-LDHB	Grade	Ki67	Metastatic
1	0.950	58.41	0.06	973.50	99.9% PD, 0.1% WMD	99 %	No
2	0.890	46.79	0.22	212.68	100% PD	99 %	No
3	0.690	27.83	0.03	911.47	99% PD, 1% WMD	95 %	Yes
	0.237	-	-	-	7 % PD, 93 % WMD	40 %	-
4	0.620	-	-	-	100 % PD	99 %	Yes
	0.168	16.89	0.93	18.13	25 % N, 75% WMD	15 %	-
5	0.655	33.76	0.01	3376	99 % PD	99 %	No
6	0.341	13.68	0.63	21.71	95 % WMD, 5 % PD	30 %	No

4.4 Discussion & Conclusions

The advantage of the dynamic MAD-STEAM MRSI approach is two-fold. First, it improves sensitivity to metabolism by removing signals within the vasculature and the need to correct for arterial input. Secondly, it provides a robust and simple method for parametric mapping with increased specificity to cellular exchange, which can be used to identify regions with high enzymatic activity. Using MAD-STEAM, high-grade cancerous regions with high LDH activity were detected. Moreover, $K_{Pyr\rightarrow Lac}$ maps revealed heterogeneity within tumors and secondary metastatic nodules.

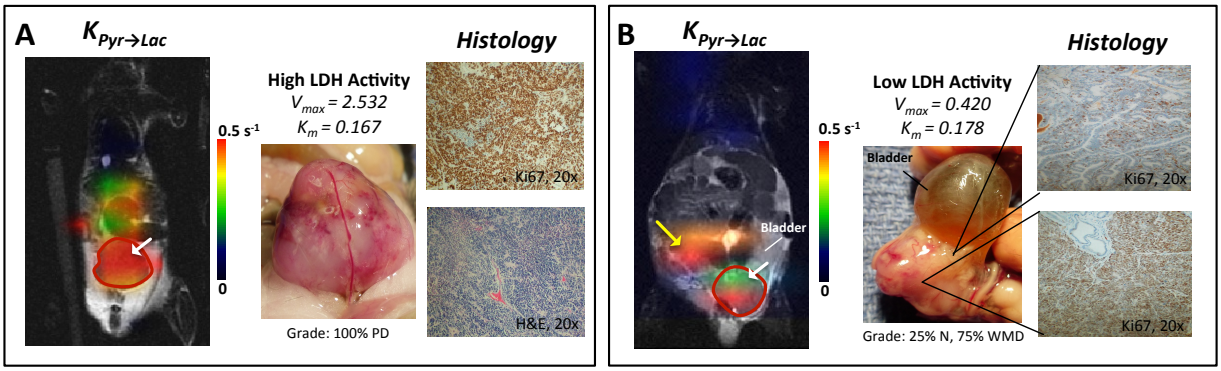

Figure 4.5: $K_{Pyr→Lac}$ reveals heterogeneity within tumors and a large metastatic para-aortic lymph node mass (yellow arrow, verified with pathology). High $K_{Pyr→Lac}$ values with corresponding high enzymatic activities of LDH were observed in high-grade regions (PD – poorly differentiated, WMD – well or moderately differentiated, and N – normal). The primary tumors are encircled in red. White arrows indicate approximate regions where tissue was collected for LDH activity assays and tumor grading. LDH activity V_{max} is reported in x10^{-3}µmol NADH/min/[protein] and K_m is reported in mmol Pyruvate.

This technique is not limited to the measurement of LDH activity and could be used to measure other enzymes' activity such as alanine transaminase (ALT/GPT1), where there is a known increase in conversion of pyruvate-to-alanine during tumor formation[22], or to measure the activity of isocitrate dehydrogenase 1 (IDH1) via the conversion of α-ketoglutarate to 2-hydroxyglutarate[19]. In the field of oncology, this new technique of non-invasively measuring *in vivo*, enzymatic activity has great medical research and clinical significance, as it could be used to identify particularly aggressive regions within tumors, monitor cancer progression, and follow response to therapy. Outside of the field of oncology, the technique has broad applications including the diagnosis of metabolic diseases and tool for the study of biochemistry *in vivo.*

Chapter 5. Simultaneous Measurement of Carbon-13 MR Spin-Relaxation, Facilitated Diffusion, and Exchange

The following chapter is adapted from: Swisher et al. in the Proceedings of International Society for Magnetic Resonance in Medicine, 2013.

In this work, we present a new MR spectroscopy approach for measuring exchange, diffusion, and relaxation, simultaneously. This new approach employs the Metabolic Activity Decomposition – Stimulated Echo Acquisition Mode (MAD-STEAM) method whereby exchange can be directly observed through "phase tagging". Moreover, this new approach was designed for hyperpolarized (HP) substrates such that it is rapid and does not require magnetization renewal. Diffusion weighting from stimulated echoes was isolated from relaxation by varying the dephasing gradient. While varying the dephasing gradient imparts variable diffusion sensitivity, the decay route caused by relaxation remains unchanged.

In this project we measured exchange, diffusion, and relaxation of hyperpolarized substrates simultaneously for the first time *in vivo* and *in vitro*. Potential applications are broad including measurement of diffusion-controlled reactions, relaxation in exchanging systems, cellular transport, enzyme activity, molecular interactions, and studying the cellular environment. In addition to having increased accuracy in the measurement of reaction rates and enzyme activity, this new approach is also particularly sensitive to facilitated transport, which could be used to measure activity of cell membrane transporters.

5.1 Background

5.1.1 Motivation

MRS of HP substrates has shown clinical potential when applied to a variety of other pathologies such as cardiovascular disease[105–109], inflammation[30], and type 2 diabetes[31]. Recently, HP substrates have been developed as biomarkers of redox[110], pH[111], and vascularity[112,113]. It has also been used to study a number of different phenomena in chemistry including rapid chemical reactionship[114], molecular interactions, such as ligand-receptor interactions[115–117], and low-population reaction intermediates[118].

However, in all of these applications the acquired signal is a combination of the substrate's environment, exchange and relaxation. *In vivo* the acquired signal is further complicated by cellular membrane transport, the cellular environment, perfusion, and agent delivery. Previous methods do not offer the ability to measure T_1 relaxation and transport directly for exchanging spins. The goal of this work was to overcome this limitation by developing a new method to separate and measure concomitant relaxation, diffusion, and exchange of hyperpolarized substrates.

5.1.2 MADSTEAM Measurements of Relaxation and Diffusion

Metabolic Activity Decomposition – Stimulated Echo Acquisition Mode (MAD-STEAM) is a recently introduced approach to directly detect exchange, metabolic conversion, or more generally, any frequency shift during a mixing time can be directly observed through "phase tagging"[14,15]. MAD-STEAM is similar to conventional approaches such as exchange

spectroscopy (EXSY), but is advantageous in that it only requires a single encoding step[14]. Moreover, it is ideal for studying *in vivo* metabolism because the stimulated echo sequence can concurrently remove signals from bulk flowing spins, providing improved contrast to cellular metabolism[83,92].

Using MAD-STEAM the effective spin-relaxation, $T_{1,Eff}$, of multiple metabolites can be quantified with improved accuracy by separating newly generated metabolites from metabolites present during encoding. Recently, we showed that that the $T_{1,\mathrm{Eff}}$ of lactate observed after infusion of hyperpolarized pyruvate was significantly shorter in tumors, suggesting a different cellular environment of lactate, in addition to increased conversion of pyruvate-to-lactate, $K_{\mathrm{Pyr}\rightarrow\mathrm{Lac}}$[15]. However, the $T_{1,Eff}$ of lactate as measured using the existing method is subject to both spin-relaxation and diffusion effects. Here, we modified the MAD-STEAM approach to separate diffusion weighting from T_1 relaxation effects.

5.1.3 Cellular Membrane Transport and Hypervascularization in Cancer

This new technique is particular relevant to the field of oncology where both leaky vasculature and high vascularity are a result of sustained angiogenesis, a hallmark of cancer[119], and may alter the T_1 of metabolites. Meanwhile, expression of membrane transporters such as Slc16a family moncarboxylate transporters MCT1 and MCT4 (Slc16a1 and SLc16a3, respectively), which shuttle pyruvate and lactate between the intracellular and extracellular space, may affect the diffusion of metabolites. This has clinical implications because stromal MCT4 has been shown to predict clinical outcome[68] in triple negative breast cancers[70]. Another study in patients with glioblastomas (GBM) showed that upregulation of MCT4 correlated with a significantly shorter survival and an aggressive

mesenchymal subset of GBM in comparison to patients with intermediate expression[120]. Birsoy et al. showed that MCT1 expression correlates with glycolysis upregulation in cancer cells which may be a marker of sensitivity to anticancer therapies that target glycolytic enzymes, such as 3-bromopyruvate (3-BrPA)[121].

In this work we present a new method to separate and measure both relaxation and diffusion, in addition to exchange, to provide unprecedented biologic information about the cellular environment *in vivo*. To better investigate cell transport such as the facilitated transport of lactate out of the cell via MCT4, as shown in Figure 5.1, long diffusion times on the order of transport were used because of their added sensitivity to boundaries rather viscosity. Potential applications are broad including the measurement of diffusion-controlled reactions, molecular interactions, relaxation in exchanging systems, cellular transport, enzyme activity, and studying the cellular environment. This technique maybe particularly valuable in the field of oncology because of the unique biological information it provides where both the rates cellular membrane transport and enzyme catalyzed reactions can be separated and measured. For instance, the hyperpolarized [1-^{13}C]-lactate signal following the injection of [1-^{13}C]-pyruvate is an affected by both MCT4 and lactate dehydrogenase (LDH), both known to be up regulated in cancer and associated with prognosis, can now be measured independently and simultaneously within a single acquisition.

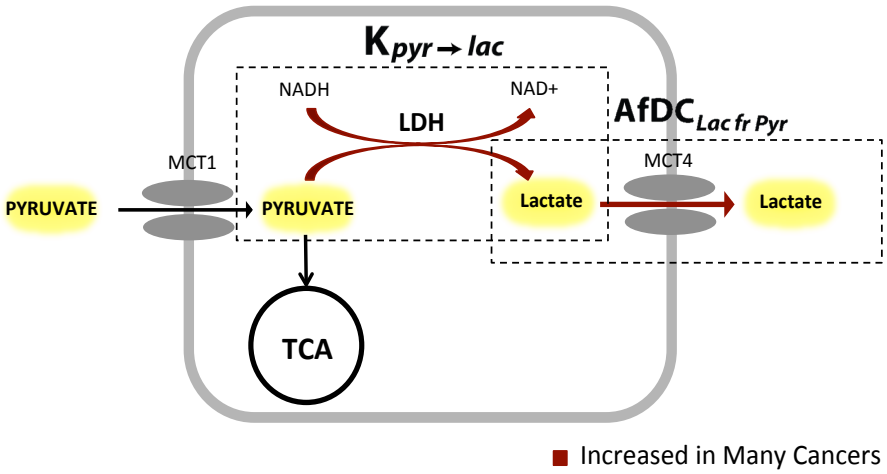

Figure 5.1: Schematic of hyperpolarized [1-^{13}C]-pyruvate uptake into the cell, conversion to hyperpolarized [1-^{13}C]-lactate, and efflux of lactate out of the cell via MCT4 and Multiparametric parameters that describe the exchange, $K_{Pyr\rightarrow Lac}$, and $AfDC_{Lac\ fr\ Pyr}$.

5.2 Theory

5.2.1 Diffusion and Relaxation

Diffusion weighting can be isolated from relaxation by varying the gradient strength between the first two 90^{o} pulses in a repetition of the MAD-STEAM, as shown in Figure 5.2. While varying the diffusion gradient imparts variable diffusion sensitivity, the decay route caused by relaxation remains unchanged. Such that when the trains of FID's are acquired, they will decay with the same T_1 relaxation and the difference in their signal attenuation will be due variable gradient strength alone. With this information, diffusion can be separated from T_1 relaxation effects.

Mathematically, the signal can de described by the following equation:

$$S(t) \propto e^{-t/T_1} e^{-b(t)ADC} = S_a * e^{-t/T_1} e^{-t(\gamma G\delta)^2 ADC} \quad (5.1)$$

Where $S_a = e^{-(\gamma G\delta)^2 (\frac{\delta}{3}) ADC}$ for a square gradient and is a constant that describes the signal attenuation present during the experiment. γ is the gyromagnetic ratio and δ is the

dephasing gradient duration. Thus, the $T_{1,eff}$ can be described by $T_1/(1 + T_1(\gamma G\delta)^2 ADC)$, such that ADCs and T_1s can be estimated by varying diffusion gradient strength.

5.2.2 Exchange and Flux

As shown by Larson et al., STEAM in the presence of metabolic conversion creates a phase shift dependent on the resonance frequency and dephasing-rephasing time (τ), $\Delta\varphi = 2\pi f\tau$ which can be used to "phase tag" metabolites ($\Delta\varphi \approx \pm\pi/2$) and directly observe real-time metabolism[14,15]. In the single case of a single repetition, the dephasing-rephasing time (τ) equals half the echo time, $\tau = TE/2$.

The first 90° – 90° encoding and crusher result in the following encoding along M_z.

$$M_{z,encode,1}(\vec{x}, f_{enc}) = M_o \cos\left(\psi\left(\vec{G}, \vec{x}\right) + \phi(f_{enc})\right)\hat{z} \tag{5.2}$$

Where spatial encoding, $\psi\left(\vec{G}, \vec{x}\right) = -\gamma \int_0^T \vec{G}\,(t)dt$, results from the dephasing-rephasing gradients and spectral encoding, $\varphi(f) = 2\pi(f - f_o)\tau$, results from precession during the dephasing-rephasing time. f is the precession frequency of an isochromat, and f_o is the center frequency of the RF pulses and receiver[14]. The effect on the magnetization by the third pulse, which rotates the magnetization into the transverse plane and the first rephrasing gradient, can be described by multiplication with the following rotation matrix[14]:

$$R\left(\vec{G}, \vec{x}, f\right) = \exp\left(i\left(\psi\left(\vec{G}, \vec{x}\right) + \phi(f)\right)\right) \tag{5.3}$$

If a small tip angle is used, the magnetization left in z will not rephase, such that the magnetization stores the original "phase tag". The magnetization following the third 90° in the first repetition is given by[14]:

$$M_{rep,1}(\vec{x}, f_{enc}, f_1) = M_{z,encode,1}(\vec{x}, f_{enc}) R\left(\vec{G}_1, \vec{x}, f_1\right) \tag{5.4}$$

$$= M_o \cos\left(\psi\left(\vec{G}_1, \vec{x}\right) + \phi(f_{enc})\right) \times \exp\left(i\left(\psi\left(\vec{G}_1, \vec{x}\right) + \phi(f_1)\right)\right) \quad (5.5)$$

$$= \frac{1}{2} M_o \left[exp(\mathrm{i}\left(2\psi\left(\vec{G}_1, \vec{x}\right) + \phi(f_1) + \phi(f_{enc})\right) + \exp\left(i\left(\phi(f_1) - \phi(f_{enc})\right)\right)\right] \quad (5.6)$$

The first terms integrates to zero giving the following resulting signal is given by:

$$S_{rep,1}(f_{enc}, f_1) = \frac{1}{2} M_o \exp\left(i(\Delta\phi(f_{enc}, f_1)\right) \quad (5.7)$$

Similarly, the magnetization along M_z following a 90° – 90° encoding and crusher for all subsequent repetitions, n, is given by:

$$M_{z,encode,n}(\vec{x}, f_{enc}, f_{n-1}) = M_{rep,1}(\vec{x}, f_{enc}, f_{n-1}) \cos\left(\psi\left(\vec{G}_n + \vec{G}_{n-1}, \vec{x}\right) + \phi(f_{n-1})\right)\hat{z} \quad (5.8)$$

The third pulse rotates the magnetization into the transverse plane, such that the magnetization is given by:

$$M_{rep,n}(\vec{x}, f_{enc}, f_n) = M_{z,encode,n}(\vec{x}, f_{enc}, f_{n-1}) R\left(\vec{G}_n, \vec{x}, f_n\right) \quad (5.9)$$

$$=$$

$$\frac{1}{4} M_o \left[\exp\left(i\left(\psi\left(\vec{G}_n + \vec{G}_{n-1}, \vec{x}\right) + \psi\left(\vec{G}_n, \vec{x}\right) + \phi(f_{n-1}) - \phi(f_{enc}) + \phi(f_n)\right)\right) + exp(\mathrm{i}(\left(\phi(f_{n-1}) - \phi(f_{enc}) + \phi(f_n) - \phi(f_{n-1})\right))\right] \quad (5.10)$$

The first terms integrates to zero and $\phi(f_{n-1})$ subtracts such that the resulting signal is given by:

$$S_{rep,1}(f_{enc}, f_{n-1}) = \frac{1}{2^n} M_o \exp\left(i(\Delta\phi(f_{enc}, f_{n-1})\right) \quad (5.11)$$

This includes the 50% signal loss at each repetition. To improve SNR, alternate preparation schemes could be implemented[83].

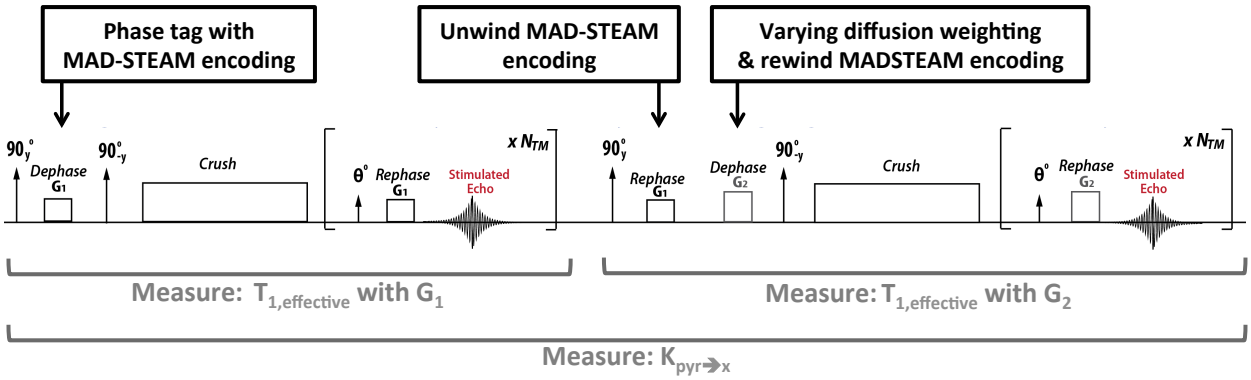

Figure 5.2: Schematic of the Multiparametric MAD-STEAM Pulse Sequence and Diffusion and Exchange Measurement Regimes.

5.2.3 Parameter Estimation

The new multiparametric MADSTEAM sequence can be used to describe the following system,

$$\xrightarrow{-AfDC_P} Pyr \overset{K_{PL}}{\longleftrightarrow} Lac \xrightarrow{AfDC_L}$$

Where K_{PL} describes the net flux of pyruvate to lactate during the mixing time and the $AfDC$ is similar to the apparent diffusion coefficient (ADC), measured in conventional diffusion weighted MRI. However, $AfDC$ is derived from very long mixing times, on the order of transport, and uses small gradients to improve SNR. We also assume that the backwards reaction, K_{LP}, is negligible compared to the forward reaction and with the added diffusion weighting there is decreased sensitivity to this small flux. Because we assume that there is no net conversion of lactate back to pyruvate during the experiment, we only measure the $AfDC_P$ of the original pyruvate. However, because there are two significant lactate populations, $AfDC_L$ can be separated to solve for both the diffusion of lactate molecules that have not gone through exchange, $AfDC_{Lac\ fr\ Lac}$, and the diffusion of lactate

molecules that started as pyruvate and were converted into lactate via the LDH enzyme, $AfDC_{Lac\ fr\ Pyr}$.

To improve sensitivity to K_{PL}, the carbon-13 nuclei on pyruvate and lactate were "phase tagged" using MAD-STEAM. Thus, at each mixing time we were able to determine which metabolites that were originally pyruvate, $Pyr_{Orig}(t)$, and which were originally lactate, $Pyr_{Lac}(t)$. We denote $Pyr_{New}(t)$ as the pyruvate that was tagged as originally having been lactate and $Lac_{New}(t)$ as the lactate that was tagged as originally having been pyruvate. This provides four signals for measurement, compared with two signals when "phase tagging" was not used.

The system dynamics can be described by following equations where G varies with time.

(5.12)

$$\frac{d}{dt}\begin{bmatrix} Pyr_{Orig}(t) \\ Pyr_{New}(t) \\ Lac_{Orig}(t) \\ Lac_{New}(t) \end{bmatrix} = \begin{bmatrix} -k_{pl} - R_P - (\gamma G\delta)^2 AfDC_P & 0 & 0 & 0 \\ 0 & -R_P - (\gamma G\delta)^2 AfDCk_P & 0 & 0 \\ 0 & 0 & -R_L - (\gamma G\delta)^2 AfDC_L & 0 \\ +k_{pl} & 0 & 0 & -R_L - (\gamma G\delta)^2 AfDC_L \end{bmatrix} \begin{bmatrix} Pyr_{Orig}(t) \\ Pyr_{New}(t) \\ Lac_{Orig}(t) \\ Lac_{New}(t) \end{bmatrix}$$

with initial condition $\begin{bmatrix} Pyr_{Orig}(0) \\ Pyr_{New}(0) \\ Lac_{Orig}(0) \\ Lac_{New}(0) \end{bmatrix} = \begin{bmatrix} P_O \\ 0 \\ L_O \\ 0 \end{bmatrix}$

Where $R = {}^{1}/_{T_1}$ is the inverse of the longitudinal relaxation. In order to perform least square estimate of the parameters, (5.12) can be rewritten in terms of the unknown parameters

$$\frac{d}{dt}\begin{bmatrix} Pyr_{Orig}(t) \\ Pyr_{New}(t) \\ Lac_{Orig}(t) \\ Lac_{New}(t) \end{bmatrix} = \begin{bmatrix} -Pyr_{Orig}(t) & -Pyr_{Orig}(t) & 0 & -Pyr_{Orig}(t) & 0 \\ 0 & -Pyr_{New}(t) & 0 & -Pyr_{New}(t) & 0 \\ 0 & 0 & -Lac_{Orig}(t) & 0 & -Lac_{Orig}(t) \\ Pyr_{Orig}(t) & 0 & -Lac_{New}(t) & 0 & -Lac_{New}(t) \end{bmatrix} \begin{bmatrix} k_{pl} \\ R_P \\ R_L \\ AfDC_P \\ AfDC_L \end{bmatrix} \quad (5.13)$$

For each measurement, we get an equation of the form (13), which are stacked to form

$$B = A\theta \tag{5.14}$$

where

$$A = \begin{bmatrix} -Pyr_{Orig}(t_1) & -Pyr_{Orig}(t_1) & 0 & -Pyr_{Orig}(t_1) & 0 \\ 0 & -Pyr_{New}(t_1) & 0 & -Pyr_{New}(t_1) & 0 \\ 0 & 0 & -Lac_{Orig}(t_1) & 0 & -Lac_{Orig}(t_1) \\ Pyr_{Orig}(t_1) & 0 & -Lac_{New}(t_1) & 0 & -Lac_{New}(t_1) \\ \vdots & & & & \vdots \\ -Pyr_{Orig}(t_n) & -Pyr_{Orig}(t_n) & 0 & -Pyr_{Orig}(t_n) & 0 \\ 0 & -Pyr_{New}(t_n) & 0 & -Pyr_{New}(t_n) & 0 \\ 0 & 0 & -Lac_{Orig}(t_1) & 0 & -Lac_{Orig}(t_n) \\ -Pyr_{Orig}(t_n) & 0 & -Lac_{New}(t_n) & 0 & -Lac_{New}(t_n) \end{bmatrix} \quad \theta = \begin{bmatrix} k_{pl} \\ R_P \\ R_L \\ AfDC_P \\ AfDC_L \end{bmatrix} \quad B = \frac{d}{dt}\begin{bmatrix} Pyr_{Orig}(t_1) \\ Pyr_{New}(t_1) \\ Lac_{Orig}(t_1) \\ Lac_{New}(t_1) \\ \vdots \\ Pyr_{Orig}(t_n) \\ Pyr_{New}(t_n) \\ Lac_{Orig}(t_n) \\ Lac_{New}(t_n) \end{bmatrix}$$

The entries of B can be estimated using the approximation

$$\frac{dx}{dt}(t_i) = \frac{x(t_{i+1}) - x(t_{i-1})}{t_{i+1} - t_{i-1}}. \tag{5.15}$$

Then the vector of parameters, θ, can be found with a simple linear least squares fit on equation (5.14).

5.3 Methods

5.3.1 Simulations

To validate the feasibility and optimize the pulse sequence to yield the desired spin isochromats, the sequence was simulated with a Bloch simulator (SpinBench, Heartvista, Palo Alto, CA). To evaluate the accuracy of parameter estimation of various diffusion weighting schemes, data was simulated over a range of parameters: $K_{PL} = 0.01 - 0.5s$ $T_1 = 20 - 50s$ and $AfDC = 1{\times}10^{-4} - 2{\times}10^{-3} mm^2 s^{-1}$. Each combination was simulated over a range of starting SNRs (20-100) with $\delta = 0.1ms$, TR = 1s, N = 20, and iterations = 20 for the following three combinations of gradient strengths: (1) $G_1 = 1\frac{G}{cm}$ and $G_2 = 3\frac{G}{cm}$, $b = 0.5 -$

$85\ s^1mm^{-2}$, (2) $G_1 = 2\frac{G}{cm}$ and $G_2 = 8\frac{G}{cm}$, $b = 1.2 - 608\ s^1mm^{-2}$, and (3) $G_1 = 10\frac{G}{cm}$ and $G_2 = 15\frac{G}{cm}$, $b = 45 - 2138\ s^1mm^{-2}$. The SNR was determined using the average signal of pyruvate at the first time point and dividing by the noise root mean square (rms).

5.3.2 Hyperpolarization of [1-^{13}C]-Pyruvate and ^{13}C –Urea

[1-^{13}C]-Pyruvate mixed with the trityl radical OX063 (Tris[8-carboxyl-2,2,6,6tetra[2-(1hydroxyethyl)]-benzo(1,2-d:4,5-d)bis(1,3)dithiole-4-yl]methyl sodium salt, Oxford Instruments, Abingdon UK) and ^{13}C-urea mixed with the trityl radical OX063 were simultaneously hyperpolarized[95] for phase correction using conventional dynamic nuclear polarization (DNP) methods and a HyperSense DNP polarizer (Oxford Instruments, Abingdon, UK) operating at 3.3T and a temperature of 1.3K. All samples, for both *in vivo* and *in vitro* experiments, were dissolved to produce solutions with 80mM pyruvate and 80mM urea and a biologically appropriate pH (~7.4) with TRIS/NaOH/EDTA dissolution media.

5.3.3 Phantom Validation Studies

HP [1-^{13}C] Pyruvate prepared by dissolution DNP was placed into a syringe under varying conditions. To validate the ability of this new technique to detect changes in T_1 relaxation gadolinium (MAGNEVIST, gadopentetate dimeglumine, Bayer HealthCare Pharmaceuticals Inc.), was added. To validate contrast to diffusion, samples were cooled to ~5°C. Finally, to investigate rate of conversion, the pH was lowered to 4.0 to alter the rate of pyruvate hydration.

5.3.4 Animal Experiments

All animal studies were performed under a protocol approved by the UCSF Institutional Animal Care and Utilization Committee. Mice were anesthetized with 1-1.5% isoflurane and placed on a pad heated to 37°C during the MR experiment. Data were acquired from a slab in z. During each study, 350 μL of the hyperpolarized [1-^{13}C]-pyruvate solution was injected into the mouse over a 12s period, followed by a 0.15 mL normal saline flush. To reduce artifacts from the inflow of pyruvate, data acquisition began 20s following the start of injection of pyruvate. Axial, coronal, and sagittal T_2-weighted fast spin-echo (FSE) images were acquired as anatomical references.

5.3.5 Acquisition and Reconstruction

All data were acquired with a STEAM sequence slab selection, TMs starting at 1s, 20 acquisitions including 2 repetitions of the MAD-STEAM preparation with varying dephasing gradient strengths, 1s temporal resolution, 20° flip angle, and an adiabatic double spin echo[27] and 256 spectral points, 2.5 kHz spectral bandwidth at 3T and 64 spectral points, 4006 Hz spectral bandwidth at 14T. A symmetrically sampled full echo was acquired to preserve phase information[19]. Copolarized ^{13}C-urea was used as a phase reference to correct for phase shifts caused by homogeneous, bulk motion such as respiration, which would affect all metabolites[19].

For animal experiments, a 3T MRI system (GE Healthcare, Waukesha, WI, USA) was used with a dual tuned mouse birdcage coil based on a design used previously[85,97]. For validation experiments, given a main field of 3T TE=13ms was chosen such that $\Delta\varphi_{Pyr\rightarrow Hyd} = \pi/2$ to investigate pyruvate and pyruvate-hydrate's relaxation and diffusion. *In vivo* experiments

were performed on the 3T with both TE = 14ms such that $\Delta\varphi_{Pyr\rightarrow Lac} = \pi/2$ and TE=13ms such that $\Delta\varphi_{\mathrm{Pyr}\rightarrow\mathrm{Hyd}} = \pi/2$. In vivo experiments performed on the 14T were acquired at TE=17.30ms for $\Delta\varphi_{Pyr\rightarrow Lac} = \pi/2$.

5.4 Results

5.4.1 Simulation

Three gradient combinations were evaluated over a range of possible parameters at SNR=20, 50, and 100 with simulated multiparametric MAD-STEAM data. Two small gradients produce the optimal SNR but may be sensitive to perfusion and flow and have reduced diffusion sensitivity. Two large gradients yielding high b-values would attenuate the signal thus reducing the accuracy of the estimated parameters. One small and one modestly large gradient was chosen as the optimal gradient combination. This combination reduces signal attenuation, improving parameter estimation whilst retaining diffusion sensitivity. Additionally the contrast between the two curves will be maximized improving sensitivity to differences in the effective T_1 due to diffusion. Percent error in estimated versus actual value in simulated data is shown in Table 5.1.

Table 5.1. Comparison of percent error in simulated data and estimated parameters for three gradient schemes (n=5, T_1=20-50s, ADC = 1e-4-1e-3 mm^2s^{-1}).

	SNR			
Two Small Gradients: b = 20-900 s/mm²	**200**	**100**	**50**	**25**
ADC	1.68±0.54%	3.14±2.25%	10.32±5.70%	11.78±12.17%
T₁	1.17±0.54%	1.37±0.56%	8.79±2.54%	11.14±9.43%
Two Large Gradients: b = 90-1400 s/mm²				
ADC	3.72±3.84%	7.88±3.70%	11.51±8.18%	42.26±22.24%
T₁	6.13±9.53%	8.07±4.95%	12.74±9.51%	69.82±81.06%
Small & Large Gradients: b = 20-2000 s/mm²				
ADC	1.13±0.63%	2.47±0.55%	6.91±6.60%	11.39±5.48%
T₁	0.71±0.95%	3.74±2.28%	4.14±3.41%	11.83±6.02%

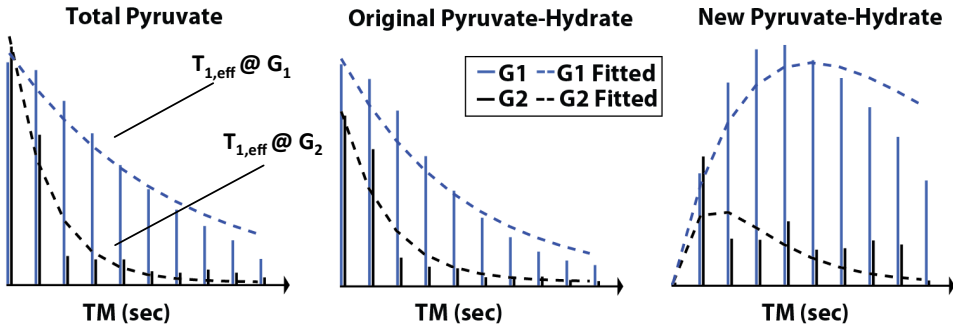

Figure 5.3: Dynamic curves showing the hydration of pyruvate (*TE = 13ms*, *TR =1s,* and $\Delta\varphi_{Pyr \rightarrow Lac} = \pi/2$). Signal normalized to total pyruvate.

5.4.2 In Vitro

Dynamic time series data of the hydration of pyruvate acquired with multiparametric MAD-STEAM *in vitro* is shown in Figure 5.3. As shown in Table 5.2, we observed a decrease in the T_1 relaxation measurements with the addition of gadolinium, a decrease in the *ADC* values at cooler temperatures, reduced exchange with high pH, and increased exchange with low pH.

Table 5.2. Diffusion, relaxation, and conversion parameters of pyruvate in water (TE=13ms, b-values: 65-1734s/mm^2, pH = 7-8 unless otherwise indicated). *This experiment was performed first, so pyruvate and pyruvate-hydrate may not have reached equilibrium causing increased exchange.

	$K_{Pyr \rightarrow Hyd}$	ADC_{Pyr}	$T_{1,Pyr}$	ADC_{Hyd}	$T_{1,Hyd}$
Room Temperature (~ 24 °C)	0.047 s^{-1}*	24.5x10^{-4}mm^{2}s^{-1}	59.0 s	25.0x10^{-4} mm^{2}s^{-1}	50.0 s
Cooled (~ 5 °C)	0.016 s^{-1}	8.07x10^{-4}mm^{2}s^{-1}	52.4 s	10.0x10^{-4} mm^{2}s^{-1}	45.0 s
With Gadolinium (5% vol)	0.014 s^{-1}	24.0x10^{-4}mm^{2}s^{-1}	15.0 s	17.1 x10^{-4}mm^{2}s^{-1}	13.0 s
Low pH (4.0)	0.030 s^{-1}	19.3x10^{-4}mm^{2}s^{-1}	58.1 s	21.4x10^{-4}mm^{2}s^{-1}	57.7 s

5.4.3 In Vivo Feasibility

HP carbon-13 diffusion coefficients, T_1 relaxation, and rates of conversion and exchange were measured simultaneously *in vivo* as shown in Figure 5.4. The showed feasibility of the technique *in vivo.*

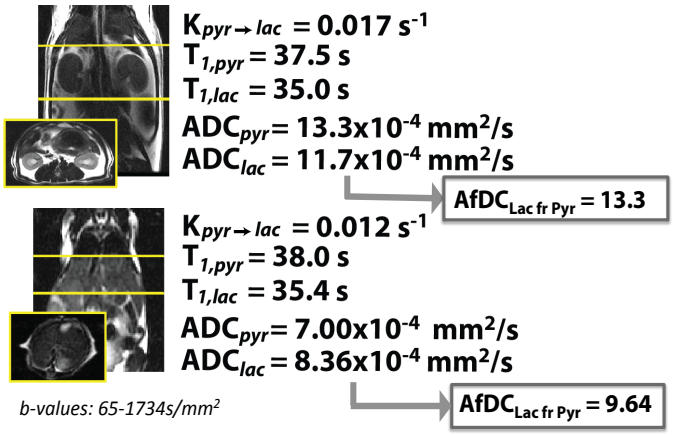

Figure 5.4: Feasibility of Multiparametric MAD-STEAM acquisition *in vivo*.

5.5 Discussion & Conclusions

Methods were developed to measure exchange, diffusion, and T_1 relaxation of HP substrates simultaneously. In general, this multiparametric approach to MAD-STEAM can be used to study any system where spins experience a frequency shift. Potential applications are broad including measurement of diffusion-controlled reactions, relaxation in exchanging systems, cellular transport, enzyme activity, molecular binding, and studying the cellular environment. In the field of oncology, this method has applications for describing both the rates of cellular membrane transport such as MCT4 and enzyme catalyzed reactions such as LDH, which are known be highly expressed in cancer and associated with poor prognosis.

Chapter 6. Dynamic UltraFast 2D EXchange SpectroscopY (UF-EXSY) of Hyperpolarized Substrates

Two-dimensional (2D) NMR is an important tool for revealing molecular structure and dynamics. However, the technique is limited by the inherent low sensitivity, resulting in typical acquisition times for 2D NMR spectra ranging from minutes to hours[89]. In Carbon-13 NMR, this is particularly pronounced whereby only ~1% of carbon atoms are ^{13}C isotope. Hyperpolarization can be used to boost NMR's sensitivity, including capable of yielding signals that exceed those currently afforded by the highest-field spectrometers by several orders of magnitude, providing the sensitivity equivalent of ~10^6 scans[4].

However, its nonrenewable longitudinal magnetization and short lived signal makes it incompatible with conventional 2D NMR acquisitions. Here, we present a new UltraFast method for acquiring dynamic 2D EXchange SpectroscopY (UF-EXSY) that reconstructs 2D EXSY spectra from 1D spectra based of phase accrual during the echo time. Unlike conventional approaches to acquire 2D EXSY data, the UF-EXSY reconstruction utilizes a simple STEAM encoding sequence, requiring only a single encoding step within a single shot, which does not require renewable longitudinal magnetization making it well-suited for hyperpolarized substrates. Furthermore, it requires only a single shot to acquire high-resolution 2D EXSY spectra making ideal for dynamic detection of many exchange pathways.

We validated this method in simulations and hyperpolarized phantom experiments observing the hydration of pyruvate. We also applied this technique in cell studies where both forward and backward exchange of pyruvate-lactate and pyruvate-hydrate were resolved in time. Most,

significantly increased conversion of lactate-to-pyruvate was observed with decreased expression of the Moncarboxylate Transporter 4 (MCT4), which regulates the efflux of lactate out of the cell is known to indicative a more aggressive phenotype in a number of cancers.

6.1 Background

6.1.1 2D-NMR

In the fields of chemistry and biology, multidimensional NMR acquisitions, which differentiate and correlate the resonances arising from individual sites onto multiple frequency axes are commonly used to study structure, dynamics, reaction state, proteins, the chemical environment of molecules, or any other sample that contains nuclei possessing spin[122]. These experiments are intrinsically longer than their conventional one-dimensional (1D) counterparts, and thus the SNR can suffer from reduced time for signal averaging. Increased sensitivity can be gained with increase the magnetic field, but this leads to only modest returns despite large investments on higher field strengths.

Not surprisingly, there has been an increased interest in developing alternatives that prepare nuclei in 'hyperpolarized' states, whose spin population differences depart significantly from the usual $\approx 10^{-5}$ Boltzmann distributions. DNP yields over a 10,000-fold increase in SNR[4], which is greatly larger than what can be achieved by multiscan signal averaging. Using hyperpolarization with its inherent dramatic increases in sensitivity provide a unique opportunity to probe previously undetectable NMR phenomena.

6.1.2 2D-NMR and Hyperpolarized Substrates

However, the detection of hyperpolarized substrates requires sequence modifications to overcome challenges such as non-renewable longitudinal relaxation, T_1, and short acquisition times on the order of T_1. The non-renewable longitudinal relaxation makes conventional acquisitions schemes for multidimensional NMR impossible which are based on collection an array of scans that are identical to one another except for the serial incrementing of evolution delays. Similar to Frydman and Blazina, the serial indirect domain t_1 encoding of 2D NMR is replaced by a parallelized procedure endowing different positions within a sample of length with inequivalent evolution times[89], but uses a symmetric slice selective excitation rather than a gradient acting in combination with a frequency-swept excitation for preparation and small dephasing and rephrasing gradients rather than an oscillating field gradient.

The acquisition and reconstruction presented here relies on principles of phase accrual used with the 1D acquisition, Metabolic Activity Composition with Simulated Echo Acquisition Mode (MAD-STEAM)[14]. The main advantages are the simplicity of the sequence and reconstruction, the RF and gradient requirements allow this sequence to be implemented on clinical MRI scanners, and the use of larger sampling regions can also reduce error from turbulence from rapid injection of hyperpolarized substrates. Furthermore, this is first application of 2D EXchange SpectroscopY (EXSY) in the hyperpolarized Carbon-13 field. This is significant, where cell both preclinical animal studies of hyperpolarized substrates[21,69,76,123], as well as the first-in-man clinical trial[20], have focused heavily on the exchange of hyperpolarized metabolites as markers of disease.

6.1.3 Motivation

MRS of hyperpolarized substrates is a powerful tool for investigating tissue metabolism and kinetics *in vivo*[77,124]. In addition to detecting increased conversion of pyruvate-to-lactate, $K_{Pyr\rightarrow Lac}$, in tumors using MAD-STEAM, we recently showed that the backwards reaction of lactate-to-pyruvate, $K_{Lac\rightarrow Pyr}$, was significantly smaller in tumors compared to normal tissue with a transgenic model of prostate cancer[15], consistent with a decreased LDHB expression and increased MCT4 and LDHA expression. However, the $K_{Lac\rightarrow Pyr}$ as measured previously can be corrupted by alanine-to-pyruvate and hydrate-to-pyruvate conversion, warranting a method to separate these signals.

In metabolism, flux and exchange often occur in both directions examples include reductive carboxylation[125,126], lipogenesis and its regulation of citrate and α-ketoglutarate[127], glutamine addiction[22,50,87,128], gluconeogenesis, and the isoenzyme composition of LDH. Detection of these pathways have great diagnostic and biomedical research potential. For instance, the directionality of reactions within the citric acid cycle has become an area of increased interest as reductive carboxylation has been shown to support tumor growth[125]. However, the signal from hyperpolarized experiments reports on only the bulk spin-exchange and cannot differentiate concomitant spin-exchange.

In this work a simple Ultra Fast method to acquire and reconstruct hyperpolarized 2D EXchange SpectroscopY (UF-EXSY) dynamically is developed. This new approach could provide improved specificity to cancer metabolism, provide directionality of metabolic pathways, and shed light on exchange and flux of hyperpolarized substrates.

6.2 Theory

6.2.1 Acquisition

Conventional Dynamic EXSY requires the third RF pulse to be 90º necessitating renewable longitudinal magnetization not available in hyperpolarized substrates and many repetitions to obtain the entire indirect spectral direction (Figure 6.1a). The dynamic UF-EXSY pulse sequence is rapid and does not require renewable longitudinal magnetization making it ideal for hyperpolarized substrates (Figure 6.1b). Key features include the symmetric slice selection gradient played with the first 90º RF pulse, gradients blips, which rephrase echoes sequentially, and a small flip angle, which allows for dynamic acquisition of 2D EXSY spectra. This data can be used to measure build up curves for multiple measured signal intensities that can be fit to an exchange model to extract kinetic rates of interconversion (Figure 6.1c,d).

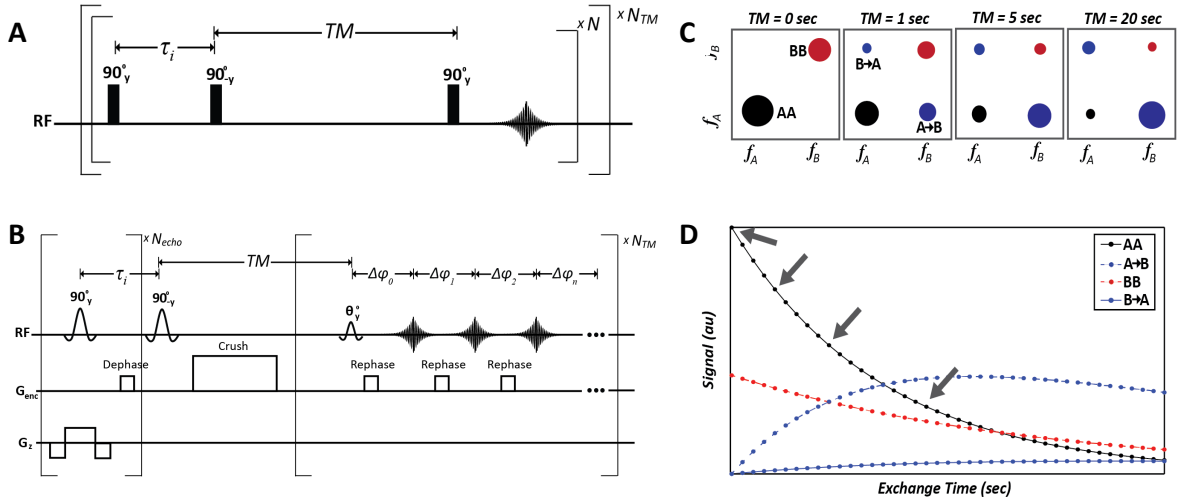

Figure 6.1: (a) Conventional Dynamic EXchange SpectroscopY (EXSY) requires the third RF pulse to be 90º necessitating renewable longitudinal magnetization not available in hyperpolarized substrates and many repetitions to obtain the entire indirect spectral direction. **(b)** Dynamic UltraFast EXSY (UF-EXSY) pulse sequence is rapid and does not require renewable longitudinal magnetization making it ideal for hyperpolarized substrates. Data was acquired with N_{echo} = 3, N_{TM} = 5-20, slab selection in Δz = 3mm, Δτ = 8.575ms, 20º flip, 1-2sec temporal resolution, 64 spectral points, and 4006Hz spectral bandwidth. **(c)** Schematic of dynamic 2D exchange spectra and **(d)** simulated build up curves from four measured signal intensities in (c) which can be fit to an exchange model to extract kinetic rates of interconversion. Arrows denote time points shown in 2D spectra (c).

6.2.2 Reconstruction

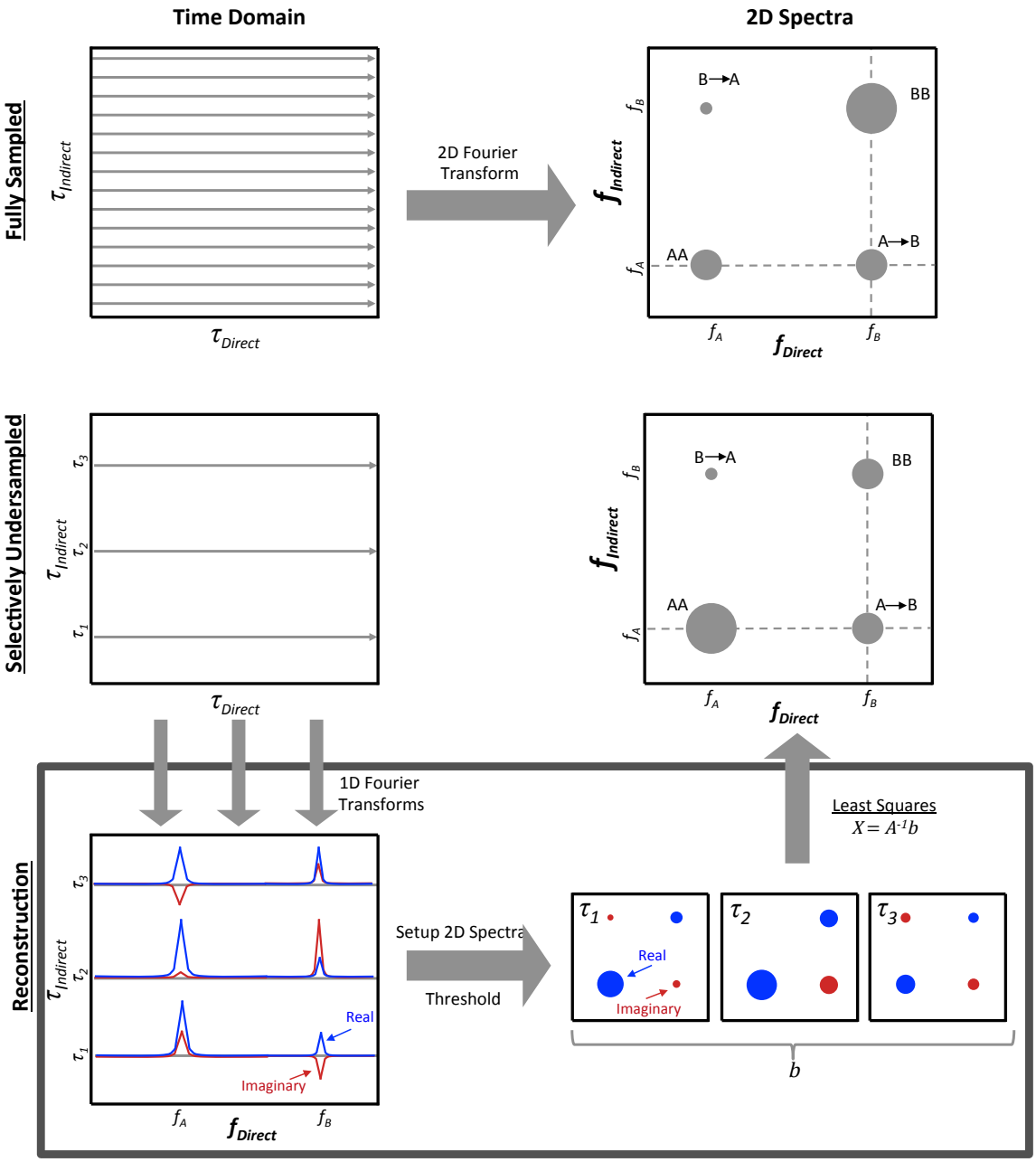

Figure 6.2: Schematic of Ultra Fast EXchange SpectroscopY (UF-EXSY) reconstruction. Using conventional EXSY the 2D spectra can is reconstructed from the magnitude of the 1D spectrum but requires many τ repetitions. Using the UF-EXSY reconstruction the entire 2D spectra can be reconstructed from a few echoes with high spectral resolution in the indirect frequency direction equal to that of the direct frequency direction. For each frequency, f_i, with a signal greater than the noise threshold in the direct frequency direction the cross peaks are calculated using Equation 6.1 or with linear least squares based on the phase accrual and frequency difference between the $\Delta\varphi = 2\pi\Delta f\tau$ between every other frequency with a signal also greater than the noise threshold. By using the real and imaginary spectra rather than the magnitude only, the 2D spectra can be reconstructed from a single acquisition. Multiple τ times are used to correct for concomitant exchange pathways at a single resonance and for τ_i where $\Delta\varphi(\Delta f) \approx 0$ and the number of echoes is greater than the number of concomitant exchange pathways at a single resonance.

Using conventional EXSY reconstruction from the magnitude of the data requires many τ repetitions to reconstruct the 2D spectra. By choosing the τ repetitions wisely, only a few repetitions can be used to acquire the entire 2D spectra. Using the UF-EXSY reconstruction, shown in Figure 6.2, the entire 2D spectra can be reconstructed from only a few echoes with high spectral resolution in the indirect frequency direction equal to that of the direct frequency direction.

The reconstruction relies on the phase accrual, $\Delta\varphi = 2\pi\Delta f\tau$, of exchanging spins with a resonance frequency difference, Δf, at each echo time, $TE = 2\tau$, which has been used to directly observe flux and exchange of a single reaction in real-time[14]. For each frequency, f_i, with a signal greater than the noise threshold in the direct frequency direction the cross peaks are calculated using the following equation:

$$S(f_1, f_2) = \begin{cases} \frac{Imag\{S(f_1,f_2)\}}{\sin(2\pi(f_1-f_2)\tau)}, & f_1 \neq f_2 \\ Re\{S(f_1, f_2)\} - \sum_i \frac{Imag\{S(f_1,f_2)\}}{\tan(2\pi(f_1-f_i)\tau)}, & f_1 = f_2 \end{cases} \quad (6.1)$$

By using the real and imagery spectra rather than the magnitude only, the 2D spectra can be reconstructed from a single echo utilizing the phase accrual, $\Delta\varphi = 2\pi\Delta f\tau$, between all other frequencies with a signal greater than the noise threshold. However, multiple τ times need to be used to correct for concomitant exchange pathways at a single resonance with the acquisition of multiple echoes where $\Delta\varphi$ varies from Δf between the different exchange pathways (Figure 6.3e,f). Additionally it is required that for at least one τ_i $\Delta\varphi(\Delta f) \neq 0, \pi, 2\pi, \ldots$. As the number of τ_i increases, the accuracy will increase. To ensure accuracy at least one τ_i is required for each concomitant spin exchange. For instance in the renal cell carcinoma models, UMRC6 and UOK262, there are three concomitant spin exchanges at pyruvate's resonance, namely lactate-to-pyruvate,

hydrate-to-pyruvate, and alanine-to-pyruvate. Because alanine SNR is below the noise threshold, we only need two τ_i to accurately reconstruct the data shown in Figure 6.3.

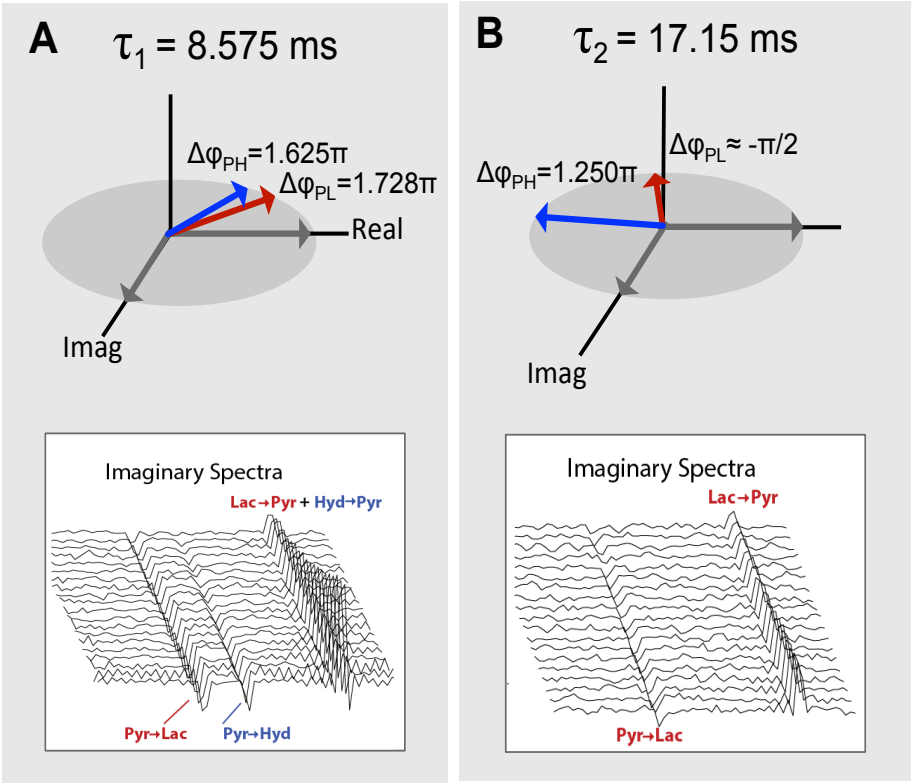

Figure 6.3: Schematic of phase dependence of the **(a)** first and **(b)** second echo and their corresponding raw dynamic imaginary spectra from UOK262 renal cell carcinoma cell-filled alginate microspheres (TR=1s). Alternate phase schemes could be used to maximize SNR in imaginary spectra (specifically to increase hydrate SNR). Up to an 83% increase in SNR can be recovered in the 2D spectra after reconstruction.

Of course, each τ_i repetition will result in a loss in SNR. However, much of the original SNR can be recovered as is function of τ_i where the SNR of a cross peak is defined by

$$SNR(\Delta f) = \frac{S}{n\sigma}\left(\frac{1}{\sin(\Delta\varphi(\tau_1))} + \frac{1}{\sin(\Delta\varphi(\tau_2))} + \cdots \frac{1}{\sin(\Delta\varphi(\tau_n))}\right) \tag{6.2}$$

where n is the number of τ_i. As stated previously, to detect a cross peak it is necessary that for at least one echo, $\Delta\varphi$ is between 0 and $\pm\pi$ with sufficient SNR.

More generally, the entire spectra can be described by the following equations:

$$cross\ peaks: \quad X = A^{-1}a \tag{6.3}$$

$$diagonal: \quad Y = b - \sum_f XB \tag{6.4}$$

where

$$A = \begin{bmatrix} \sin(\varphi_{1,\tau 1}) & \sin(\varphi_{1,\tau 2}) & \cdots \\ \sin(\varphi_{2,\tau 1}) & \sin(\varphi_{2,\tau 2}) & \cdots \\ \vdots & \vdots & \ddots \end{bmatrix} \qquad a = \begin{bmatrix} Im\{S(\tau_1)\} \\ Im\{S(\tau_2)\} \\ \vdots \end{bmatrix} \tag{6.5}$$

$$B = \begin{bmatrix} \cos(\varphi_{1,\tau 1}) & \cos(\varphi_{1,\tau 2}) & \cdots \\ \cos(\varphi_{2,\tau 1}) & \cos(\varphi_{2,\tau 2}) & \cdots \\ \vdots & \vdots & \ddots \end{bmatrix} \qquad b = Re\{S(\tau_1)\} + Re\{S(\tau_2)\} + \cdots \tag{6}.$$

Such that the 2D reconstructed spectra can be described by the following equation:

$$\mathbf{2D\ Spectra} = \mathbf{X} + diag(\mathbf{Y}) \tag{6.7}$$

where

$$X(f_i) = \begin{bmatrix} New\{S(f_i \to f_0)\} \\ New\{S(f_i \to f_1)\} \\ \vdots \end{bmatrix} \tag{6.8}$$

and

$$Y(f_i) = Orig\{S(f_i)\} \tag{6.9}$$

For more complex spectra than shown in this work noise amplification occurring near each π crossing, can be reduced with Tikhonov Regularization,

$$min \qquad \|AX - a\|^2 + \|\Gamma X\|^2 \tag{6.10}$$

such that the cross peaks can be found using the following least square operation

$$X = \begin{bmatrix} A \\ \lambda I \end{bmatrix}^{-1} \begin{bmatrix} a \\ 0 \end{bmatrix} \tag{6.11}.$$

Alternatively, SNR can be optimized and error due to noise amplification can be reduced by choosing τ based on *a priori* knowledge of cross peak locations. The UF-EXSY reconstruction workflow is summarized in Figure 6.4.

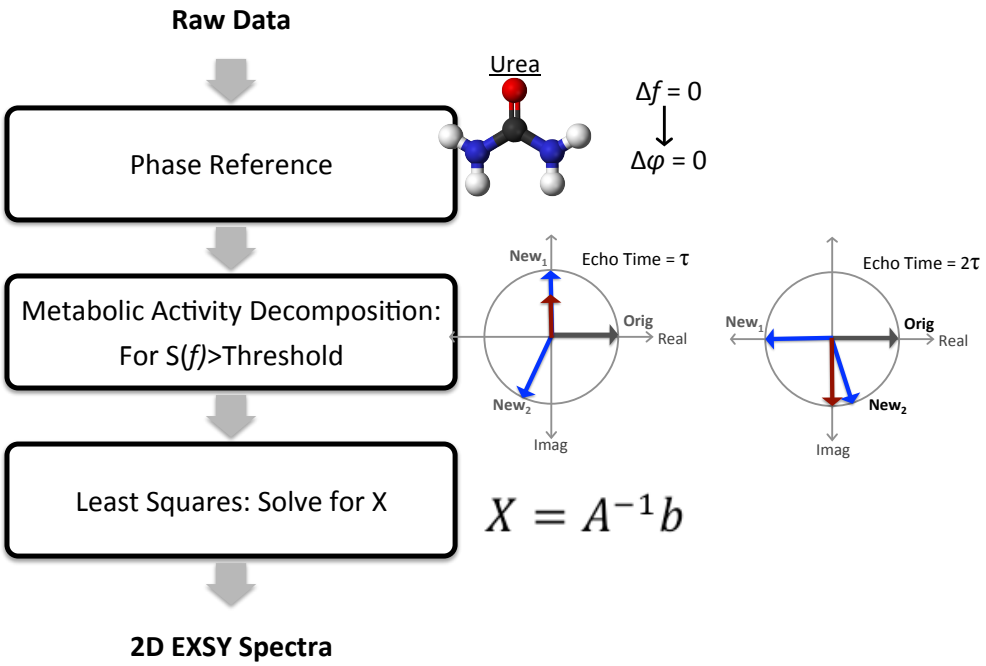

Figure 6.4: Workflow of Ultrafast EXchange SpectroscopY (UF-EXSY) reconstruction.

6.3 Methods

6.3.1 NMR Experiments

These studies were conducted on a 14.1T wide-bore microimaging spectrometer equipped with 100G/cm gradients and a 10mm broadband probe (Agilent Technologies). The sequence shown in Figure 1b was acquired with $\Delta\tau$ = 8.575*ms*, t_{phase} = 52 μs, G_{phase} = 5 *G/cm*, t_{crush} = 10 *ms*, G_{crush} = 15 *G/cm*, N_{echo} = 3, *TM* = 1-2 *sec* temporal resolution, N_{TM} = 5-20 repetitions, Δz = 3*mm*, 20° flip, 64 spectral points, and 4006Hz bandwidth. Noise was subtracted to remove cross peak artifacts. T_2 signal loss between echoes was small and considered negligible because of the long T_2s of the hyperpolarized^{129}. However, in the case of short T_2s, signal loss between echoes be can corrected in the reconstruction.

6.3.2 Polarization of [1-^{13}C] Pyruvate and ^{13}C-Urea

[1-^{13}C]-Pyruvate mixed with the trityl radical OX063 (Tris[8-carboxyl-2,2,6,6tetra[2-(1hydroxyethyl)]-benzo(1,2-d:4,5-d)bis(1,3)dithiole-4-yl]methyl sodium salt, Oxford Instruments, Abingdon UK) was hyperpolarized using conventional DNP methods and a HyperSense DNP polarizer (Oxford Instruments, Abingdon, UK) operating at 3.3T and a temperature of 1.3K. For validations studies, [1-^{13}C]-Pyruvate was copolarized[95] with ^{13}C-urea mixed with the trityl radical OX063. All samples were dissolved to produce solutions with 80mM pyruvate and 80mM urea and a biologically appropriate pH (~7.4) with TRIS/NaOH/EDTA dissolution media.

6.3.3 Cell Studies

UMRC6 cells are representative of localized human clear cell RCC[16], and were a gift from Dr. Bart Grossman (MD Anderson Cancer Center, Houston, TX; obtained January, 2010; authenticated using STR profiling, October 2012). UOK262 cells are derived from a metastasis of the highly aggressive hereditary leiomyomatosis RCC (HLRCC), which is characterized by mutation of the TCA cycle enzyme fumarate hydratase[17]. UOK262 cells were a gift from Dr. W. Marston Linehan (National Cancer Institute, Bethesda, MD; obtained May, 2010; authenticated using STR profiling, October 2012). All cells were grown in Dulbeco's Modified Eagle's Medium (DMEM) with 4.5 g/L glucose. The cells were passaged serially and were used for assays and magnetic resonance experiments between passages 2 to 10 and at 60% to 80% confluency. These two cell lines were chosen because of their differential expression of the monocarboxylate transporter 4 (MCT4), which regulates lactate efflux out of the cell and similar lactate dehydrogenase (LDH) activity[69].

6.3.4 Hyperpolarized ^{13}C magnetic resonance bioreactor experiment

Cells were electrostatically encapsulated into 2.5% w/v alginate microspheres as previously described[69] and then loaded into a magnetic resonance–compatible bioreactor. Approximately 800 µL of microspheres were perfused in the bioreactor with DMEM H-21 media at a flow rate of 0.5 mL/min. During acquisition the flow was turned off during acquisition. The media was kept at 37°C with water-jacketed perfusion lines and was maintained at 95% air/5% CO_2 via gas exchanger. All bioreactor studies were conducted on the 14T Varian Inova NMR microimaging system (Agilent Technologies) with a 10 mm, triple-tune, direct-detect, broadband probe at 37°C.

6.3.5 MCT4 Inhibition

The inhibitor 4,4-diisothiocyanatostilbene-2,2-disulfonate (DIDS) was chosen based on its specificity for MCT4[62]. UF-EXSY experiments with hyperpolarized $^{13}C_1$-Pyruvate were acquired before and 40 minutes after the administration of 1mM DIDS in a UOK262 cell line in a bioreactor.

6.3.6 In Vivo

To show feasibility a UOK262 cell line was implanted in the renal capsule of Rag2 immunocompromised mouse. 24 µL of $^{13}C_1$-Pyruvate co-polarized with 55 µL of ^{13}C-Urea. 80mM HP $^{13}C_1$-Pyruvate and ^{13}C-Urea buffered solution (pH ~ 7.4) was injected over 15 seconds. Acquisition started at 20 seconds after the start of injection. 8mm x 8mm x 8mm voxels were acquired in both the normal and abnormal kidney. The pulse sequence was adapted to be able to select multiple voxels with the addition of slice selection gradients played during the second and third RF pulses (shown in Figure 6.7a).

6.4 Results

6.4.1 Validation

Using MAD-STEAM single-voxel acquisition and reconstruction, real-time conversion and exchange can be directly observed for a pathway specified by the echo time (TE)[14]. Similarly, we utilize the phase accrual from a set of paired 90° STEAM preparation pulses and a dephasing gradient to observe multiple exchange pathways rapidly and simultaneously all within a single acquisition as shown in Figure 6.5.

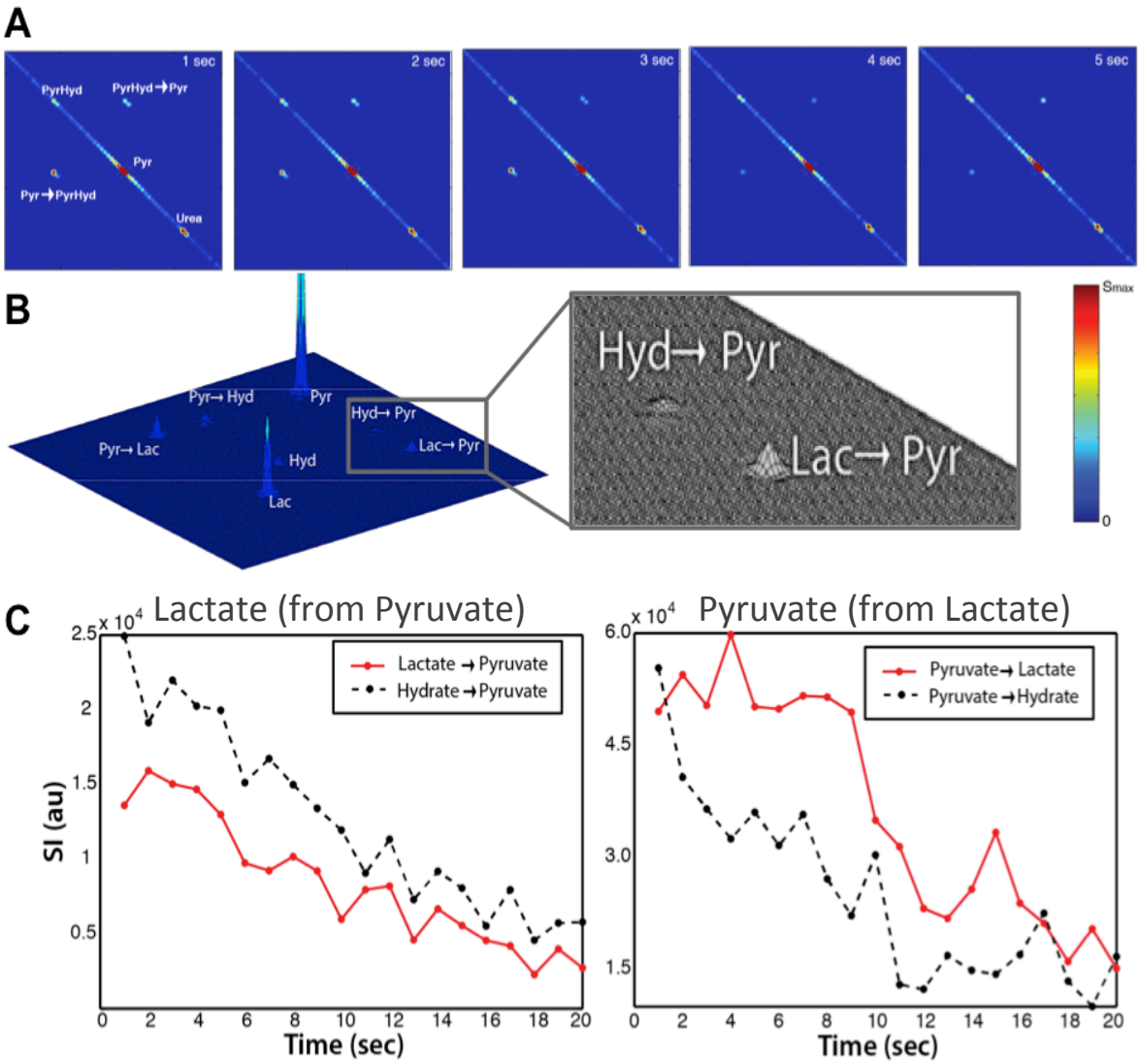

Figure 6.5: (a) dynamic EXSY spectra of pyruvate hydration co-polarized with ^{13}C-Urea, **(b)** 2D sum spectra and **(c)** time course of pyruvate-lactate and pyruvate-hydrate from forward and reverse reactions in MR-compatible bioreactor using UOK262 renal cell carcinoma cell-filled alginate microspheres.

The method was validated with a Bloch simulator (SpinBench, Heartvista, Palo Alto, CA) and with hyperpolarized phantom experiments where the hydration of pyruvate was observed dynamically (Figure 6.5a). We have also applied this technique to cell studies where both forward and backward exchange of pyruvate-lactate and pyruvate-hydrate was resolved and acquired dynamically (Figure 6.5 b and c).

This technique reconstructs 2D EXSY spectra from 1D spectra based on phase accrual during each echo time. This acquisition has similarities to previous ultrafast 2D NMR techniques with the major difference being that simple STEAM encoding of discrete slices is used instead of frequency-sweep excitation pulses[122]. The reconstruction is advantageous as it can be used to yield high spectral resolution in the indirect direction without parsing the signal for the indirect direction and is thus more sensitive to low SNR cross peaks.

6.4.3 Cell Studies of Flux and Transport

The HP flux of lactate-to-pyruvate in the aggressive, metastatic UOK262 cell line was less than in the less aggressive UMRC6 cell line supporting the hypothesis that lactate efflux reduces the conversion of lactate-to-pyruvate, $k_{Lac\rightarrow Pyr}$. MCT4 inhibition with the DIDIS inhibitor in UOK262 cell line resulting in a statistically significant decrease (95% Confidence Interval, paired students t-test) in the, $k_{Pyr\rightarrow Lac}$, conversion of lactate-to-pyruvate conversion as shown in Figure 6.6. This new method revels high MCT4, which are known mutations in aggressive cancers via modulated exchange of lactate and pyruvate.

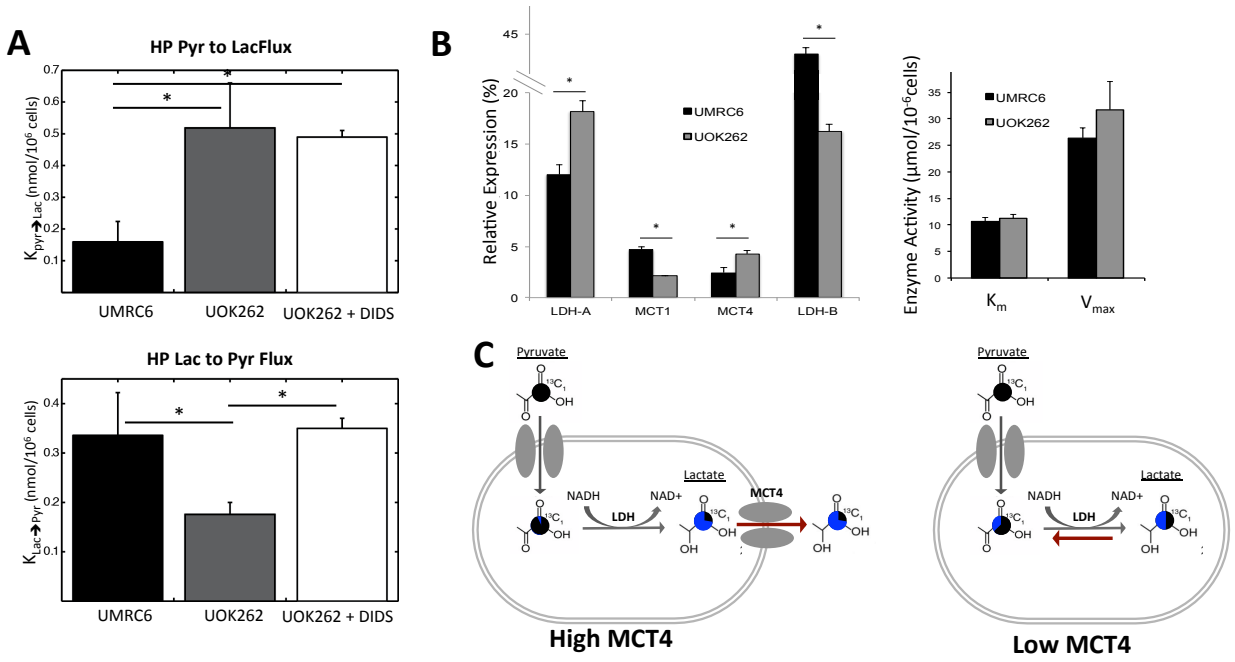

Figure 6.6: (a) Dynamic UltraFast 2D EXchange SpectroscopY (UF-EXSY) of Hyperpolarized Substrates detects high MCT4 in metastatic renal cell carcinomas and revels decreased conversion of lactate back to pyruvate with the efflux of lactate out of the cell. **(c)** Analysis of relevant enzyme expression/activity and transporter expression in the two cell lines *(Adapted from Keshari et al. 2013).* LDH activity as measured by Km (µmol pyruvate/106 cells) and Vmax (µmol NADH/s/106 cells) in the two cell lines (N = 6 each) mRNA expression of LDHA and monocarboxylate transporters 1 and 4 (MCT1 and MCT4), relative to internal β-actin expression, in the two cell lines (N = 6 each).. All values are reported as mean ± SE. *, significant difference ($p < 0.05$). **(c)** Schematic of pyruvate and lactate exchange with high and low MCT4. Pie charts indicate the percentage of the label that is generated after encoding, "New", shown in blue and the percentage that were present during encoding, "original" shown in black.

In the normalized (Total Carbon) dynamic time curves, decreased pyruvate from lactate was observed in the UOK262 cell line compared to the UMRC6 cell line and UOK262 cell line with DIDS, a MCT4 inhibitor. The signal of pyruvate from lactate was not different between the UMRC6 cell line and the UOK262 cell line with DIDS. As it expected the the UMRC6 cell line, which has a reduced LDH-A to LDH-B ratio in conjunction with reduced low MCT4, had both high pyruvate from lactate signal and a low lactate signal not going through exchange (Figure 6.7).

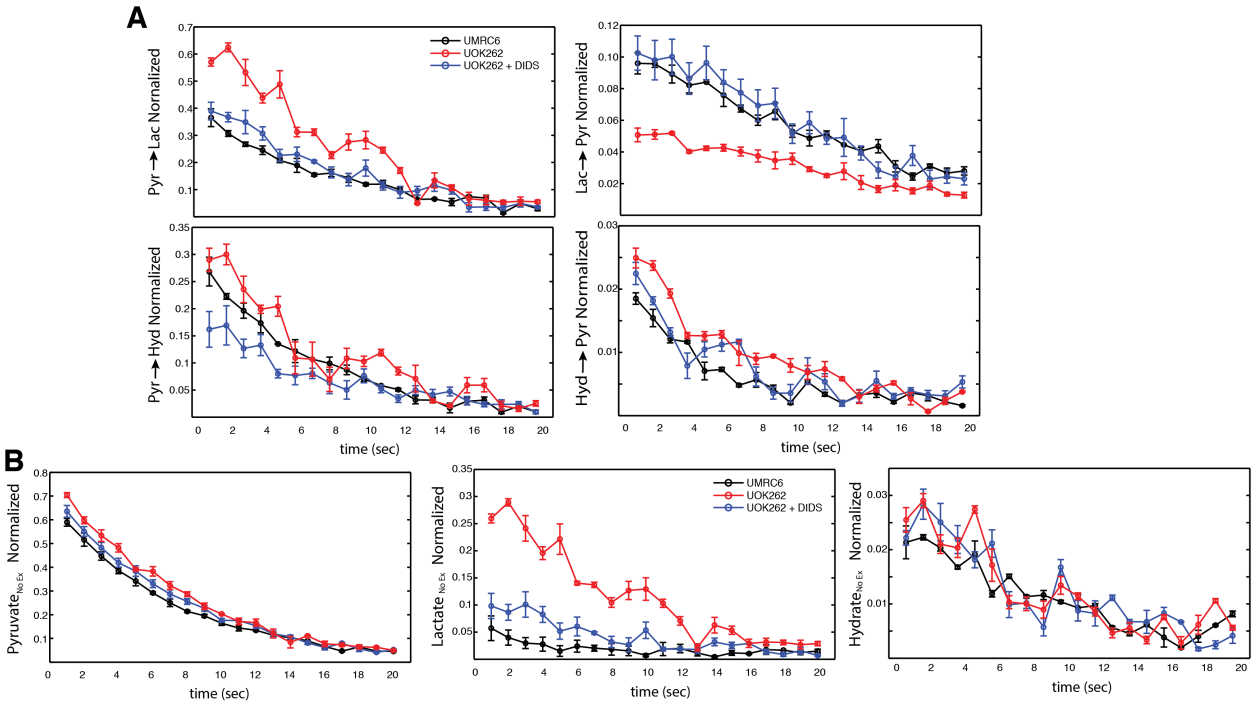

Figure 6.7: Dynamic time course from 2DEXSY spectra of **(a)** cross-peaks (spins that have gone through exchange) and **(b)** diagonals (spins that have not gone through exchange). Data was normalized to the total carbon signal excluding Urea.

6.4.5 In vivo Feasibility

Finally, the sequence was adapted to acquire multiple voxels (Figure 6.8a). Feasibility of the technique was shown *in vivo* in the comparison of a normal kidney and a kidney with implanted UOK262 cell line under the renal capsule (Figure 6.8b-d).

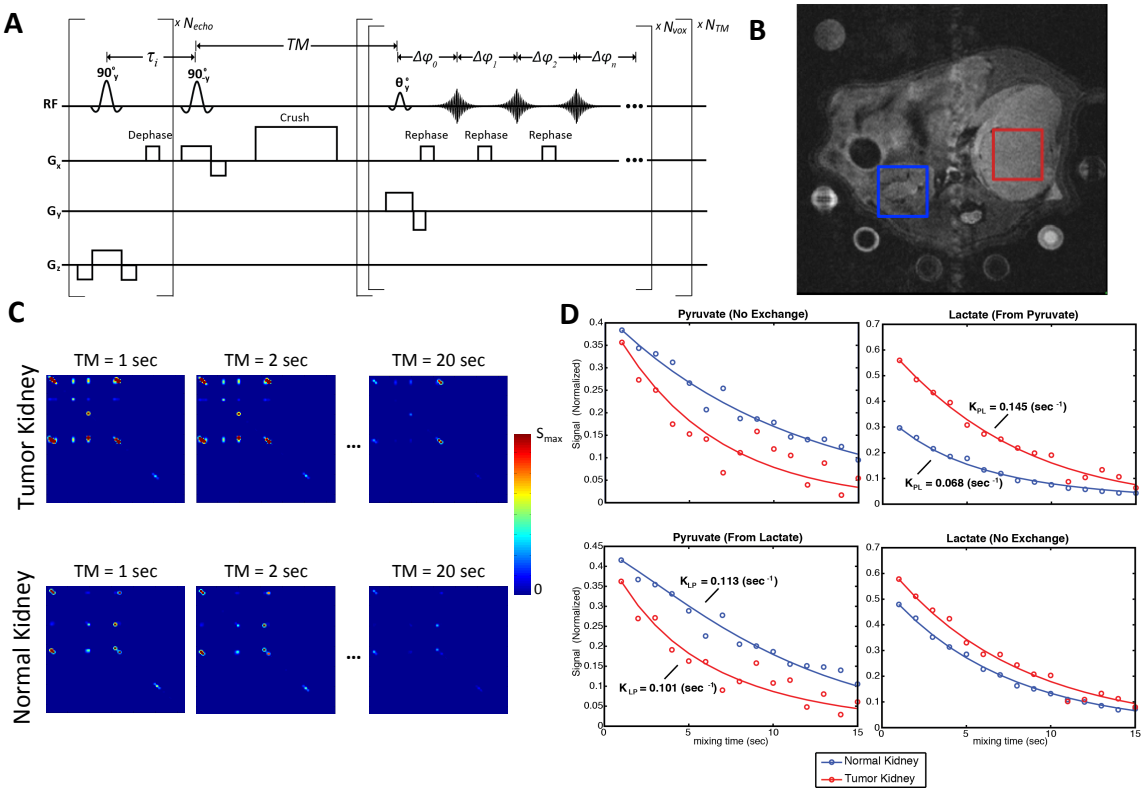

Figure 6.8: In vivo feasibility (a) Multivoxel pulse sequence for *in vivo* studies. **(b)** Location of voxels on T2W anatomical image. One voxel was acquired in a UOK262 implanted tumor and the other was acquired in the contralateral normal kidney. Both voxels were acquired within a single acquisition. **(c)** Dynamic 2D spectra data and **(d)** Dynamic traces with corresponding fitted kinetic parameters show contrast between kidneys.

6. 5 Discussion & Conclusions

In this work, we present a new UltraFast method for acquiring dynamic 2D EXchange SpectroscopY (UF-EXSY) within a single acquisition using principles of MAD-STEAM[14]. The presented dynamic UF-EXSY pulse sequence is rapid and does not require renewable longitudinal magnetization making it ideal for hyperpolarized substrates. Overcoming the three main challenges associated with 2D NMR of hyperpolarized substrates, which are 2D NMR experiments are time intensive, longitudinal magnetization is not renewable, and the signal decays quickly requiring fast acquisition.

The simple reconstruction based of phase accrual makes it ideal for dynamic detection of many exchange pathways. This new approach could provide improved specificity to cancer metabolism in particular providing directionality of metabolic pathways. Outside of the field of oncology, the potential applications of this technique are broad including applications such as solvent hydrogen-exchange, protein interactions, protein folding, and conformational changes such as cis-trans isomerizations and domain movements as wells as to investigate multistep chemical reactions.

Here we applied this technique in cell studies where both forward and backward exchange of pyruvate-lactate and pyruvate-hydrate were resolved in time. The technique provided insights on the effect of transporters on exchange. Moreover, this work showed the potential using bidirectional exchange as a marker of MCT4, which h has been shown to be indicative of aggressive disease in a number of cancers[68,120,130]. More generally, this work highlights the importance of investigating bidirectional exchange, which could have applications including the investigation of directionality in gluconeogenesis, effect of pyruvate kinase isoenzymes, and reductive carboxylation. It can be used with other carbon-13 hyperpolarized substrates such as [2-^{13}C]-Pyruvate or ^{13}C- α-Ketoglutarate. Or more broadly the utilization of phase in 2D NMR acquistions could be adapted to quickly acquire sparse 2D spectra for other nuclei such as ^{1}H, ^{15}N, ^{31}P, and ^{129}Xe.

Chapter 7. Hyperpolarized ^{13}C-pyruvate imaging reveals metabolic differences between oncogene induced signaling pathways

Tumor cells have an altered metabolic phenotype characterized by increased utilization of glutamine as a fuel source[50,40], dysfunction metabolism of citric acid cycle metabolites[131], and diminished oxidative phosphorylation[132,133]. A single oncogene can directly target many enzymes associated with metabolism causing dramatic reprogramming of the metabolic network[32,40,133,25]. The goal of this project was to detect oncogene activation with hyperpolarized ^{13}C-pyruvate magnetic resonance spectroscopic imaging (MRSI) via oncogene-induced metabolic reprogramming in separate switchable models[49] of Myc-driven versus Ras-driven liver cancer.

These results demonstrate that metabolic imaging can be used to differentiate oncogene induced metabolic signaling pathways. Specifically this proof-of-concept study detected changes in hyperpolarized pyruvate-to-alanine conversions as a result of alternate utilization of cofactors α-ketoglutarate and glutamate and ultimately glutamine metabolism in c-myc versus h-ras driven liver tumors. We show for the first time that a hyperpolarized carbon-13 labeled substrate can be used as metabolic imaging agent for non-invasive, *in vivo* monitoring of the presence of h-Ras and more generally for the differentiation of oncogenes via metabolic reprogramming.

7.1 Background

7.1.1 Motivation

Hepatocellular carcinoma (HCC), the most frequent form of primary liver cancer, is the third most common cause of cancer mortality worldwide[134]. In Europe, North America and Australia, the incidence of HCC has doubled since 1983 even though the prevalence of hepatitis B (HBV) infection has been declining[135]. The median survival of HCC is short, less than 12 months from diagnosis, resulting from both late diagnosis and lack of effective treatments[136]. In most cases, by the time the diagnosis is made, the patient is beyond the stage of resection with only 10–20% of HCCs are resectable[137]. Of those patients who are eligible for resection only 10-20% have a 5-year recurrence-free survival[138]. Therefore, most HCC patients will eventually develop advanced disease. Clinical trials cannot recommend a systemic therapy that can be considered the standard for all patients with advanced HCC[139]. However, targeted therapies have shown promise.

7.1.2 Targeting Oncogene-Induced Signaling Pathways

Sorafenib, for instance, targets the RAF kinase in the MAPK/ERK pathway, and is the first FDA approved effective systemic therapy for liver cancer[46]. More generally, in many cancers, a defect in the MAPK/ERK pathway leads to uncontrolled growth[140]. About 25% of all human cancers have a defect in this pathway[141]. There is a clear need to identify patients who would be successfully treated with compounds that can inhibit steps in the MAP/ERK pathway. Here we study upregulation of h-Ras which activates the protein kinase activity of RAF kinase followed by RAF kinase phosphorylating and activating MEK[141–143]. The ability to detect Ras has important implications outside of liver cancer[142–145141–144111–114]. Where Ras, a key player in the MAPK/ERK pathway, is one of the most common oncogenes in

human cancers. Moreover, this work has implications outside of liver cancer, because Soraenib has antitumor activity against a variety of tumor types including renal cell carcinomas[146–148], hepatocellular caricnomas[149], and thyroid cancer[47].

Similarly, CDK inhibitors which target cell-cycle progression, a hallmark of Myc upregulation, have been successfully used to treat c-Myc driven models of breast cancer[150], and more generally selective CDK inhibition may provide therapeutic benefit against certain human neoplasias which require specific interphase CDKs for proliferation[151]. CDK inhibitors have been used to treat a variety of neoplasias[152].

7.1.3 Anatomical Imaging and Treatment Planning

The non-invasive identification of patients who would benefit from targeted therapies using conventional imaging methods such as magnetic resonance imaging (MRI) or computerized axial tomography (CT) remains a challenge. ^{1}H MRI and CT are mostly limited to the detection of gross anatomical changes, which occur after changes in metabolism. Moreover, in a single patient there can be great heterogeneity within a tumor. Using MRI and CT to guide biopsy location has had great success. However, metabolic imaging would add additional beneficial information revealing particularly aggressive sites within the tumor that might not be detectable with conventional imaging techniques, thus guiding biopsy locations. Hyperpolarized ^{13}C MR in conjunction with DNP, would allow for the imaging of aberrant metabolism such as the Warburg effect[24]. In the present study we have further investigated the potential utility of ^{13}C MRSI using HP [1-^{13}C] pyruvate for detecting metabolic reprogramming after oncogene activation.

7.1.4 Metabolic Reprogramming and Oncogene Activation

A single oncogene can directly target many enzymes associated with metabolism causing dramatic reprogramming of the metabolic network. Oncogenes alter the utilization of glutamine and glucose, the two main fuel sources for tumors, which provide precursors for nucleic acids, proteins and lipids, the three classes of macromolecules needed to proliferate[40]. Glutamine metabolism also supplements the pyruvate pool, which is predominantly formed from glucose[25]. As a consequence of the rapid metabolism of these two nutrients, lactate, alanine and $NH4^+$ are secreted by the tumor[40]. Pyruvate sits at a pivotal point in that its metabolism is a result of interactions from both glutamine metabolism and glucose metabolism (catabolism and anabolism). We sought to exploit metabolic reprogramming, specifically altered utilization of glutamine, to detect oncogene activation.

The ability to detect activation of an oncogene non-invasively has clinical implications as it could be used to identify patients that would benefit most from a targeted therapy. In hepatocellular carcinoma (HCC) specifically, the detection of the upregulation of the Ras oncogene is clinically significant because Ras is associated with a poorer prognosis and could be effectively treated with Sorefinib therapy[145]. This novel application of HP ^{13}C MR to detect oncogene activation could be used to predict prognosis, for more robust image-guided biopsies, and to guide treatment decisions.

7.2 Theory

7.2.1 Compressed Sensing

Compressed Sensing is a method to provide accelerated MRI acquisitions to enable improved spatial coverage and or resolution within a given time period[153]. Theoretically, compressed sensing will perfectly reconstruct a sparse data sets. Then, with very high probability, the original signal is recoverable with high accuracy with a convex minimization.

To apply compressed sensing three criteria must be met: (1) the signal must be sparse in some domain, although it does not have to be in the image domain, (2) the aliasing artifacts must be incoherent or noise-like, and (3) a nonlinear reconstruction must be applied that reinforces sparsity of the object or image domain. To meet criterion (2), random sampling in k-space can be utilized to produce incoherent aliasing in image space and improving sparsity[153].

7.2.2 Compressed Sensing and Hyperpolarized Carbon-13 MR Spectroscopy

Spatial resolution in hyperpolarized carbon-13 experiments is limited by short acquisition times and in ability to signal average. Logically, the implementation of compressed sensing in this field has had a number of benefits including improved spatial resolution, increased SNR, and implementation of 3D dynamic spectroscopic pulse sequences.

The most obvious implementation is to undersample in k_x and k_y. The typical hyperpolarized ^{13}C scan is 16×8. Therefore for an increase in speed by a factor of 2, [154] only 8×8 data points can be acquired[155]. However, it has been shown that small sample sizes do

not provide enough sparsity in in wavelet simulations[154,155]. Fortunately, the spectral domain sampled in hyperpolarized ^{13}C experiments is inherently sparse.

Alternatively, an improved approach would utilize the sparsity in the spectral domain by undersampling in the k_f dimension. Implementation of undersampling in the time domain has been previously described by Hu et al. 2010. Compressed sensing was combined with another rapid imaging technique, echo-planar spectroscopic acquisition, whereby k_f and k_x where both undersampled. Unlike k_x and k_y, $k_f = t$ making it more challenging to designa pulse sequence that randomly undersamples k_f. By alternating between k_x *and* k_f, in a flyback acquisition undersampling in both the spectral and spatial domain can be achieved[153].

7.3 Methods

7.3.1 *Hyperpolarization of [1-^{13}C]-Pyruvate and ^{13}C –Urea*

[1-^{13}C]-Pyruvate mixed with the trityl radical OX063 (Tris[8-carboxyl-2,2,6,6tetra[2-(1hydroxyethyl)]-benzo(1,2-d:4,5-d)bis(1,3)dithiole-4-yl]methyl sodium salt, Oxford Instruments, Abingdon UK) was hyperpolarized[4] using conventional dynamic nuclear polarization (DNP) methods and a HyperSense DNP polarizer (Oxford Instruments, Abingdon, UK) operating at 3.3T and a temperature of 1.3K. All samples were dissolved to produce solutions with 80mM pyruvate and a biologically appropriate pH (~7.4) with TRIS/NaOH/EDTA dissolution media.

7.3.2 Animal Experiments

All animal studies were performed under a protocol approved by the UCSF Institutional Animal Care and Utilization Committee. Mice were anesthetized with 1-1.5% isoflurane and placed on a pad heated to 37°C during the MR experiment. During each study, 350 μL of the hyperpolarized [1-^{13}C]-pyruvate solution was injected into the mouse over a 12s period, followed by a 0.15 mL normal saline flush. To reduce artifacts from the inflow of pyruvate, data acquisition was started 20s following the injection of pyruvate. Axial, coronal, and sagittal T_2-weighted fast spin-echo (FSE) images were acquired as anatomical references.

The oncogene's expression was regulated via the tetracycline operator (tet-O). Specifically, the tetracycline-controlled transactivator protein (tTA) regulates the expression of either the c-Myc or h-Ras protein and is regulated with doxycycline (dox) as shown in Figure 7.1a. Two switchable oncogene-driven models were studied and compared to the control (Figure 7.1b).

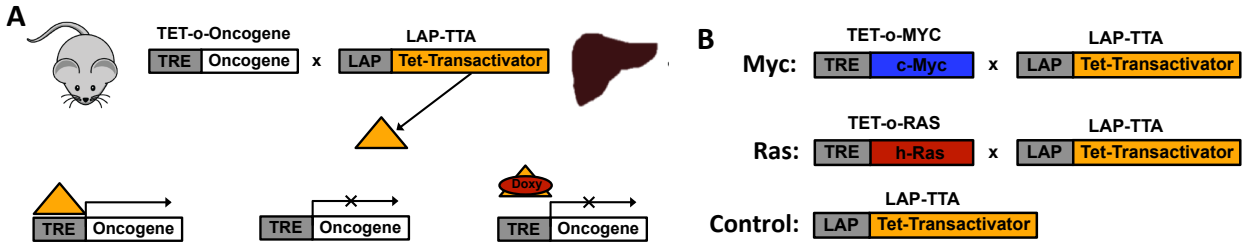

Figure 7.1: Schematic description of models **(a)** Switchable oncogene-driven model **(b)** MYC, RAS, and Control models used in this study.

7.3.3 Acquisition and Reconstruction

All experiments were performed on a General Electric 3T (Waukesha, WI) MRI scanner equipped with 40 mT/m, 150 mT/m/ms gradients, and a broadband RF amplifier. The RF coil was a custom built, dual-tuned $^{1}H/^{13}C$ transmit/ receive design used previously[85]. T2-weighted proton fast spin-echo (FSE) images were acquired and used as the anatomical reference on which ^{13}C spectra were overlaid and co-registered. The axial FSE imaging parameters were as follows: FOV = 8 cm, 192 x 192 matrix, 2 mm slice thickness, and NEX = 6. Carbon-13 hyperpolarized spectra were acquired as a volumetric grid with a compressed sensing 3D-MRSI sequence[155]. Acquisition parameters were as follows: variable flip angle, TE = 140 ms, TR = 215 ms, 16 x 16 in-plane phase encodes, center out phase encode order, 2.5 mm x 2.5 mm in-plane resolution, flyback readout in z with 16 points and 5.4 mm resolution, 581 Hz spectral bandwidth, and 9.8 Hz spectral resolution.

The ^{13}C 3D-MRSI scan was started 30 s after injection of the hyperpolarized ^{13}C-pyruvate and lasted 16 s. To quantify metabolism in the ^{13}C spectra, the areas under the ^{13}C-lactate, ^{13}C-pyruvate-hydrate, ^{13}C-alanine, and ^{13}C-pyruvate resonances (total carbon-13 defined as the sum of all four) in magnitude spectra were calculated. The ratios lactate area to total carbon area (Lac/tCar) and alanine area to total carbon (Ala/tCar) were computed for each voxel and then averaged over all voxels of interest for each mouse to derive the final lac/tCar and ala/tCar values for statistical analysis. To further compare the myc and ras voxels displaying the Warburg effect, high Lactate regions within the tumor were defined and the ala/tCar values were determined for statistical analysis.

7.3.4 Statistical Analysis

For the ^{13}C MRSI statistical analysis, experimental data were divided into three groups, Tet-o-RAS/LAP-tTA, Tet-o-MYC/LAP-tTA, and control (LAP-tTA). Both the Myc and Ras groups were imaged at baseline (Myc or Ras off [n = 6]) and at progression (Myc or Ras on [n = 6], when tumor was clearly visible on a T_2W anatomical imaging scan). These results were compared to normal liver (Tet transactivator control mice [n = 6]). Groups were compared with unpaired, two-sided student's t-test.

7.4 Results

7.4.1 Molecular Characterization of Models

Molecular characterization showed that Myc and Ras were significantly upregulated in the animals studied (Figure 7.2b). Histology and increased alpha-fetoprotein (AFP), a marker for hepatocellular carcinoma (HCC), confirmed the progression (Figure 7.2a, 7.2b). Kaplan-Meier survival curves showed decreased survival in both oncogene-driven models as compared to controls as well as a shorter survival for the ras-driven compared to the myc-driven model (Figure 7.2c). Furthermore, differential mRNA expression in liver tumors driven by Myc and Ras have gene signatures derived from transgenic models cluster tumor and non-tumor patient samples ($p<0.0001$) demonstrating striking segregation of normal and tumor samples suggesting the models share gene expression chances with human liver cancers, and are thus a relevant tool to study metabolic changes associated with tumorigenesis (Figure 7.2d).

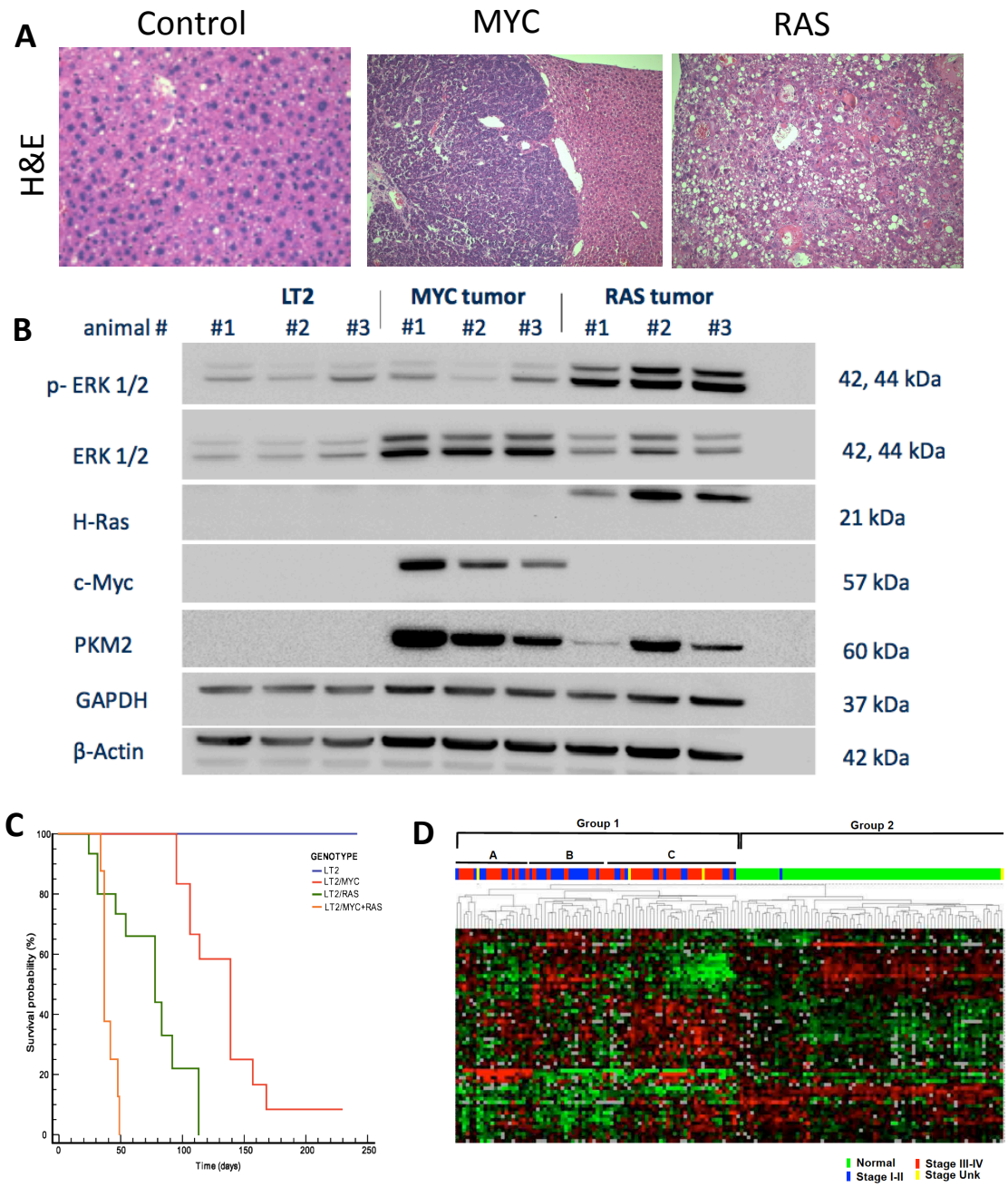

Figure 7.2: Molecular characterization of the tumor models. **(a)** Histology, **(b)** Verification of expression of oncogene activation, **(c)** Kaplan-Meier survival curves, and **(d)** Hierarchical clustering of human data with transgenic models.

7.4.2 Hyperpolarized ^{13}C-pyruvate imaging reveals metabolic differences between oncogene induced signaling pathways

HP carbon-13 conversion of pyruvate to alanine reveals metabolic differences between oncogene induced signaling pathways as shown in Figure 7.3. In the h-Ras driven model, the alanine-to-total carbon remained significantly higher at progression unlike the c-myc driven model (Figure 7.3b) indicative of an alternate signaling pathway shown in Figure 7.3c.

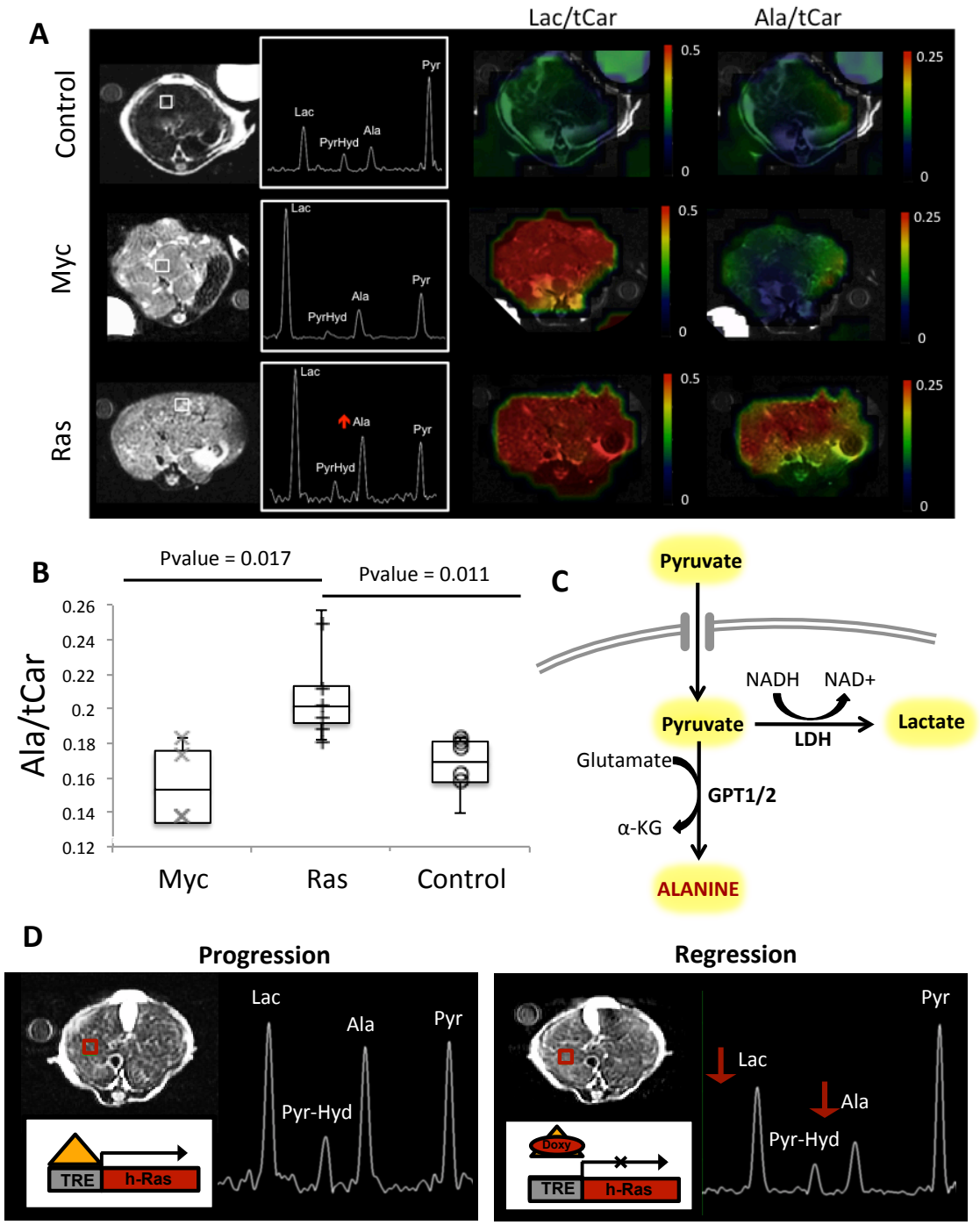

Figure 7.3: (a) Lactate (Lac/tCar) and alanine (Ala/tCar) over total carbon overlays and sample voxels from switchable transgenic models of Myc and Ras driven liver cancer and Control (LT2) showed increased conversion of [1-^{13}C]-Pyruvate to [1-^{13}C]-Alanine. **(b)** Alanine-to-Total Carbon in the Ras driven model of liver cancer was significantly higher than in the Myc driven model or the Control, LT2 (*indicates p-value <0.05). **(c)** Schematic of conversion of Hyperpolarized [1-^{13}C]-Pyruvate. The Ras driven model favors conversion of pyruvate to alanine (shown in red) which was confirmed by **(d)** inhibition of the oncogene h-Ras which reduced Lac/tCar (indicative of decreased Warburg effect) and reduced Ala/tCar.

Since the time to progression varied significantly between the Myc and Ras models and even within the group. Only tumors greater than 1cm were included and only the region abnormal by anatomical imaging was included. We sought to investigate if the cause of increased alanine in the Ras-driven tumors was in fact due to altered signaling pathways and not other factors such as necrosis. Regions-of-interest that exhibited the Warburg effect in the Myc and Ras were compared (Figure 7.4). Alanine-to-total carbon was statistically significant despite potential substrate competition for the HP ^{13}C-Pyruvate suggesting that the effect significant and is a result of altered metabolism.

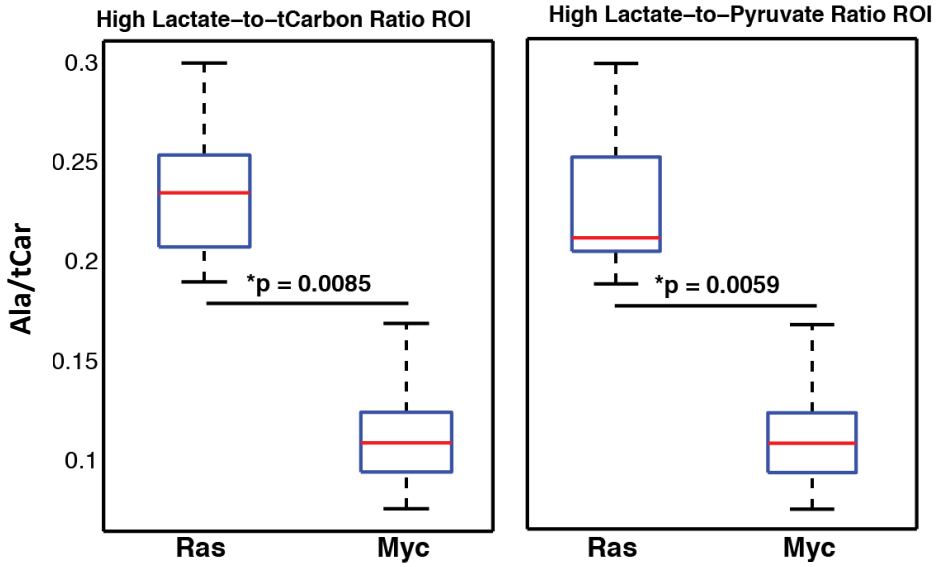

Figure 7.4: Regions-of-interest that exhibited the Warburg effect showed increased conversion to alanine. Comparison of alanine-to-total carbon in tumorigenic regions-of-interest (ROIs) defined by high lactate-to-total carbon within the liver, abnormal ROI by a T_2-weighted anatomical imaging and regions with high lactate-to-pyruvate ratios.

Furthermore, inactivation of the signaling pathway led to a dramatic decrease of tumor relevant metabolites in the h-Ras over-expression model as shown in Figure 7.3d with quantitative analysis shown in Figure 7.5 which further demonstrated that increased alanine at progression is a result of h-Ras activation.

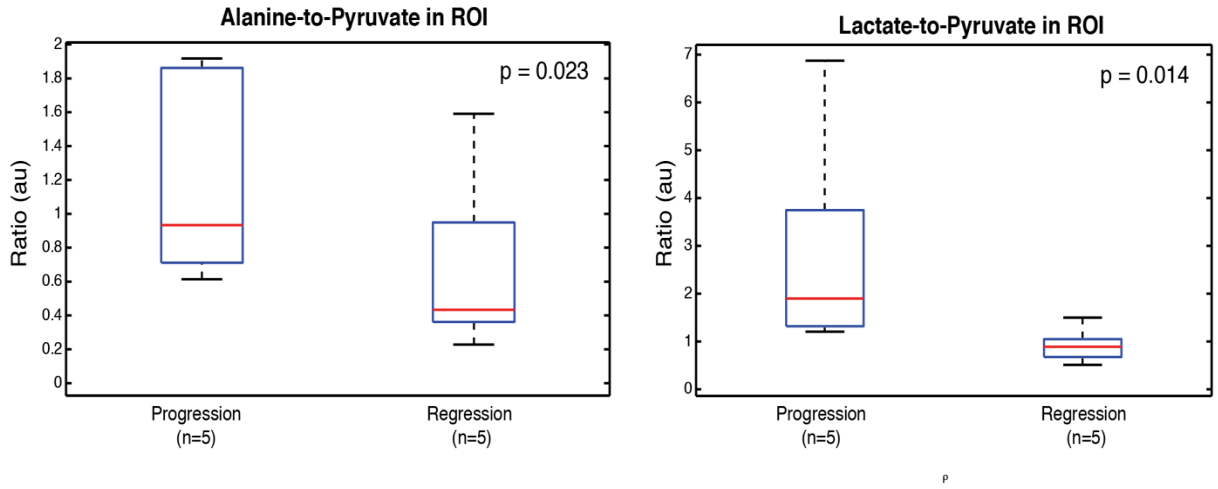

Figure 7.5: Analysis of inhibition of the oncogene h-Ras, which reduced Lac/Pyr (indicative of removal of the Warburg effect). Reduced Lac/Pyr was used a marker of early regression. Ala/Pyr was also reduced with the inhibition of the oncogene.

7.4.3 Increased Conversion of ^{13}C-Pyruvate to ^{13}C-Alanine in hRas is indicative of alternate utilization co-factors α-Ketoglutarate and Glutamate

Enzymes most likely to be associated with increased pyruvate-to-alanine conversion such as Gpt1 and Glud-1 were significantly upregulated. However, Gls-1 was significantly down regulated in the h-Ras-driven tumors compared to the c-Myc-driven tumors (Figure 7.6a). Other factors that could affect conversion such as MCT1 and MCT2, which are the primary transporters for pyruvate's entry into the cell, were not significantly different between the models or control. MCT4, which drives lactate efflux out of the cell, was similarly upregulated in both the Myc and Ras tumors (Figure 7.7c). Thus, the increased conversion of ^{13}C-Pyruvate to ^{13}C-Alanine, which may report on the pool size[156] of the substrates and cofactors in addition to enzymatic activity, is likely indicative of alternate utilization of cofactors, α-ketoglutarate and glutamate.

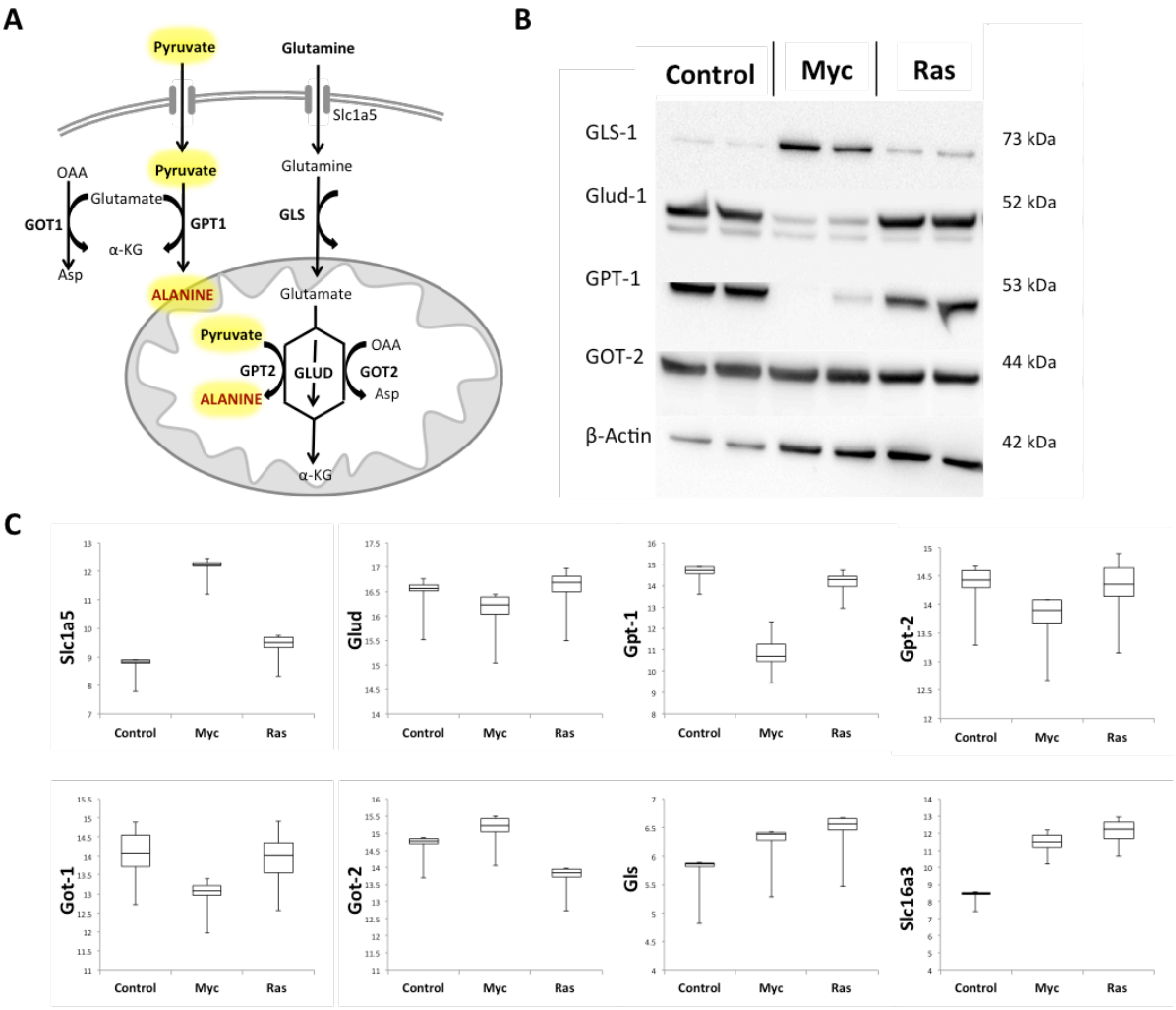

Figure 7.6: The Ras driven model favors conversion of pyruvate to alanine, which maybe due to **(a)** altered oncogene-induced signaling pathway whereby **(b)** increased expression of Gpt-1/2 and Glud-1 coupled with **(c)** decreased transport of glutamine into the cell via Slc1a5 and decreased conversion of glutamine into glutamate via Gls in the Ras model in comparision with the myc model.

Meanwhile, genes associated with the PDH complex and PC were down-regulated in the h-Ras model (Figure 7.7 and 7.8c) limiting pyruvate from entering the TCA cycle (Figure 7.8a). Moreover, mRNA expression suggests that a number of genes associated with the utilization of α-ketoglutarate were altered in the h-Ras model compared to the c-Myc model including Slc5a1 which uptakes glutamine was upregulated in the c-Myc model only. These results support a non-canonical glutamine pathway whereby α-ketoglutarate is conserved in h-Ras in liver cancer[128]. These results also suggest the cause for alanine-to-

total carbon remaining significantly high at progression in the h-Ras model unlike the c-myc driven model is depicted in Figure 7.8a.

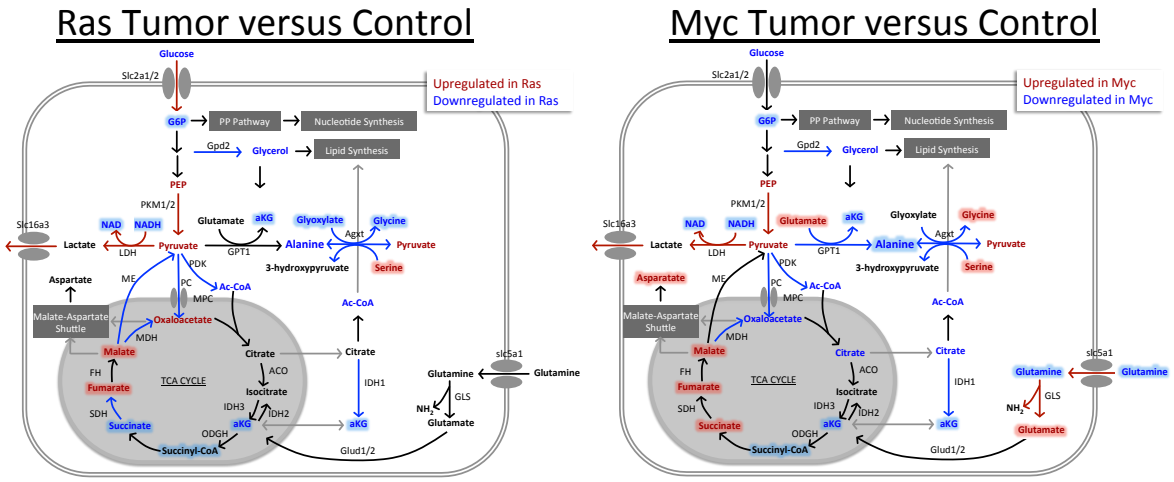

Figure 7.7: Comparison of Myc and Ras signaling pathways in oncogene-driven models of liver cancer found with Liquid Chromotography – Mass Spectrometry (LCMS) and mRNA expression. Red indicates upregulation compared to control and blue indicates down-regulation compared to control. Cloud indicates that metabolites is statistical different than control by LC-MS. Results suggests that the Ras model has a reduced reliance of glutamine as a fuel source compared to the Myc model. In the Ras model, pyruvate is not able to enter the TCA cycle as all of the genes associated with PC and PDK are down-regulated leaving more pyruvate available to be converted to alanine in a hyperpolarized experiment.

Further topological analysis of HCC relevant pathways are summarized in Figure 7.7. There are three important observations from this analysis, which support previous statements. First, the results suggest that the h-Ras model has a reduced reliance of glutamine as a fuel source compared to the c-Myc model. Secondly, the key difference associated with the observed conversion of HP pyruvate-to-alanine between the h-Ras model and the control is that pyruvate is not able to enter the TCA cycle in the Ras Model, where all of the genes associated with PC and PDK are downregulated leaving more pyruvate available to be converted to alanine in a hyperpolarized experiment. Thus, the h-Ras oncogene could be detected via its unique alternate signaling pathway signature.

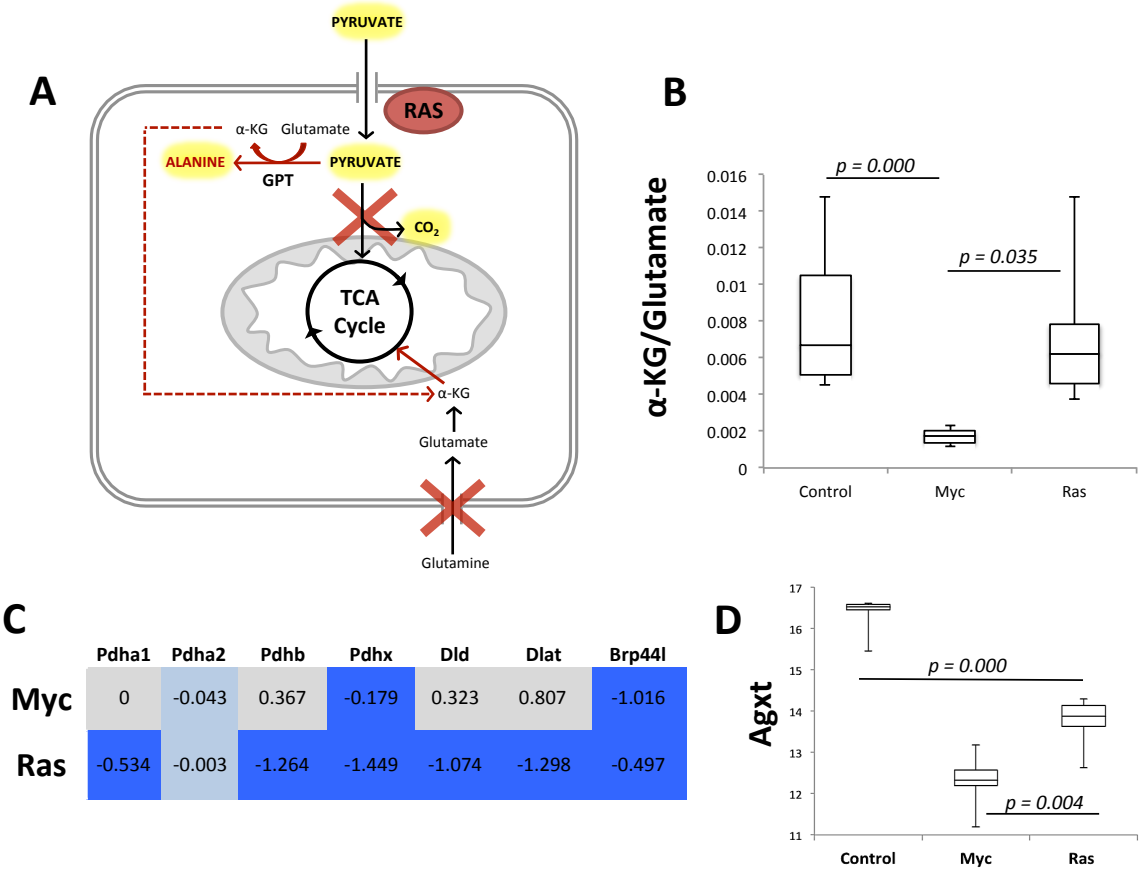

Figure 7.8: Summary of Ras driven model altered signaling pathway which favors conversion of pyruvate to alanine, whereby increased expression of Gpt-1/2 and Glud 1 coupled with **(c)** inhibition of pyruvate's entry into the TCA cycle increase conversion to alanine. **(d)** Moreover, decreased Agxt, an enzyme which converts pyruvate-to-alanine in peroxisomes, is decreased in both Myc and Ras tumors. **(b)** Meanwhile, increased conversion to alanine could be a result of altered utilization of the co-factors α-ketoglutarate (α-KG) and glutamate (p-value = 0.007). This maybe driven by reduced reliance on glutamine as a fuel source as compared to myc where the glutamine transport and glutamate production driven by Slc5a1 and Gls, respectively, are downregulated **(figure 7.6).**

7.5 Discussion & Conclusions

The HP carbon-13 MR detected conversion of pyruvate-to-alanine revealed metabolic differences between oncogene-induced signaling pathways. In the h-Ras driven liver cancer model, [1-^{13}C]-alanine remained high at progression indicative of an alternate utilization of the co-factors glutamate and α-ketoglutarate.

More generally, we show for the first time that HP MRSI can be used as metabolic imaging agent for non-invasive, *in vivo* monitoring of the presence of an oncogene, h-Ras. This is a novel application of HP MRSI to detect oncogene activation, which could be used to identify patients that would benefit most from a targeted therapy, to predict prognosis, for more robust image-guided biopsy, and to guide treatment decisions.

8. Automated Kinetic Modeling of Perfusion and Metabolism Based on Dynamic Hyperpolarized Carbon-13 Data With Open-Source SIVIC Software

Considerable attention has been dedicated to investigating the dynamics of real-time exchange of hyperpolarized signals to understand the underlying pathophysiology[23,24,29,85,106,157–165]. Derivation of kinetics of exchange from a HP substrate often requires a complex, multi-compartment model[76,84,166]. The results are prone to misinterpretation and can be model-dependent[76,166]. Moreover, as the technology moves into the clinic, there is a clear need for standardization, simplification of complicated workflows, and a format compatible with PACS. The present SIVIC open-source package processes and quantifies dynamic HP spectroscopic data in two simple steps. In the first step, the resonance of each metabolite is identified such that the program can produce a time-series of images for each measured metabolite. These dynamic images represent the time variation of the HP signals and are then processed to produce multiple parameters to fully describe the pathophysiology including quantification of dynamics, perfusion, and metabolic reaction rate kinetics. These can then be displayed readily in SIVIC, a free, open-source software package.

8.1 Background

Magnetic resonance spectroscopy (MRS) of HP substrates is a powerful tool for investigating tissue metabolism and kinetics *in vivo*[20,21,23,24]. In particular, HP [1-^{13}C]pyruvate is extremely valuable for the study of cancer because the conversion of pyruvate into lactate catalyzed via the lactate dehydrogenase (LDH) enzyme is highly

elevated in tumor cells[26,133]. Real-time exchange of HP [1-^{13}C]pyruvate to HP [1-^{13}C]lactate has shown great potential for the early diagnosis of tumor formation[22], response to therapy[23,157,158], and progression in preclinical models of cancer[19,21,85,157]. Following these promising preclinical studies, a pioneering first-in-man clinical trial using HP [1-^{13}C]pyruvate in prostate cancer patients was successfully completed[167]. Here we present a free, open-source implementation of kinetic and perfusion models for processing dynamic HP MRS data.

Considerable research effort has been dedicated to investigating the dynamics of real-time exchange of hyperpolarized signals to understand the underlining pathophysiology[15,75,76,166,168,169]. Derivation of reaction rate kinetics from a HP substrate often requires complex, multi-compartmental models to describe dynamic data requiring a complicated workflow[15,76]. The results are prone to misinterpretation and model-dependent. Moreover, as the technology moves into the clinic, there is a need for standardization, simplification of complicated work-flows, and delivery of data to PACS. The present open-source package processes and quantifies dynamic HP spectroscopic data in a two-step scheme, shown in Figure 8.1. First each metabolite is quantified at each time point to produce time series of maps. These dynamic images represent the time variation of the HP signals that are then processed to produce multiple parameters to fully describe the pathophysiology including quantification of dynamics, perfusion, and reaction rate kinetics. The resulting model parameters can be represented as 3D maps which can be exported as standard DICOM images.

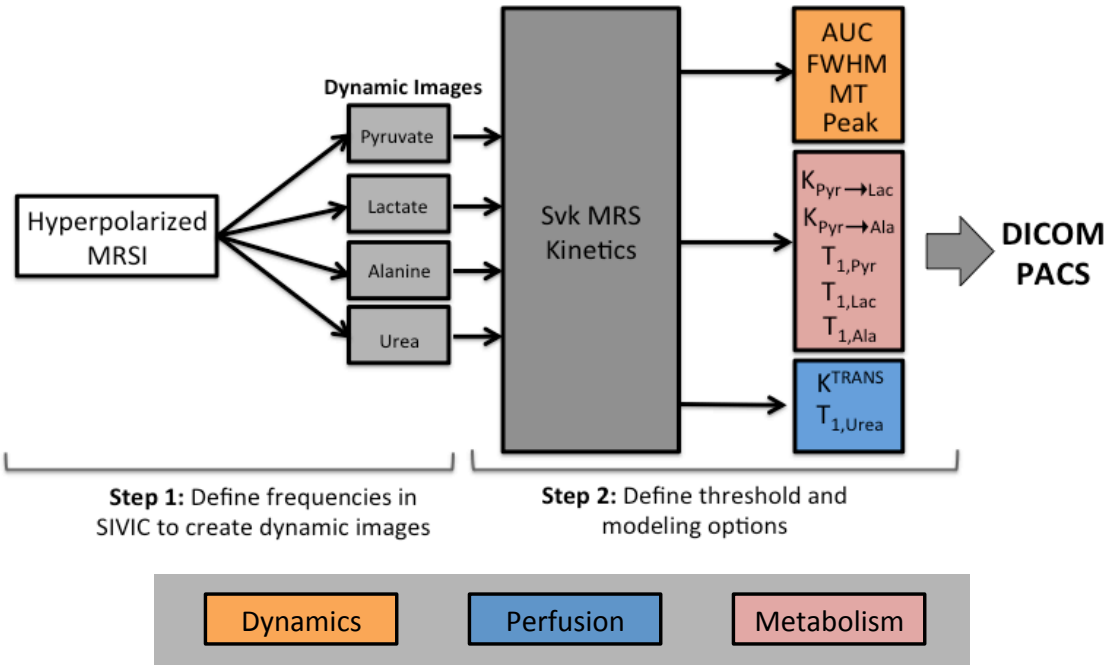

Figure 8.1: Two-step workflow for processing Hyperpolarized Spectroscopic data. First, spectral locations of metabolites are defined in the SIVIC GUI. Then the command line tool is used to generate maps of dynamics, perfusion, and metabolism.

8.2 Theory

8.2.1 Simplified Solver for Systems of Differential Equations

An equation of the form:

$$\frac{d}{dt}M(t) = \boldsymbol{K}M(t) \tag{8.1}$$

can be more simply described in the form

$$M(t) = \phi(t)M(t_0) \tag{8.2}$$

We define a matrix of exponential parameters, $\phi(t)$ using the Laplace transform.

$$\phi(t) = E^{\boldsymbol{K}t} = L^{-1}(s\boldsymbol{I} - \boldsymbol{K})^{-1} \tag{8.3}$$

Therefore any system of nonlinear differential equations of the form $\frac{d}{dt}M(t) = \boldsymbol{K}M(t)$ can be easily described with a simplified cost function. Using the symbolic toolbox in matlab, we can solve for our cost function simply (script available in appendix).

8.2.2 Metabolic Modeling

Hyperpolarized carbon-13 data can be described by the following system:

$$\begin{array}{ccc} Pyr & \underset{\leftarrow}{\xrightarrow{K_{Pyr\rightarrow Lac}}} & Lac \\ T_{1,Pyr}\downarrow & & \downarrow T_{1,Lac} \end{array}$$

Where $K_{Pyr\rightarrow Lac}$ describes the net flux of pyruvate to lactate during the mixing time. To reduce the number of parameters and provide for a better conditioned system[15], we assume that the backwards reaction, $K_{Lac\rightarrow Pyr}$, and pyruvate-to-alanine conversion, $K_{Pyr\rightarrow Ala}$, are negligible compared to the forward reaction. These assumptions are reasonable as $K_{Pyr\rightarrow Lac}$ reports on the net flux, $K_{Lac\rightarrow Pyr}$ is typically at least an order of magnitude lower than $K_{Pyr\rightarrow Lac}$ and $K_{Pyr\rightarrow Ala}$ is small outside of the liver.

The systems dynamics can be described by a simple two-site exchange model,

$$\frac{d}{dt}M(t) = \theta M(t) \tag{8.4}$$

where

$$M(t) = \begin{bmatrix} Pyr(t) \\ Lac(t) \end{bmatrix} \qquad \text{and} \qquad \theta = \begin{bmatrix} K_{Pyr\rightarrow Lac} \\ 1/T_{1,Pyr} \\ 1/T_{1,Lac} \end{bmatrix} \tag{8.5}$$

with the initial condition

$$\begin{bmatrix} Pyr(0) \\ Lac(0) \end{bmatrix} = \begin{bmatrix} Pyr(t_{Pyr\ Peak}) \\ Lac(t_{Pyr\ Peak}) \end{bmatrix} \tag{8.6}$$

In order to perform a linear least squares estimate of the parameters, Eqn. 8.4 can be rewritten in terms of the unknown parameters.

$$\frac{d}{dt}\begin{bmatrix} Pyr(0) \\ Lac(0) \end{bmatrix} = \begin{bmatrix} -Pyr(t) & -Pyr(t) & 0 \\ Pyr(t) & 0 & -Lac(t) \end{bmatrix} \begin{bmatrix} K_{Pyr\to Lac} \\ 1/T_{1,Pyr} \\ 1/T_{1,Lac} \end{bmatrix} \tag{8.7}$$

Such that for each measurement, we get an equation of the for,

$$B = A\theta \tag{8.8}$$

where

$$B = \frac{d}{dt}\begin{bmatrix} Pyr(t_1) \\ Lac(t_1) \\ \vdots \\ Pyr(t_n) \\ Lac(t_n) \end{bmatrix} \quad \text{and} \quad A = \begin{bmatrix} -Pyr(t_1) & -Pyr(t_1) & 0 \\ Pyr(t_1) & 0 & -Lac(t_1) \\ \vdots & \vdots & \vdots \\ -Pyr(t_n) & -Pyr(t_n) & 0 \\ Pyr(t_n) & 0 & -Lac(t_n) \end{bmatrix} \tag{8.9}.$$

The entries of B can be estimated using the following estimation:

$$\frac{d}{dt}b(t_i) = \frac{b(t_{i+1}) - b(t_{i-1})}{t_{i+1} - t_{i-1}} \tag{8.10}$$

And the parameter matrix, θ , can be found using a linear least squares fit, $\theta = B/A$. However, estimating three or more parameters with two curves can cause overfitting. Often it is assumed that $T_{1,Pyr} = T_{1,Lac}$ since they are in exchanging throughout the experiment. Applying this assumption can improve $K_{Pyr\to Lac}$ estimates which are indicative of the Warburg effect.

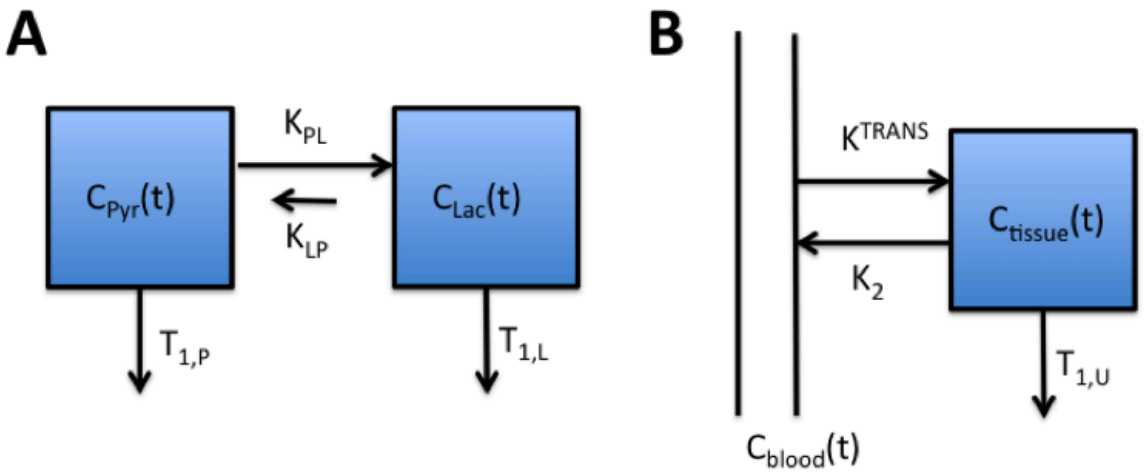

Figure 8.2: (a) Two-site exchange and **(b)** Perfusion kinetic models for hyperpolarized carbon-13 MR used in algorithm.

Alternatively, the kinetic model, $\frac{d}{dt}M(t) = \boldsymbol{K}M(t)$, can also be solved with a nonlinear least squares fit. The solution at each iteration is

$$min_x \|\boldsymbol{Js} - \boldsymbol{F}(\boldsymbol{x})\|_2^2 \tag{8.11}.$$

Thus solving for the approximate normal equations:

$$\boldsymbol{J^T Js} = -\boldsymbol{J^T F} \tag{8.12}.$$

The Jacobian matrix is defined as:

$$\boldsymbol{J}(\boldsymbol{x_k}) = \begin{bmatrix} \nabla F_1(x_k)^T \\ \nabla F_2(x_k)^T \\ \vdots \\ \nabla F_n(x_k)^T \end{bmatrix} \tag{8.13}.$$

Where the Jacobian is a vector based on the residuals, such that $\boldsymbol{F}(\boldsymbol{x}) = \frac{d}{dt}M(t) - \boldsymbol{K_i}M(t)$ a the ith iteration of the parameter combinations. Similarly to the linear least squares $\frac{d}{dt}M(t)$ can be approximated by

$$\frac{d}{dt}m(t_i) = \frac{m(t_{i+1}) - m(t_{i-1})}{t_{i+1} - t_{i-1}} \tag{8.14}.$$

The algorithm may converge slowly or not at all if the initial guess is far from the minimum

or if the matrix $\boldsymbol{J^T J}$ is ill-conditioned. In both linear and non-linear solving algorithms, without correction for the bolus arrival and perfusion the metabolic kinetic model must begin after the peak pyruvate signal and may have artifacts from perfusion.

8.2.3 Perfusion Modeling

Conventional (^{1}H, thermal) perfusion data can be modeled[170,171] according to a single-compartment model governed by the differential equation:

$$\frac{d}{dt}C_{tissue}(t) = EF\ C_{blood}(t) - \frac{EF}{V_T}C_{tissue}(t) \qquad (8.15).$$

Where $C_{tissue}(t)$ is the tracer concentration in tissue (MR signal/mL) and $C_{blood}(t)$ is the arterial input function (MR signal/mL), while F is the tissue perfusion (mL/mL/s), E is the extraction fraction of each agent (unitless), and V_T is the distribution volume of each agent (mL/mL). Perfusion curves can be fit by join nonlinear least squares to its solution,

$$C_{tissue}(t) = (1 - v_b)EF\ exp\left(-\frac{EF}{V_T}\right) \otimes C_{blood}(t) + v_b C_{blood}(t) \qquad (8.16)$$

which includes the blood volume v_b (mL/mL). The extraction fraction, E, can be modeled as a function of the vessel permeability surface (PS) product (mL/mL/s), by $E = PS/(PS + F)$. The gamma-variate arterial input function known to approximate the arterial concentration curve for the injection procedure can be described by:

$$C_{blood}(t \geq 0) = A_o(t - t_o)^{\alpha}\exp\left(-\frac{t-t_o}{\beta}\right) \qquad (8.17).$$

This is typically measure in a major artery.

Alternatively, Eqn. 8.15 can be described by the following simplified model, which accounts for the non-renewable T_1 signal decay of a hyperpolarized substrate:

$$\frac{d}{dt}C_{tissue}(t) = -K_{TRANS}C_{blood}(t) - k_2 C_{tissue}(t) \qquad (8.18).$$

Where K_{TRANS} describes the perfusion in both vascularity and leakiness of the vesels and

k_2 is a combination of T_1 relaxation and the uptake of the tracer back into the vasculature, k_{ep}[112,113,168].

8.2.4 Combined Metabolic and Perfusion Modeling

Eqn. 8.18, which describes perfusion that is of, is now in the form Eqn. 8.1, which can be used in the symbolic solver and then implemented in the command-line tool. Moreover, this can be combined with Eqn. 8.4, which describes metabolism to get the following:

$$\frac{d}{dt}\vec{M}(t) = \boldsymbol{K}_{met}\vec{M}(t) + \boldsymbol{K}_{perf}F(t) \quad (8.19).$$

Where $\vec{M}(t)$ is a matrix containing the dynamic metabolic data of size $m \times t$, metabolites × time. $\boldsymbol{K}_{met}$ is a matrix of parameters that describes metabolism and $\boldsymbol{K}_{perf}$ describes the perfusion of the input function into the tissue pyruvate pool. $F(t)$ is an input function which can be measured arterial input function, simulated based on the total carbon signal, or the urea signal in the voxel. Eqn. 8.19 describes the model shown in Figure 8.3.

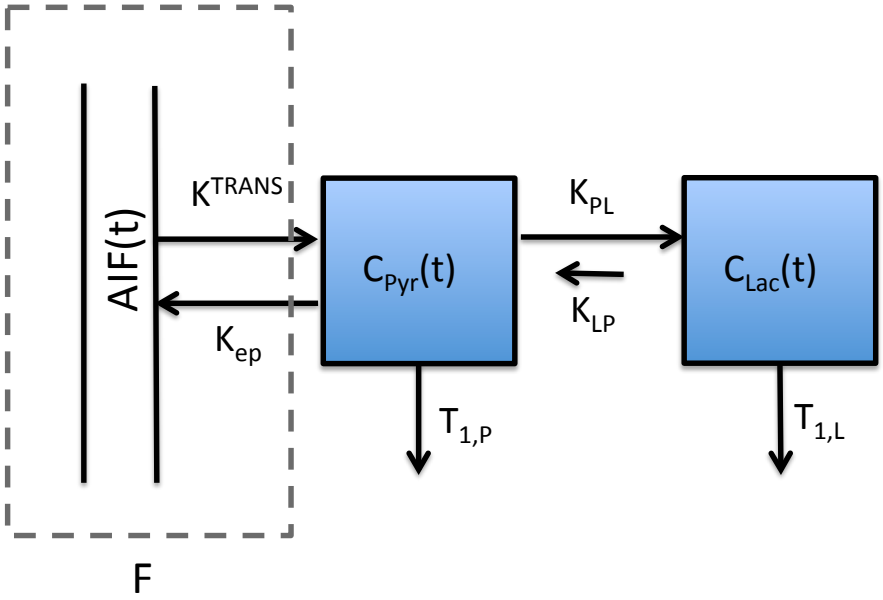

Figure 8.3: Combined perfusion and metabolism kinetic models for hyperpolarized carbon-13 MR.

If urea is used as the input function, K^{trans} no longer describes the movement of the tracer from the major vasculature to the tissue but instead describes the movement of pyruvate

into cells. Designing the model for the Phase 1 clinical trial data, the total carbon signal was used to simulate an arterial input function as there was no measured arterial input and HP ^{13}C-urea is not yet approved for human use, although urea has been show to be very safe even at high doses. Therefore , $\vec{M}(t) = \begin{bmatrix} P(t) \\ L(t) \end{bmatrix}$ and the parameter matrices are

$$\boldsymbol{K}_{met} = \begin{bmatrix} -K_{PL} - 1/T_{1,P} & 0 \\ K_{PL} & -1/T_{1,L} \end{bmatrix} \quad \text{and} \quad \boldsymbol{K}_{perf} = \begin{bmatrix} K^{trans} \\ 0 \end{bmatrix} \quad (8.20).$$

8.3 Implementation

The three kinetic models were implemented in C++ in the open-source SIVIC package. The models were tested for accuracy and sensitivity to noise in matlab. The source code, as well as a command line tool (svk_mrs_kinetics) and GUI (SIVIC) application are freely available for download. The SIVIC package reads several vendors MRS data formats and can also read, visualize and fit dynamic metabolite maps encoded as DICOM MR Image Storage SOP instances. The SIVIC C++ class (svkMRSKinetics) can easily be extended to support other kinetic models.

For flexibility, particle swarm optimization (PSO) was used. PSO uses population-based approach that finds a solution to an optimization problem in a search space. PSO allows for non-linearity making it more adaptable to any model. Additionally, PSO allows for upper and lower bounds constraints preventing physiologically impossible parameter estimates that may result in a local minimum. As with many other solvers, it minimizes the residual and thus makes no assumptions about the model (Figure 8.4).

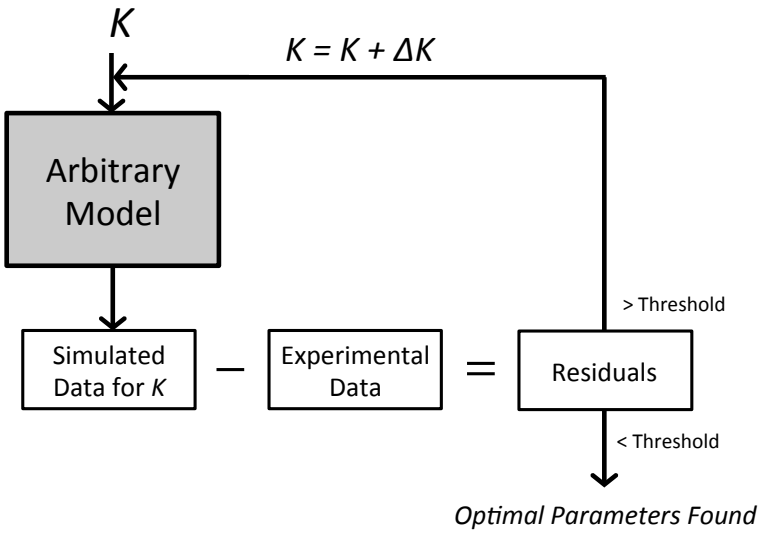

Figure 8.4: Optimization algorithm flow. The optimization does not utilize a jacobian and does not require linearity of the model. Therefore it is independent of input model allowing for flexibility.

8.4 Results

The processing procedure is shown in Figure 8.5. MRSI data is converted to dynamic metabolic images in the SIVIC GUI (Figure 8.5a). Then (Figure 8.5b) the algorithm produces maps of parameters describing the dynamics and (Figure 8.5c) maps of metabolic and perfusion kinetic parameters are produced all within a single step. Kinetic models were validated in matlab (Figure 8.5c).

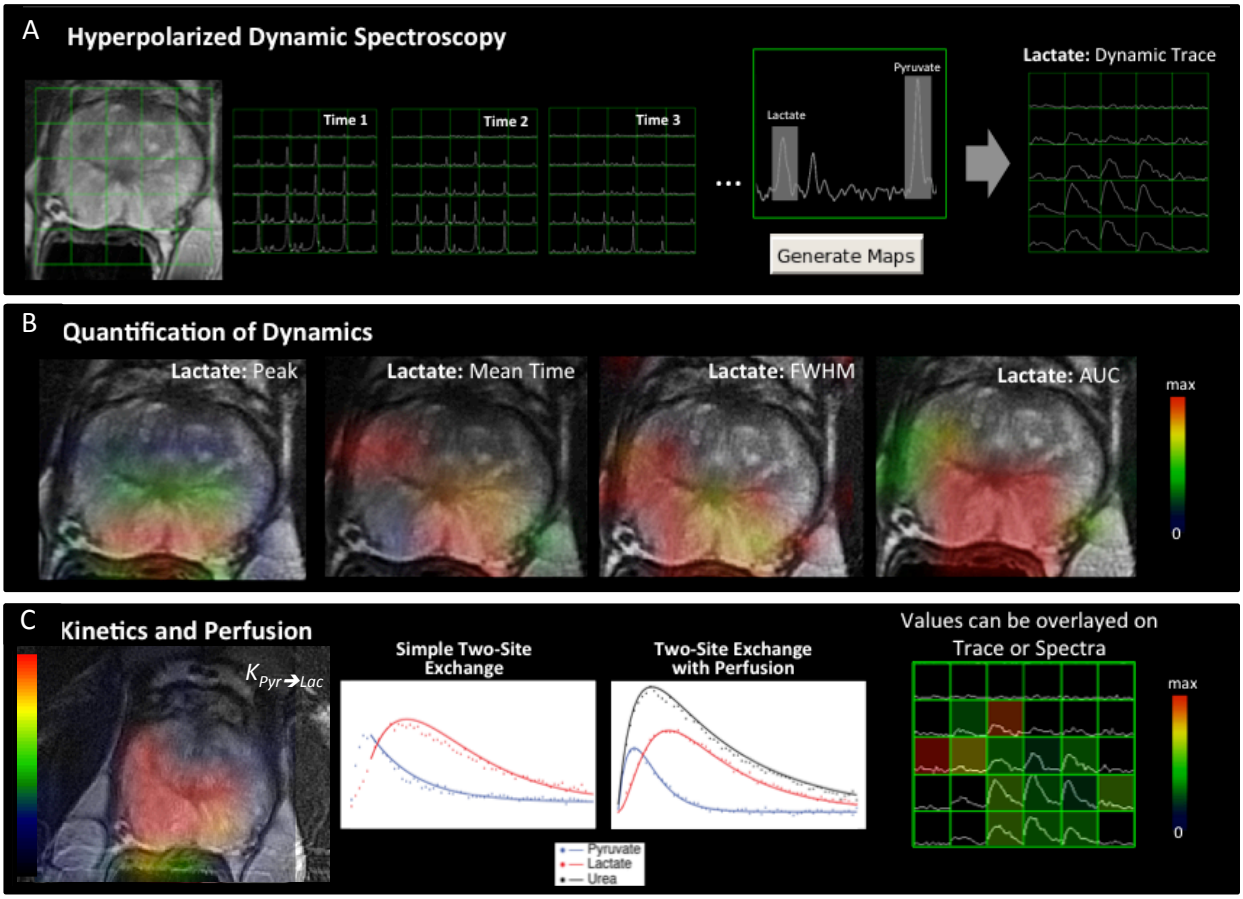

Figure 8.5: Output from processing of dynamic MR spectroscopic imaging from Phase I clinical trial. **(a)** MRSI data is converted to dynamic metabolic images. Then **(b)** maps of parameters describing the dynamics are produced and **(c)** maps of metabolic and perfusion kinetic parameters are produced all within a single step.

The sample kinetic maps from the combined model are shown in Figure 8.6. Fitted traces can be displayed with experimental data for validation and to prevent false positives from modeling errors.

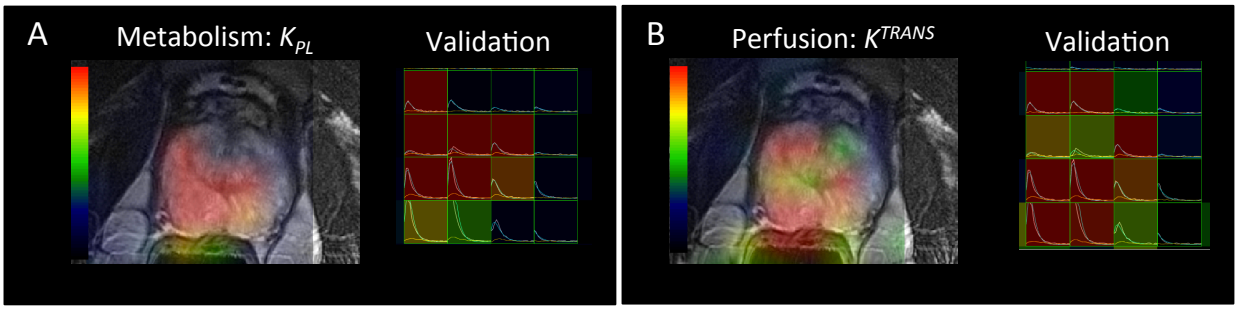

Figure 8.1: Sample maps from processing of dynamic MR spectroscopic imaging from Phase I clinical trial with combined **(a)** metabolism and **(b)** perfusion kinetic model. Dynamic traces with fitted curves are shown which estimate value for each voxel. This display allows the user to debug the model and aids preventing false positives.

8.5 Discussion & Conclusions

Within a single step, dynamic volumetric images are masked to total carbon (tCar) signal-to-noise (SNR) above an input threshold. Then, the algorithm creates volumetric maps quantifying the dynamics, which includes the maximum signal (Peak), area under the curve (AUC), full width half max (FWHM), and mean time (MT) for each metabolite, which provides information on uptake, perfusion, retention, and vascularization. It then produces maps of the metabolic kinetics (Figure 8.4a) which includes the rate of conversion of pyruvate-to-lactate ($K_{Pyr\rightarrow Lac}$), but can be extended to include pyruvate-to-alanine conversion ($K_{Pyr\rightarrow Ala}$) or lactate-to-pyruvate conversion ($K_{Lac\rightarrow Pyr}$), as well as maps of the longitudinal relaxation of pyruvate ($T_{1,Pyr}$), lactate ($T_{1,Lac}$), alanine ($T_{1,Ala}$), and urea ($T_{1,Urea}$). Finally, with a reference voxel, perfusion maps (Figure 4b) can be produced including the transport rate constant from blood to tissue (K_{TRANS}), and can be extended to include the rate constant between extracellular extravascular space (k_2).

The two-step workflow for processing data is shown in Figure 8.2. Whereby dynamic spectra can be easily converted to dynamic images and displayed with anatomical images. Dynamic images can then be processed with a single command line tool to produce multiple parametric maps. Parametric maps can be displayed simultaneously with spectra, dynamics, and anatomical images. The produced maps describe many aspects of pathophysiology including quantification of uptake, perfusion, flow, and reaction rate kinetics.

For the initial demonstration, we implement three kinetic models (1) a two-site exchange

model of metabolism (2) a perfusion model and a (3) new combined perfusion and metabolism model. These were implemented on this platform that is easily extended to other models and is freely available. A key motivation for this work is standardization Because consensus has not been made on what is the best model and acquisition strategy, flexibility is still needed. However, once standardized protocols are accepted in the field, this tool will allow such a model to be widely accessible and easily to implemented across sites. The tool presented here also addresses the need for simplification of complicated workflows, and delivery of data to PACS, both necessary as this technique moves into the clinic.

9. Summary

This dissertation presents several contributions to the new and growing field of hyperpolarized carbon-13 magnetic resonance, a subset of magnetic resonance imaging. This work shows both developments in acquisition and reconstruction MR methods as well as the application of this new technology to study biological alterations in cancer.

Chapter 3 focuses on the application of metabolic activity decomposition (MAD) with stimulated echo acquisition mode (STEAM) to kinetic modeling of hyperpolarized substrates. Because MAD-STEAM allows for direct detection of exchange it provides twice the information and thus provides much more accurate quantitative markers of cancer metabolism. Chapter 4 presents an extension of the MAD technique, which allowed for visualization of the distribution enzymatic activity. Moreover, this localization allowed for the validation of the technique to be able to accurately detect changes in enzymatic activity *in vivo.* Chapter 5 built upon the foundations made in Chapter 3 with the addition of variable diffusion weighting. The addition of varied diffusion weighting allowed for the possibility to acquire exchange, relaxation and diffusion parameters within a single acquisition. In Chapter 6, MAD is adapted to rapidly acquire 2D NMR EXchange SpectroscopY (EXSY) spectra of hyperpolarized substrates. The preliminary results highlight the importance of investigating bidirectional exchange in the study of metabolism as well as show its potential to be used as a diagnostic tool. The technique has broad applications including other substrates and other pathways that may be altered due to the presence of disease and even other nuclei.

The research presented in Chapter 7 demonstrated that metabolic reprogramming can be used to detect and differentiate oncogene activation in liver cancer. This is a novel application of HP MRSI to detect oncogene activation, which could be used to identify patients that would benefit most from a targeted therapy, to predict prognosis, for more robust image-guided biopsy, and to guide treatment decisions. Finally in Chapter 8, kinetic modeling algorithms for a single command line tool were developed to aid in the interpretation and visualization of hyperpolarized signals, to facilitate translation and multisite clinical trials of hyperpolarized technology.

Hyperpolarized Carbon-13 MR has many advantages, including high SNR metabolic imaging, use of safe agents with out the risk of ionizing radiation and without the toxicity associated with other contrast agents, high specificity due to the lack of background signals, and speed. Future work could be focused on other agents, although this this work. For instance, flux of α-ketoglutarate to its products is associated with a number of important in cancer metabolism pathways such as reductive carboxylation, IDH mutations, glutamine addiction, lipogenesis, and Ras expression as shown in Chapter 7. The directionality of its exchange could both provide insights on how cancer cells metabolize fuel sources with a dysfunctional mitochondrial as well as be used a diagnostic tool marker of cancer metabolism. Moreover, the study of how exchange and flux is affected in different cancer types, grades, after treatment, and even other diseases is certainly a major research focus in the future. Finally the optimization of pulse sequences to gain improved resolution, speed, SNR, and spatial coverage would greatly strengthen the advantages of using metabolic activity decomposition, which we have shown is a very powerful technique.

In summary, hyperpolarized carbon-13 is a rich, emerging field with great biomedical research and clinical potential. Already, the technology has been translated into the clinic with the first-in-man clinical trial, which showed both safety and efficacy. Moreover, both the breadth and depth of preclinical studies have demonstrated the power of this technology to aid in understanding of disease as well as its clinical potential. This dissertation presents a small contribution to this paradigm-shifting field.

References

1. Haacke, M., Brown, R., Thompson, M. & Venkatesan, R. *Magnetic Resonance Imaging: Physical Principles And Sequence Design*. (Wiley-Liss, 1999).
2. Levitt, M. *Spin Dynamics: Basics of Nuclear Magnetic Resonance*. (John Wiley & Sons Ltd, 2001).
3. Nishimura, D. *Principles of Magnetic Resonance Imaging*. (1996).
4. Ardenkjaer-Larsen, J. H. *et al.* Increase in signal-to-noise ratio of > 10,000 times in liquid-state NMR. *Proc. Natl. Acad. Sci. U. S. A.* **100,** 10158–10163 (2003).
5. Bloch, F. Nuclear Induction. *Phys. Rev.* **70,** 460–474 (1946).
6. Hu, S. Hyperpolarized 13C Magnetic Resonance Spectroscopic Imaging: Pulse Sequence Development for Compressed Sensing Rapid Imaging and Preclinical Liver Studies. (2009).
7. Sholl, C. A BPP (Bloembergen-Purcell-Pound) model for nuclear spin relaxation due to diffusion in disordered systems: combined barrier- and site-energy disorder. *J Phys: Condens Matter* **12,** 4385 (2000).
8. McConnell, H. M. Reaction Rates by Nuclear Magnetic Resonance. *J. Chem. Phys.* **28,** 430–431 (1958).
9. Abergel, D. & Palmer, A. G. Approximate solutions of the Bloch-McConnell equations for two-site chemical exchange. *Chem. Phys. Chem.* **5,** 787–793 (2004).
10. Bracewell, R. *The Fourier Transform and Its Applications*. (McGraw-Hill, 2000).
11. Vallurupalli, P. Chemical Exchange. Lecture: TIFR Mumbai (2009).
12. Bain, A. D. Chemical exchange in NMR. *Prog. Nucl. Magn. Reson. Spectrosc.* **43,** 63–103 (2003).

13. Aue, W. P., Bartholdi, E. & Ernst, R. R. Two-dimensional spectroscopy. Application to nuclear magnetic resonance. *J. Chem. Phys.* **64,** 2229–2246 (1976).
14. Larson, P. E. Z., Kerr, A. B., Swisher, C. L., Pauly, J. M. & Vigneron, D. B. A rapid method for direct detection of metabolic conversion and magnetization exchange with application to hyperpolarized substrates. *J. Magn. Reson.* **225,** (2012).
15. Swisher, C. L. *et al.* Quantitative measurement of cancer metabolism using stimulated echo hyperpolarized carbon-13 MRS. *Magn. Reson. Med.* **71,** (2014).
16. Torrey, H. C. Bloch Equations with Diffusion Terms. *Phys Rev* **104,** 563–565 (1956).
17. Bernstein, M., King, K. & Zhou, X. *Handbook of MRI Pulse Sequences*. (Elsevier Academic Press, 2004).
18. Park, I. *et al.* Detection of early response to temozolomide treatment in brain tumors using hyperpolarized 13C MR metabolic imaging. *J. Magn. Reson. Imaging* **33,** 1284–1290 (2011).
19. Chaumeil, M. M. *et al.* Non-invasive in vivo assessment of IDH1 mutational status in glioma. *Nat. Commun.* **4,** (2013).
20. Nelson, S. J. *et al.* Metabolic imaging of patients with prostate cancer using hyperpolarized [1-(13)C]pyruvate. *Sci. Transl. Med.* **5,** (2013).
21. Kurhanewicz, J. *et al.* Analysis of cancer metabolism by imaging hyperpolarized nuclei: prospects for translation to clinical research. *Neoplasia N. Y. N* **13,** (2011).
22. Hu, S. *et al.* 13C-pyruvate imaging reveals alterations in glycolysis that precede c-Myc-induced tumor formation and regression. *Cell Metab.* **14,** 131–142 (2011).
23. Day, S. E. *et al.* Detecting tumor response to treatment using hyperpolarized 13C magnetic resonance imaging and spectroscopy. *Nat. Med.* **13,** 1382–1387 (2007).

24. Golman, K., Zandt, R. I., Lerche, M., Pehrson, R. & Ardenkjaer-Larsen, J. H. Metabolic imaging by hyperpolarized 13C magnetic resonance imaging for in vivo tumor diagnosis. *Cancer Res.* **66,** 10855–10860 (2006).
25. Olenchock, B. A. & Vander Heiden, M. G. Pyruvate as a pivot point for oncogene-induced senescence. *Cell* **153,** 1429–1430 (2013).
26. WARBURG, O. On the origin of cancer cells. *Science* **123,** 309–314 (1956).
27. Schroeder, M. A., Clarke, K., Neubauer, S. & Tyler, D. J. Hyperpolarized magnetic resonance: a novel technique for the in vivo assessment of cardiovascular disease. *Circulation* **124,** 1580–1594 (2011).
28. Merritt, M. E., Harrison, C., Sherry, A. D., Malloy, C. R. & Burgess, S. C. Flux through hepatic pyruvate carboxylase and phosphoenolpyruvate carboxykinase detected by hyperpolarized 13C magnetic resonance. *Proc. Natl. Acad. Sci.* **108,** 19084–19089 (2011).
29. Chaumeil, M. M. *et al.* Hyperpolarized 13C MR spectroscopic imaging can be used to monitor Everolimus treatment in vivo in an orthotopic rodent model of glioblastoma. *NeuroImage* **59,** (2012).
30. MacKenzie, J. D. *et al.* Detection of inflammatory arthritis by using hyperpolarized 13C-pyruvate with MR imaging and spectroscopy. *Radiology* **259,** 414–420 (2011).
31. Laustsen, C. *et al.* Assessment of early diabetic renal changes with hyperpolarized [1-(13) C]pyruvate. *Diabetes Metab. Res. Rev.* **29,** 125–129 (2013).
32. Ward, P. S. & Thompson, C. B. Metabolic reprogramming: a cancer hallmark even warburg did not anticipate. *Cancer Cell* **21,** (2012).

33. Kalinina, J. *et al.* Detection of 'oncometabolite' 2-hydroxyglutarate by magnetic resonance analysis as a biomarker of IDH1/2 mutations in glioma. *J. Mol. Med.* **90,** 1161–1171 (2012).
34. Ward, P. S. *et al.* Identification of additional IDH mutations associated with oncometabolite R(-)-2-hydroxyglutarate production. *Oncogene* **31,** 2491–2498 (2012).
35. Bardella, C. *et al.* Aberrant succination of proteins in fumarate hydratase-deficient mice and HLRCC patients is a robust biomarker of mutation status. *J. Pathol.* **225,** (2011).
36. Sullivan, L. B. *et al.* The proto-oncometabolite fumarate binds glutathione to amplify ROS-dependent signaling. *Mol. Cell* **51,** 236–248 (2013).
37. Yang, M., Soga, T., Pollard, P. J. & Adam, J. The emerging role of fumarate as an oncometabolite. *Front. Oncol.* **2,** (2012).
38. Lopez-Lazaro, M. The warburg effect: why and how do cancer cells activate glycolysis in the presence of oxygen? *Anticancer Agents Med. Chem.* **8,** 305–312 (2008).
39. Ponisovskiy, M. R. Cancer metabolism and the Warburg effect as anabolic process outcomes of oncogene operation. *Crit. Rev. Eukaryot. Gene Expr.* **20,** 325–339 (2010).
40. DeBerardinis, R. J. & Cheng, T. Q's next: the diverse functions of glutamine in metabolism, cell biology and cancer. *Oncogene* **29,** 313–324 (2010).
41. Croce, C. M. Oncogenes and Cancer. *N. Engl. J. Med.* **358,** 502–511 (2008).
42. The Nobel Prize in Physiology or Medicine 1989 to J. Michael Bishop and Harold E. Varmus for their discovery of 'The cellular origin of retroviral oncogenes'.
43. Weinberg, R. *The Biology of Cancer*. (Garland Science, 2013).
44. Barillot, E., Calzone, L., Hupe, P., Vert, J. & Zinovyev, A. *Computational Systems Biology of Cancer*. (CRC Press, 2012).
45. Hilgenfeld, R. Regulatory GTPases. *Curr. Opin. Struct. Biol.* **5,** 810–817 (1995).

46. Mendez-Sanchez, N., Vasquez-Fernandez, F., Zamora-Valdes, D. & Uribe, M. Sorafenib, a systemic therapy for hepatocellular carcinoma. *Ann. Hepatol.* **7,** (2008).

47. Sorafenib (Nexavar) for thyroid cancer. *Med. Lett. Drugs Ther.* **56,** 43–44 (2014).

48. Escudier, B. *et al.* Sorafenib in advanced clear-cell renal-cell carcinoma. *N. Engl. J. Med.* **356,** 125–134 (2007).

49. Felsher, D. W. & Bishop, J. M. Reversible tumorigenesis by MYC in hematopoietic lineages. *Mol. Cell* **4,** (1999).

50. Dang, C. V. MYC, microRNAs and glutamine addiction in cancers. *Cell Cycle* **8,** 3243–3245 (2009).

51. Goga, A., Yang, D., Tward, A. D., Morgan, D. O. & Bishop, J. M. Inhibition of CDK1 as a potential therapy for tumors over-expressing MYC. *Nat. Med.* **13,** 820–827 (2007).

52. Briggs, G. E. & Haldane, J. B. A Note on the Kinetics of Enzyme Action. *Biochem. J.* **19,** 338–339 (1925).

53. Johnson, K. A. & Goody, R. S. The Original Michaelis Constant: Translation of the 1913 Michaelis–Menten Paper. *Biochemistry (Mosc.)* **50,** 8264–8269 (2011).

54. Mathews, C., van Holde, K. & Ahern, K. *Biochemistry*. (Prentice Hall, 1999).

55. Oliver, J. A., el-Hilali, M. M., Belitsky, P. & MacKinnon, K. J. LDH isoenzymes in benign and malignant prostate tissue. The LDH V-I ratio as an index of malignancy. *Cancer* **25,** 863–866 (1970).

56. Koukourakis, M. I. *et al.* Lactate dehydrogenase-5 (LDH-5) overexpression in non-small-cell lung cancer tissues is linked to tumour hypoxia, angiogenic factor production and poor prognosis. *Br. J. Cancer* **89,** 877–885 (2003).

57. Tesch, P., Sjodin, B., Thorstensson, A. & Karlsson, J. Muscle fatigue and its relation to lactate accumulation and LDH activity in man. *Acta Physiol. Scand.* **103,** 413–420 (1978).

58. Hamosh, A., Scott, A. F., Amberger, J. S., Bocchini, C. A. & McKusick, V. A. Online Mendelian Inheritance in Man (OMIM), a knowledgebase of human genes and genetic disorders. *Nucleic Acids Res.* **33,** D514–517 (2005).

59. Brooks, G. A. Cell-cell and intracellular lactate shuttles. *J. Physiol.* **587,** 5591–5600 (2009).

60. Brooks, G. A. Lactate shuttles in nature. *Biochem. Soc. Trans.* **30,** 258–264 (2002).

61. Draoui, N. & Feron, O. Lactate shuttles at a glance: from physiological paradigms to anti-cancer treatments. *Dis. Model. Mech.* **4,** 727–732 (2011).

62. Dimmer, K. S., Friedrich, B., Lang, F., Deitmer, J. W. & Broer, S. The low-affinity monocarboxylate transporter MCT4 is adapted to the export of lactate in highly glycolytic cells. *Biochem. J.* **350 Pt 1,** 219–227 (2000).

63. Halestrap, A. P. The monocarboxylate transporter family - Structure and functional characterization. *IUBMB Life* **64,** (2012).

64. Halestrap, A. P. The SLC16 gene family - structure, role and regulation in health and disease. *Mol. Aspects Med.* **34,** 337–349 (2013).

65. Lin, R. Y., Vera, J. C., Chaganti, R. S. & Golde, D. W. Human monocarboxylate transporter 2 (MCT2) is a high affinity pyruvate transporter. *J. Biol. Chem.* **273,** 28959–28965 (1998).

66. Cheng, C. *et al.* Alterations of monocarboxylate transporter densities during hypoxia in brain and breast tumour cells. *Cell. Oncol. (Dordr).* **35,** 217–227 (2012).

67. Rosafio, K. & Pellerin, L. Oxygen tension controls the expression of the monocarboxylate transporter MCT4 in cultured mouse cortical astrocytes via a hypoxia-inducible factor-1alpha-mediated transcriptional regulation. *Glia* **62,** 477–490 (2014).

68. Gotanda, Y. *et al.* Expression of monocarboxylate transporter (MCT)-4 in colorectal cancer and its role: MCT4 contributes to the growth of colorectal cancer with vascular endothelial growth factor. *Anticancer Res.* **33,** 2941–2947 (2013).

69. Keshari, K. R. *et al.* Hyperpolarized 13C-pyruvate magnetic resonance reveals rapid lactate export in metastatic renal cell carcinomas. *Cancer Res.* **73,** 529–538 (2013).

70. Witkiewicz, A. K. *et al.* Using the 'reverse Warburg effect' to identify high-risk breast cancer patients: stromal MCT4 predicts poor clinical outcome in triple-negative breast cancers. *Cell Cycle* **11,** 1108–1117 (2012).

71. Doherty, J. R. & Cleveland, J. L. Targeting lactate metabolism for cancer therapeutics. *J. Clin. Invest.* **123,** 3685–3692 (2013).

72. Zhao, Y., Butler, E. B. & Tan, M. Targeting cellular metabolism to improve cancer therapeutics. *Cell Death Dis.* **4,** (2013).

73. Merritt, M. E. *et al.* Hyperpolarized 13C allows a direct measure of flux through a single enzyme-catalyzed step by NMR. *Proc. Natl. Acad. Sci.* **104,** 19773–19777 (2007).

74. Harrison, C. *et al.* Comparison of kinetic models for analysis of pyruvate-to-lactate exchange by hyperpolarized 13 C NMR. *NMR Biomed.* **25,** 1286–1294 (2012).

75. Larson, P. E. Z. *et al.* Investigation of tumor hyperpolarized [1-13C]-pyruvate dynamics using time-resolved multiband RF excitation echo-planar MRSI. *Magn. Reson. Med.* **63,** 582–591 (2010).

76. Harris, T., Eliyahu, G., Frydman, L. & Degani, H. Kinetics of hyperpolarized 13C1-pyruvate transport and metabolism in living human breast cancer cells. *Proc. Natl. Acad. Sci.* **106,** 18131–18136 (2009).

77. Zierhut, M. L. *et al.* Kinetic modeling of hyperpolarized 13C1-pyruvate metabolism in normal rats and TRAMP mice. *J. Magn. Reson.* **202,** (2010).

78. Zeng, H., Lee, Y. & Hilty, C. Quantitative Rate Determination by Dynamic Nuclear Polarization Enhanced NMR of a Diels–Alder Reaction. *Anal. Chem.* **82,** 8897–8902 (2010).

79. Kettunen, M. I. *et al.* Magnetization transfer measurements of exchange between hyperpolarized [1-13C]pyruvate and [1-13C]lactate in a murine lymphoma. *Magn. Reson. Med.* **63,** 872–880 (2010).

80. Schulte, R. F. *et al.* Saturation-recovery metabolic-exchange rate imaging with hyperpolarized [1-13C] pyruvate using spectral-spatial excitation. *Magn. Reson. Med.* **69,** 1209–1216 (2013).

81. Witney, T. H., Kettunen, M. I. & Brindle, K. M. Kinetic modeling of hyperpolarized 13C label exchange between pyruvate and lactate in tumor cells. *J. Biol. Chem.* **286,** 24572–24580 (2011).

82. Chen, A. P., Hurd, R. E. & Cunningham, C. H. Spin tagging for hyperpolarized (1)(3)C metabolic studies. *J. Magn. Reson.* **214,** 319–323 (2012).

83. Larson, P. E. Z. *et al.* Generating super stimulated-echoes in MRI and their application to hyperpolarized. *IEEE Trans. Med. Imaging* **31,** 265–275 (2012).

84. Santarelli, M. F. *et al.* How the signal-to-noise ratio influences hyperpolarized 13C dynamic MRS data fitting and parameter estimation. *NMR Biomed.* **25,** 925–934 (2012).

85. Albers, M. J. *et al.* Hyperpolarized 13C lactate, pyruvate, and alanine: noninvasive biomarkers for prostate cancer detection and grading. *Cancer Res.* **68,** 8607–8615 (2008).

86. Dafni, H. *et al.* Hyperpolarized 13C spectroscopic imaging informs on hypoxia-inducible factor-1 and myc activity downstream of platelet-derived growth factor receptor. *Cancer Res.* **70,** 7400–7410 (2010).

87. Wise, D. R. & Thompson, C. B. Glutamine addiction: a new therapeutic target in cancer. *Trends Biochem. Sci.* **35,** 427–433 (2010).

88. Zeng, H., Bowen, S. & Hilty, C. Sequentially acquired two-dimensional NMR spectra from hyperpolarized sample. *J. Magn. Reson.* **199,** 159–165 (2009).

89. Frydman, L. & Blazina, D. Ultrafast two-dimensional nuclear magnetic resonance spectroscopy of hyperpolarized solutions. *Nat Phys* **3,** 415–419 (2007).

90. Brotin, T., Devic, T., Lesage, A., Emsley, L. & Collet, A. Synthesis of deuterium-labeled cryptophane-A and investigation of Xe@cryptophane complexation dynamics by 1D-EXSY-NMR experiments. *Chem.* **7,** 1561–1573 (2001).

91. Jeener, J., Meier, B., Bachmann, P. & Ernst, R. Investigation of exchange processes by two-dimensional NMR spectroscopy. *J Chem Phys* (1979).

92. Larson, P. E. Z. *et al.* Perfusion and diffusion sensitive 13C stimulated-echo MRSI for metabolic imaging of cancer. *Magn. Reson. Imaging* **31,** 635–642 (2013).

93. Park, T. & Haug, E. J. Ill-Conditioned equations in kinematics and dynamics of machines. *Int. J. Numer. Methods Eng.* **26,** 217–230 (1988).

94. Rivals, I. & Personnaz, L. Jacobian conditioning analysis for model validation. *Neural Comput.* **16,** 401–418 (2004).

95. Wilson, D. M. *et al.* Multi-compound polarization by DNP allows simultaneous assessment of multiple enzymatic activities in vivo. *J. Magn. Reson.* **205,** 141–147 (2010).

96. Cunningham, C. H. *et al.* Double spin-echo sequence for rapid spectroscopic imaging of hyperpolarized 13C. *J. Magn. Reson.* **187,** 357–362 (2007).

97. Derby, K., Tropp, J. & Hawryszko, C. Design and evaluation of a novel dual-tuned resonator for spectroscopic imaging. *J. Magn. Reson. 1969* **86,** 645–651 (1990).

98. Shachaf, C. M. *et al.* MYC inactivation uncovers pluripotent differentiation and tumour dormancy in hepatocellular cancer. *Nature* **431,** 1112–1117 (2004).

99. Chin, L. *et al.* Essential role for oncogenic Ras in tumour maintenance. *Nature* **400,** 468–472 (1999).

100. Spiess, A.-N. & Neumeyer, N. An evaluation of R2 as an inadequate measure for nonlinear models in pharmacological and biochemical research: a Monte Carlo approach. *BMC Pharmacol.* **10,** (2010).

101. Dang, C. V. & Semenza, G. L. Oncogenic alterations of metabolism. *Trends Biochem. Sci.* **24,** (1999).

102. Vander Heiden, M. G. Exploiting tumor metabolism: challenges for clinical translation. *J. Clin. Invest.* **123,** 3648–3651 (2013).

103. Curry, J. M. *et al.* Cancer metabolism, stemness and tumor recurrence: MCT1 and MCT4 are functional biomarkers of metabolic symbiosis in head and neck cancer. *Cell Cycle* **12,** 1371–1384 (2013).

104. Lukacova, S., Sorensen, B. S., Alsner, J., Overgaard, J. & Horsman, M. R. The impact of hypoxia on the activity of lactate dehydrogenase in two different pre-clinical tumour models. *Acta Oncol.* **47,** 941–947 (2008).

105. Schroeder, M. A. *et al.* The cycling of acetyl-coenzyme A through acetylcarnitine buffers cardiac substrate supply: a hyperpolarized 13C magnetic resonance study. *Circ. Cardiovasc. Imaging* **5,** 201–209 (2012).

106. Ball, D. R. *et al.* Hyperpolarized butyrate: a metabolic probe of short chain fatty acid metabolism in the heart. *Magn. Reson. Med.* **71,** 1663–1669 (2014).

107. Dodd, M. S. *et al.* In vivo alterations in cardiac metabolism and function in the spontaneously hypertensive rat heart. *Cardiovasc. Res.* **95,** (2012).

108. Mansson, S., Petersson, J. S. & Scheffler, K. Fast metabolite mapping in the pig heart after injection of hyperpolarized. *Magn. Reson. Med.* **68,** 1894–1899 (2012).

109. Schroeder, M. A. *et al.* Hyperpolarized (13)C magnetic resonance reveals early- and late-onset changes to in vivo pyruvate metabolism in the failing heart. *Eur. J. Heart Fail.* **15,** 130–140 (2013).

110. Keshari, K. R. *et al.* Hyperpolarized 13C dehydroascorbate as an endogenous redox sensor for in vivo metabolic imaging. *Proc. Natl. Acad. Sci. U. S. A.* **108,** 18606–18611 (2011).

111. Gallagher, F. A., Kettunen, M. I. & Brindle, K. M. Imaging pH with hyperpolarized 13C. *NMR Biomed.* **24,** 1006–1015 (2011).

112. Von Morze, C. *et al.* Investigating tumor perfusion and metabolism using multiple hyperpolarized (13)C compounds: HP001, pyruvate and urea. *Magn. Reson. Imaging* **30,** 305–311 (2012).

113. Von Morze, C. *et al.* Simultaneous multiagent hyperpolarized C perfusion imaging. *Magn. Reson. Med.* (2013).

114. Hilty, C. & Bowen, S. Applications of dynamic nuclear polarization to the study of reactions and reagents in organic and biomolecular chemistry. *Org. Biomol. Chem.* **8,** 3361–3365 (2010).

115. Lerche, M. H. *et al.* Study of molecular interactions with 13C DNP-NMR. *J. Magn. Reson.* **203,** 52–56 (2010).

116. Mieville, P., Jannin, S., Helm, L. & Bodenhausen, G. Kinetics of yttrium-ligand complexation monitored using hyperpolarized (89)Y as a model for gadolinium in contrast agents. *J. Am. Chem. Soc.* **132,** 5006–5007 (2010).

117. Keshari, K. R., Kurhanewicz, J., Macdonald, J. M. & Wilson, D. M. Generating contrast in hyperpolarized 13C MRI using ligand-receptor interactions. *The Analyst* **137,** 3427–3429 (2012).

118. Jensen, P. R. *et al.* Detection of low-populated reaction intermediates with hyperpolarized NMR. *Chem. Commun.* 5168–5170 (2009).

119. Hanahan, D. & Weinberg, R. A. Hallmarks of Cancer: The Next Generation. *Cell* **144,** 646–674

120. Lim, K. S. *et al.* Inhibition of monocarboxylate transporter-4 depletes stem-like glioblastoma cells and inhibits HIF transcriptional response in a lactate-independent manner. *Oncogene* (2013).

121. Birsoy, K. *et al.* MCT1-mediated transport of a toxic molecule is an effective strategy for targeting glycolytic tumors. *Nat. Genet.* **45,** 104–108 (2013).

122. Mishkovsky, M. & Frydman, L. Progress in Hyperpolarized Ultrafast 2D NMR Spectroscopy. *Chem. Phys. Chem.* **9,** 2340–2348 (2008).

123. Day, S. E. *et al.* Detecting response of rat C6 glioma tumors to radiotherapy using hyperpolarized [1- 13C]pyruvate and 13C magnetic resonance spectroscopic imaging. *Magn. Reson. Med. Off. J. Soc. Magn. Reson. Med.* **65,** 557–563 (2011).

124. Park, J. M. *et al.* Metabolite kinetics in C6 rat glioma model using magnetic resonance spectroscopic imaging of hyperpolarized [1-(13)C]pyruvate. *Magn. Reson. Med.* **68,** 1886–1893 (2012).

125. Mullen, A. R. *et al.* Reductive carboxylation supports growth in tumour cells with defective mitochondria. *Nature* **481,** 385–388 (2012).

126. Mullen, A. R. *et al.* Oxidation of Alpha-Ketoglutarate Is Required for Reductive Carboxylation in Cancer Cells with Mitochondrial Defects. *Cell Rep.* (2014).

127. Menendez, J. A. & Lupu, R. Fatty acid synthase and the lipogenic phenotype in cancer pathogenesis. *Nat. Rev. Cancer* **7,** 763–777 (2007).

128. Son, J. *et al.* Glutamine supports pancreatic cancer growth through a KRAS-regulated metabolic pathway. *Nature* **496,** 101–105 (2013).

129. Reed, G. D. *et al.* High resolution (13)C MRI with hyperpolarized urea: in vivo T(2) mapping and (15)N labeling effects. *IEEE Trans. Med. Imaging* **33,** 362–371 (2014).

130.Lim KS, Lim Kj, Price AC, Orr BA, Eberhart CG, & Bar, EE. Inhibition of Monocarboxylate Transporter 4 (MCT4) targets stem-like cells in glioblastoma. *Oncogene (2013).*

131. Sciacovelli, M., Gaude, E., Hilvo, M. & Frezza, C. The metabolic alterations of cancer cells. *Methods Enzymol.* **542,** (2014).

132. Lin, G. *et al.* Reduced Warburg effect in cancer cells undergoing autophagy: steady-state 1H-MRS and real-time hyperpolarized 13C-MRS studies. *PloS One* **9,** (2014).

133. Vander Heiden, M. G., Cantley, L. C. & Thompson, C. B. Understanding the Warburg effect: the metabolic requirements of cell proliferation. *Science* **324,** 1029–1033 (2009).

134. Ferlay, J., Bray, F., Pisani, P. & Parkin, D. *Cancer incidence, mortality and prevalence worldwide*. **1,** (IARC Press, 2001).

135. Johnson, P. Hepatocellular carcinoma: is current therapy really altering outcome? *Gut.* **51,** 459–462 (2002).

136. Fong, Y., Sun, R. L., Jarnagin, W. & Blumgart, L. H. An analysis of 412 cases of hepatocellular carcinoma at a Western center. *Ann. Surg.* **229,** 790–799; discussion 799–800 (1999).

137. Balsells, J. *et al.* Resection of hepatocellular carcinoma in patients with cirrhosis. *Br. J. Surg.* **83,** 758–761 (1996).

138. A comparison of lipiodol chemoembolization and conservative treatment for unresectable hepatocellular carcinoma. Groupe d'Etude et de Traitement du Carcinome Hepatocellulaire. *N. Engl. J. Med.* **332,** 1256–1261 (1995).

139. Nowak, A. K., Chow, P. K. & Findlay, M. Systemic therapy for advanced hepatocellular carcinoma: a review. *Eur. J. Cancer* **40,** 1474–1484 (2004).

140. El-Nassan, H. B. Recent progress in the identification of BRAF inhibitors as anti-cancer agents. *Eur. J. Med. Chem.* **72,** (2014).

141. Hilger, R. A., Scheulen, M. E. & Strumberg, D. The Ras-Raf-MEK-ERK pathway in the treatment of cancer. *Onkologie* **25,** 511–518 (2002).

142. Downward, J. Targeting RAS signalling pathways in cancer therapy. *Nat. Rev. Cancer* **3,** (2003).

143. Avruch, J. *et al.* Ras activation of the Raf kinase: tyrosine kinase recruitment of the MAP kinase cascade. *Recent Prog. Horm. Res.* **56,** 127–155 (2001).

144. Bos, J. L. ras oncogenes in human cancer: a review. *Cancer Res.* **49,** 4682–4689 (1989).

145. Newell, P. *et al.* Ras pathway activation in hepatocellular carcinoma and anti-tumoral effect of combined sorafenib and rapamycin in vivo. *J. Hepatol.* **51,** 725–733 (2009).

146. Yang, D. *et al.* Therapeutic potential of a synthetic lethal interaction between the MYC proto-oncogene and inhibition of aurora-B kinase. *Proc. Natl. Acad. Sci. U. S. A.* **107,** 13836–13841 (2010).

147. Zhao, J. *et al.* Sorafenib or sunitinib as postoperative adjuvant therapy for Chinese patients with locally advanced clear cell renal cell carcinoma at high risk for disease recurrence. *Urol. Oncol.* **31,** 1800–1805 (2013).

148. Zimmermann, K. *et al.* Sunitinib treatment for patients with advanced clear-cell renal-cell carcinoma after progression on sorafenib. *Oncology* **76,** 350–354 (2009).

149. Gish, R. G., Finn, R. S. & Marrero, J. A. Extending survival with the use of targeted therapy in the treatment of hepatocellular carcinoma. *Gastroenterol. Hepatol.* **9,** (2013).

150. Horiuchi, D. *et al.* MYC pathway activation in triple-negative breast cancer is synthetic lethal with CDK inhibition. *J. Exp. Med.* **209,** 679–696 (2012).

151. Malumbres, M. & Barbacid, M. Cell cycle, CDKs and cancer: a changing paradigm. *Nat. Rev. Cancer* **9,** 153–166 (2009).

152. Malumbres, M., Pevarello, P., Barbacid, M. & Bischoff, J. R. CDK inhibitors in cancer therapy: what is next? *Trends Pharmacol. Sci.* **29,** (2008).

153. Lustig, M., Donoho, D. & Pauly, J. M. Sparse MRI: The application of compressed sensing for rapid MR imaging. *Magn. Reson. Med.* **58,** 1182–1195 (2007).

154.Hu, S. *et al.* Compressed sensing for resolution enhancement of hyperpolarized 13C flyback. *J. Magn. Reson.* **192,** 258–264 (2008).

155. Hu, S. *et al.* 3D compressed sensing for highly accelerated hyperpolarized (13)C MRSI with in vivo applications to transgenic mouse models of cancer. *Magn. Reson. Med. Off. J. Soc. Magn. Reson. Med..* **63,** 312–321 (2010).

156. Hurd, R. E. *et al.* Exchange-linked dissolution agents in dissolution-DNP (13)C metabolic imaging. *Magn. Reson. Med.* **70,** 936–942 (2013).

157. Asghar Butt, S. *et al.* Monitoring mammary tumor progression and effect of tamoxifen treatment in. *Magn. Reson. Med. Med.* (2014).

158. Bohndiek, S. E., Kettunen, M. I., Hu, D. & Brindle, K. M. Hyperpolarized (13)C spectroscopy detects early changes in tumor vasculature and metabolism after VEGF neutralization. *Cancer Res.* **72,** 854–864 (2012).

159. Brindle, K. M., Bohndiek, S. E., Gallagher, F. A. & Kettunen, M. I. Tumor imaging using hyperpolarized 13C magnetic resonance spectroscopy. *Magn. Reson. Med.* **66,** 505–519 (2011).

160. Chen, A. P. *et al.* Hyperpolarized C-13 spectroscopic imaging of the TRAMP mouse at 3T-initial experience. *Magn. Reson. Med.* **58,** 1099–1106 (2007).

161. Chen, A. P. *et al.* Simultaneous investigation of cardiac pyruvate dehydrogenase flux, Krebs cycle metabolism and pH, using hyperpolarized [1,2-(13)C2]pyruvate in vivo. *NMR Biomed.* **25,** 305–311 (2012).

162. Darpolor, M. M., Kaplan, D. E., Pedersen, P. L. & Glickson, J. D. Human Hepatocellular Carcinoma Metabolism: Imaging by Hyperpolarized C Magnetic Resonance Spectroscopy. *J. Liver Dis. Transplant.* **1,** (2012).

163. Darpolor, M. M. *et al.* In vivo MRSI of hyperpolarized [1-(13)C]pyruvate metabolism in rat hepatocellular carcinoma. *NMR Biomed.* **24,** 506–513 (2011).

164. Dutta, P. *et al.* Evaluation of LDH-A and glutaminase inhibition in vivo by hyperpolarized. *Cancer Res.* **73,** 4190–4195 (2013).

165. Gallagher, F. A. *et al.* Detection of tumor glutamate metabolism in vivo using (13)C magnetic resonance spectroscopy and hyperpolarized [1-(13)C]glutamate. *Magn. Reson. Med. Off. J. Soc. Magn. Reson. Med. Soc.* **66,** (2011).

166. Hill, D. K. *et al.* Model free approach to kinetic analysis of real-time hyperpolarized 13C magnetic resonance spectroscopy data. *PloS One* **8,** (2013).

167. Nelson, S. J. *et al.* Metabolic imaging of patients with prostate cancer using hyperpolarized [1-(1)(3)C]pyruvate. *Sci. Transl. Med.* **5,** (2013).

168. Bahrami, N., Swisher, C. L., Von Morze, C., Vigneron, D. B. & Larson, P. E. Z. Kinetic and perfusion modeling of hyperpolarized (13)C pyruvate and urea in cancer with arbitrary RF flip angles. *Quant. Imaging Med. Surg.* **4,** (2014).

169. Park, I. *et al.* Dynamic hyperpolarized carbon-13 MR metabolic imaging of nonhuman primate brain. *Magn. Reson. Med.* **71,** (2014).

170. Cuenod, C. A. & Balvay, D. Perfusion and vascular permeability: basic concepts and measurement in DCE-CT and. *Diagn. Interv. Imaging* **94,** 1187–1204 (2013).

171. Tofts, P. S. Modeling tracer kinetics in dynamic Gd-DTPA MR imaging. *J. Magn. Reson. Imaging* **7,** (1997).

11. Appendix

11.1 Symbolic solver for kinetic models

```
function [solution sim_sol] = findsymbolicsolution()
% [solution sim_sol] = function findsymbolicsolution()
%
%
% Simplifies DX(t)=AX to x(t)=phi(t,t=0)*x(t=0)
% where phi(t)=exp(A*t)=inverselaplace((sI-A)^-1)
%
% Written by Christine Leon Swisher

% define symbolic syms
syms pL pP pU Kpl Ktrans K2 R1all
syms s Lac0 Pyr0 Urea0

% initial condition
Mo=[Pyr0,Lac0,Urea0];

% metabolites
mets = {'pyr','lac','urea'};

% parameter matrix
K = [ -R1all-Kpl,    0,    0;...
          Kpl,  -R1all,    0;...
            0,    0, -pU];
% solve
I=eye(3,3);
sI=s*I;
inv(sI-K);
solution=ilaplace(inv(sI-transpose(K)))

% further simplify solution
%sim_sol=Mo*simplify(solution)
sim_sol=Mo*simplify(solution)

end
```

This gives the following simplified solution:

```
Pyr(t)  = Pyr(0)*exp(-t*(Kpl+R1p))

Lac(t)   = Lac(0)*exp(-t*Rl)-(Kpl*Pyr(0)*(exp(-t*(Kpl+R1p))-exp(-t*R1l)))/Kpl-
R1l+R1p)

Urea(t) = Urea(0)*exp(-t*R1u)
```

11.2 Automated Kinetic Modeling Tool

Models shown in Chapter 8 were implemented in C++ with an open-source Spectroscopic Imaging Visualization and Computing (SIVIC) package. The source code, as well as a

command line tool (svk_mrs_kinetics) and GUI application are freely available for download. The SIVIC C++ class (svkMRSKinetics) can easily be extended to support other kinetic models.

Available at: **http://sourceforge.net/apps/trac/sivic/**

Demo available: **http://www.ismrm.org/14/program_files** (Abstract #3793)

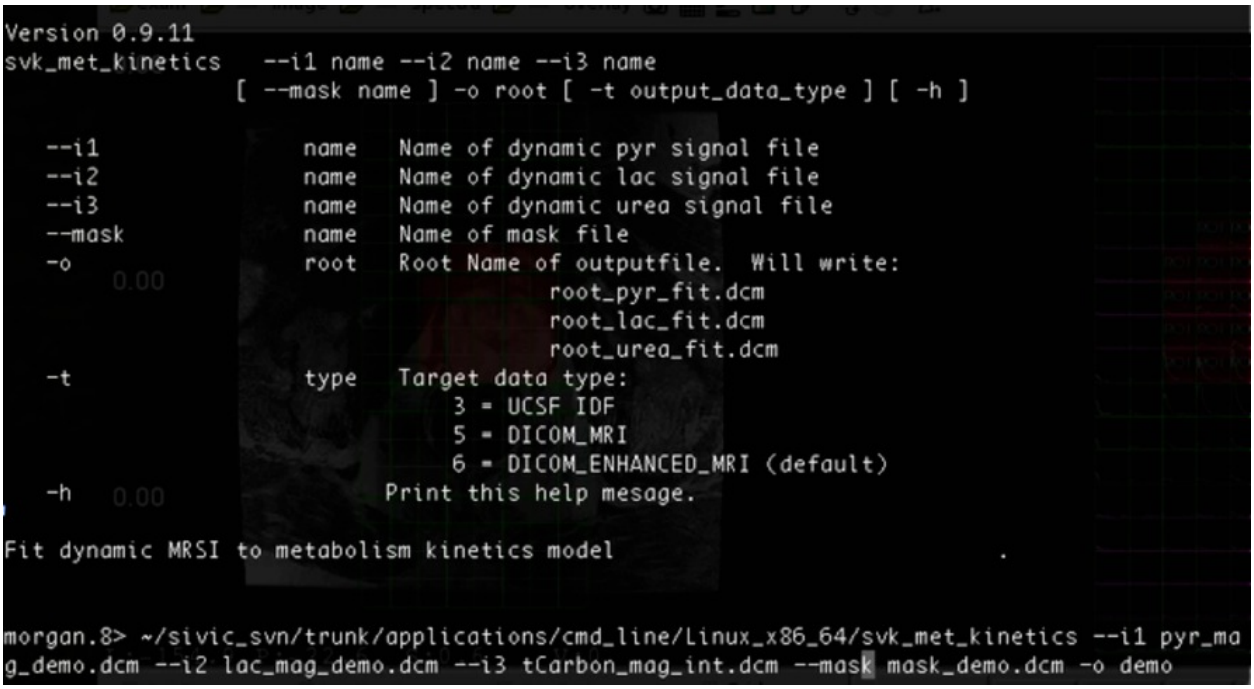

Figure 11.1: Screenshot of command-line tool.

It is the policy of the University to encourage the distribution of all theses, dissertations, and manuscripts. Copies of all UCSF theses, dissertations, and manuscripts will be routed to the library via the Graduate Division. The library will make all theses, dissertations, and manuscripts accessible to the public and will preserve these to the best of their abilities, in perpetuity.

I hereby grant permission to the Graduate Division of the University of California, San Francisco to release copies of my thesis, dissertation, or manuscript to the Campus Library to provide access and preservation, in whole or in part, in perpetuity.

Author Signature  Date June 13, 2014